

January 2008

An Orthogonally-Fed, Active Linear Phased Array of Tapered Slot Antennas

Andrew R. Mandeville

University of Massachusetts Amherst

Follow this and additional works at: <https://scholarworks.umass.edu/theses>

Mandeville, Andrew R., "An Orthogonally-Fed, Active Linear Phased Array of Tapered Slot Antennas" (2008). *Masters Theses 1911 - February 2014*. 114.

Retrieved from <https://scholarworks.umass.edu/theses/114>

This thesis is brought to you for free and open access by ScholarWorks@UMass Amherst. It has been accepted for inclusion in Masters Theses 1911 - February 2014 by an authorized administrator of ScholarWorks@UMass Amherst. For more information, please contact scholarworks@library.umass.edu.

**AN ORTHOGONALLY-FED, ACTIVE LINEAR PHASED ARRAY OF
TAPERED SLOT ANTENNAS**

A Thesis Presented

by

ANDREW R. MANDEVILLE

Submitted to the Graduate School of the
University of Massachusetts Amherst in partial fulfillment
of the requirements for the degree of

MASTER OF SCIENCE

May 2008

Electrical and Computer Engineering

© Copyright by Andrew R. Mandeville 2008

All Rights Reserved

**AN ORTHOGONALLY-FED, ACTIVE LINEAR PHASED ARRAY OF
TAPERED SLOT ANTENNAS**

A Thesis Presented

by

ANDREW R. MANDEVILLE

Approved as to style and content by:

Robert W. Jackson, Chair

Daniel H. Schaubert, Member

Marinos Vouvakis, Member

C.V. Hollot, Department Head
Electrical and Computer Engineering

To my mom and dad.

ACKNOWLEDGEMENTS

I would like to thank my advisors Professor Jackson and Professor Schaubert for providing me with the opportunity to study under their guidance. Their insights, mentorship, and patience have been very much appreciated. Also, I would like to thank Professor Vouvakis for serving as a member on my committee, as well as for providing helpful suggestions and discussions.

John Nicholson of UMass, and Mike Gouin and Bill LaPlante of Sensata Technologies provided a great deal of assistance with the assembly, soldering, and wirebonding of the antenna packages in this project. Their help was invaluable in my completion of this thesis.

Finally, I would like to acknowledge my fellow graduate students in CASCA for their moral and practical support, including Justin Creticos, Steve Holland, Sreenivas Kasturi, Eric Marklein, Georgios Paraschos, and Mauricio Sanchez.

ABSTRACT

AN ORTHOGONALLY-FED, ACTIVE LINEAR PHASED ARRAY OF TAPERED SLOT ANTENNAS

MAY 2008

ANDREW R. MANDEVILLE, B.S.E.E., VIRGINIA POLYTECHNIC INSTITUTE
AND STATE UNIVERSITY

M.S.E.C.E., UNIVERSITY OF MASSACHUSETTS AMHERST

Directed by: Professor Robert W. Jackson

An active, broadband antenna module amenable for use in low cost phased arrays is proposed. The module consists of a Vivaldi antenna integrated with a frequency conversion integrated circuit. A method of orthogonally mounting endfire antennas onto an array motherboard is developed using castellated vias. A castellated active isolated Vivaldi antenna package is designed, fabricated, and measured. An 8x1 phased array of castellated, active Vivaldi antenna packages is designed and assembled. Each element has approximately one octave of bandwidth centered in X-band, and each is mounted onto a coplanar waveguide motherboard. Radiation patterns of the array are measured at several frequencies and scan angles.

TABLE OF CONTENTS

ACKNOWLEDGEMENTS.....	v
ABSTRACT.....	vi
LIST OF TABLES.....	ix
LIST OF FIGURES.....	x
CHAPTER	
1. INTRODUCTION.....	1
1.1 Active Antennas.....	1
1.2 Background and Motivation.....	3
1.3 Thesis Objectives.....	7
2. PROJECT OVERVIEW.....	9
2.1 Orthogonally-fed Vivaldi Antennas.....	9
2.2 Active Packages.....	14
3. INDIVIDUAL VIVALDI ANTENNA.....	20
3.1 Vivaldi Design.....	20
3.2 Fabrication and Assembly.....	23
3.3 Measurements.....	26
3.3.1 Passive Vivaldi Measurements.....	26
3.3.2 Active Vivaldi Measurements.....	31
3.3.3 Comparison of Active and Passive Elements.....	35
3.4 Summary.....	41
4. ACTIVE VIVALDI ARRAY.....	43
4.1 Array Design.....	43
4.1.1 Background.....	43
4.1.2 Design of 8x1 Linear Array.....	44
4.1.3 Effects of Modularity.....	55

4.2	Array System Components and Assembly.....	57
4.2.1	Active Element Layout.....	57
4.2.2	Array Feeding and Phase Control Network.....	58
4.2.3	Array Assembly.....	63
4.3	Array Measurements.....	65
4.4	Summary.....	74
5.	CONCLUSION AND FUTURE WORK.....	75
APPENDICES		
A.	ISOLATED VIVALDI ANTENNA WITH CORRUGATED EDGES.....	78
B.	DIMENSIONED DRAWINGS.....	83
C	COMPONENT DATASHEETS.....	88
	BIBLIOGRAPHY.....	95

LIST OF TABLES

Table	Page
3.1: Comparison of Passive and Active Vivaldi Elements.....	36
4.1: Excitation Errors in 8x1 Array.....	68
A.1: E-Plane Radiation Characteristics of Isolated Vivaldi Antenna with and without Corrugations.....	82
A.2: H-Plane Radiation Characteristics of Isolated Vivaldi Antenna with and without Corrugations.....	82

LIST OF FIGURES

Figure	Page
1.1: Examples of Vivaldi Arrays, for references see [4] and [5]	4
1.2: Planar Vivaldi Array with Modular, Surface Mountable Elements.....	6
2.1: CPW-Microstrip Castellated Interconnection.....	10
2.2: Simulated Return Loss of CPW-Microstrip Transition	12
2.3: Measured Return Loss of CPW-Microstrip Transition.....	13
2.4: Simulated Return Loss of CPW-Microstrip Transition	14
2.5: Simulation Geometry for Microstrip-fed Slotline	15
2.6: Simulated Return Loss of Microstrip-fed Slotline.....	16
2.7: Feed Layout of Active Slotline Prototype	17
2.8: (a) Front View; (b) Back View; (c) Close-up of Integrated Feed of Active Slotline Prototype.....	18
2.9: Measured Conversion Gain of Active Slotline Prototype	19
3.1: Important Parameters for the (a) tapered slot, (b) microstrip feed of Vivaldi Antenna.....	21
3.2: Simulated Return Loss of Isolated Vivaldi Element	23
3.3: Fabricated Vivaldi Element and Motherboard.....	24
3.4: Vivaldi Antenna Mounted on CPW Motherboard.....	25
3.5: Close-up of Castellated Interconnection for Active Vivaldi Antenna Package.....	25
3.6: Measured Return Loss of Passive Vivaldi Antenna	26
3.7: Measured vs. Simulated E-Plane Co-polarized Radiation Patterns of Passive Isolated Vivaldi Element at: (a) 6 GHz; (b) 7 GHz; (c) 8 GHz; (d) 9 GHz; (e) 10 GHz; (f) 11 GHz.....	28

3.8: Measured vs. Simulated H-Plane Co-polarized Radiation Patterns of Passive Isolated Vivaldi Element at: (a) 6 GHz; (b) 7 GHz; (c) 8 GHz; (d) 9 GHz; (e) 10 GHz; (f) 11 GHz.....	29
3.9: Schematic of Setup Used to Measure Active Antenna.....	31
3.10: Measured vs. Simulated E-Plane Co-polarized Radiation Patterns of Active Isolated Vivaldi Element at: (a) 6 GHz; (b) 7 GHz; (c) 8 GHz; (d) 9 GHz; (e) 10 GHz; (f) 11 GHz.....	32
3.11: Measured vs. Simulated H-Plane Co-polarized Radiation Patterns of Active Isolated Vivaldi Element at: (a) 6 GHz; (b) 7 GHz; (c) 8 GHz; (d) 9 GHz; (e) 10 GHz; (f) 11 GHz.....	33
3.12: E-Plane Cross-polarized Radiation Patterns of Passive and Active Isolated Vivaldi Elements at: (a) 6 GHz; (b) 7 GHz; (c) 8 GHz; (d) 9 GHz; (e) 10 GHz; (f) 11 GHz.....	38
3.13: H-Plane Cross-polarized Radiation Patterns of Passive and Active Isolated Vivaldi Elements at: (a) 6 GHz; (b) 7 GHz; (c) 8 GHz; (d) 9 GHz; (e) 10 GHz; (f) 11 GHz.....	39
4.1: Measured Active Reflection Coefficient for Central Element in 16x1 Array of Vivaldi Antennas (see [4] for Array Dimensions).....	45
4.2: Simulated Active Reflection Coefficient for Infinite-by-1 Array of Vivaldi Antennas	47
4.3: Simulated VSWR of Infinite-by-1 Array of Vivaldi Elements for Several Scan Angles	48
4.4: Simulated Active Reflection Coefficients of Elements in an 8x1 Array of Vivaldi Elements for scan angles of (a) 0°; (b) 20°; (c) 30°; (d) 40°	50
4.5: Simulated Active Reflection Coefficients of Elements in an 8x1 Array (Edge Elements Terminated) of Vivaldi Elements for scan angles of (a) 0°; (b) 20°; (c) 30°; (d) 40°	53
4.6: Simulated VSWR for Central Element in 8x1 Array of Vivaldi Antennas with and without Electrical Separation Between Elements.....	56
4.7: Active Vivaldi Element Packages.....	57
4.8: IF Control Board.....	61
4.9: Non-inverting Voltage Amplifier	62
4.10: DC Control Network.....	63

4.11: Assembled Vivaldi Array (a) Front View; (b) Back View	64
4.12: Near-field Measurement Setup	66
4.13: Measured Broadside Radiation Pattern for Vivaldi Array with Excitation Errors.....	67
4.14: Measured Phase at Array Aperture for Scan Angles of (a) 0° , (b) 20°	69
4.15: Measured vs. Simulated E-Plane Radiation Patterns for 8x1 Array of Vivaldi Elements (0° scan) at: (a) 6 GHz, (b) 8 GHz, (c) 10 GHz.....	70
4.16: Measured vs. Simulated E-Plane Radiation Patterns for 8x1 Array of Vivaldi Elements (20° scan) at: (a) 8 GHz, (c) 10 GHz	72
4.17: Measured vs. Simulated E-Plane Radiation Patterns for 8x1 Array of Vivaldi Elements (40° scan) at: (a) 8 GHz, (c) 10 GHz	73
A.1: Vivaldi Antenna with Corrugated Edges.....	78
A.2: E-Plane Gain Patterns for Isolated Vivaldi Antenna with Corrugations at (a) 6GHz, (b) 7 GHz, (c) 8 GHz, (d) 9 GHz, (e) 10 GHz, (f) 11 GHz.....	79
A.3: H-Plane Gain Patterns for Isolated Vivaldi Antenna with Corrugations at (a) 6GHz, (b) 7 GHz, (c) 8 GHz, (d) 9 GHz, (e) 10 GHz, (f) 11 GHz.....	80
B.1: Isolated Active Vivaldi Element.....	83
B.2: Active Vivaldi Array Element Element	85
B.3: Full 8x1 Vivaldi Array	87
C.1: Datasheet for HMC130 Mixer IC	88
C.2: Datasheet for JSPHS-1000 Phase Shifter.....	94

CHAPTER 1

INTRODUCTION

1.1 Active Antennas

Active antennas, active integrated antennas, and active arrays are the focus of much interest in current research. Traditionally, antennas have been viewed as individual components in a microwave system, connected to the transmitter/receiver circuitry by transmission line. However, in many applications it is advantageous to integrate antennas and microwave circuitry into a single package. In an active antenna, one or more active electronic devices are incorporated within the radiating structure of an antenna. By integrating electronics and the antenna into a single package, one can achieve improvements in the performance, size, and cost of a system, all of which are critical factors in the design of phased arrays. Active antennas and active arrays are described in detail in [1]-[3].

The incorporation of upconversion/downconversion electronics at the antenna can help improve system performance. Conductor and dielectric losses in a transmission line increase as a function of frequency. Dissipative losses caused by lossy transmission lines increase the insertion loss and noise figure of a system. Additionally, unshielded transmission line structures such as microstrip or coplanar waveguide become increasingly efficient radiators as frequency is increased, and spurious radiation from an antenna's feed structure may increase the sidelobe and cross-polarization levels of the antenna's far-field pattern. In a phased array where many elements must be excited, large feed networks are required, and losses in such structures may severely degrade the system performance. By upconverting/downconverting in

frequency at the antenna, it is possible to substantially limit the amount of distance over which high frequency signals must propagate, which will keep dissipative losses and unwanted radiation to a minimum.

The integration of the full RF front end circuitry can yield additional performance improvements. In order to minimize noise figure, it is desirable to make a low noise amplifier the first stage following the antenna in a microwave receiver. Placing the receiver at the antenna ensures that the length of transmission line between the antenna and LNA is minimized. Likewise, integrating the transmitter circuitry allows moderate power amplifiers to be used at each element in an array, rather than a single high power amplifier at the input of the feed network. By spreading the power amplification over the aperture, much lower power levels are dissipated in the feed network. This allows for the use of components with lower power handling capabilities, and improves efficiency. Additionally, thermal dissipation is spread across a much larger area. Finally, spreading the RF circuitry across the array aperture allows for the graceful degradation of the array. As such, in an active array, the failure of a single element, or even multiple elements, would not catastrophically impact the array's performance.

Reductions in the size and cost of a system can also be achieved by using active antennas. In a microwave system, the size of the antenna is often a limiting factor in how small the system may be. In an active antenna, the radiating area is utilized as a surface on which to mount electronics. The antenna serves as a package for the electronic devices and in some configurations may also serve additional mechanical

functions such as a heat sink. In other configurations the antenna may serve as a filter or resonator for the active circuitry.

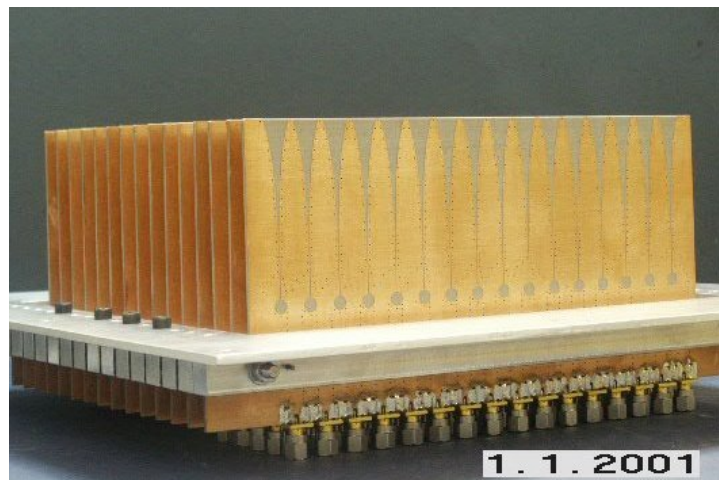
Active elements are well suited for mass-production in low-cost automated processes, as electronic packages can be mounted onto an active antenna using pick and place technology. In active integrated antennas where the radiator and the active devices share a common substrate, an entire active package can be fabricated in a single process. Because frequency conversion takes place at the antenna, only low frequency signals need to be transferred off an active antenna module. This allows for simpler interconnects and lower cost feed networks to be used.

1.2 Background and Motivation

Planar antennas fabricated using printed circuit board (PCB) techniques are well-suited for use as integrated antennas. Patch antennas are popular for use as radiating elements in active configurations due to their small size, low profile, and the ease of integration with their feed lines. A major drawback to patch antennas is that they suffer from narrow bandwidths. Tapered slot antennas (TSA) are a class of planar antennas, which are more suitable for wideband applications. Phased arrays that use TSA elements are known to operate over multiple octaves of bandwidth, and are capable of widescan performance. Vivaldi antennas are a type of TSA with exponentially flared slots. The electrical performance of Vivaldi antennas and Vivaldi arrays will be discussed in more detail in Chapters 3 and 4.

From a performance standpoint, Vivaldi arrays are often attractive; however, the assembly of such arrays can be problematic. One problem is that Vivaldi elements are

generally electrically large, and as such, it may be difficult to use Vivaldi arrays in space-limited or low-profile applications. A second problem is that Vivaldi elements radiate in the endfire direction. The main beam of an endfire antenna is located in the same plane as the antenna's feed. In order for a Vivaldi array to radiate at broadside, the individual elements must be oriented orthogonally to the face of the array aperture. Figure 1.1 shows examples of a typical Vivaldi arrays.



(a)



(b)

Figure 1.1: Examples of Vivaldi Arrays, for references see [4] and [5]

Figure 1.1a shows an array assembled by Kasturi [4]; the elements within the array are held in place with metallic slats, which double as a ground plane. Figure 1.1b is an example of a dual-polarized Vivaldi array in an “egg crate” configuration [5]. Cards of Vivaldi elements in an egg-crate type configuration are fit together using slots, or individual elements may be soldered together. Several observations can be made from the arrays in Figure 1.1. First, the Vivaldi antennas are printed on cards containing multiple, electrically-connected elements. Currently, Vivaldi arrays are designed and built with the elements electrically-connected, for reasons which will be discussed in Chapter 4. Secondly, each element in the array is fed in the plane of the board with an end launch connector. Finally, it is apparent that the designs are constructed from techniques which cannot easily be implemented in automated processes. The mechanical characteristics of the arrays above, as well as TSA arrays in general, preclude the use of TSA elements in low cost applications. However, because of their superior performance it would be highly desirable to be able to produce TSA elements that are amenable for use in low cost phased arrays. For the reasons stated in the previous section, a low cost array would use active antenna packages as elements. Such elements would need to be modular, fabricated using standard, low cost techniques, and capable of being incorporated onto an array motherboard in an automated process. An illustration of a phased array containing such elements is shown in Figure 1.2.

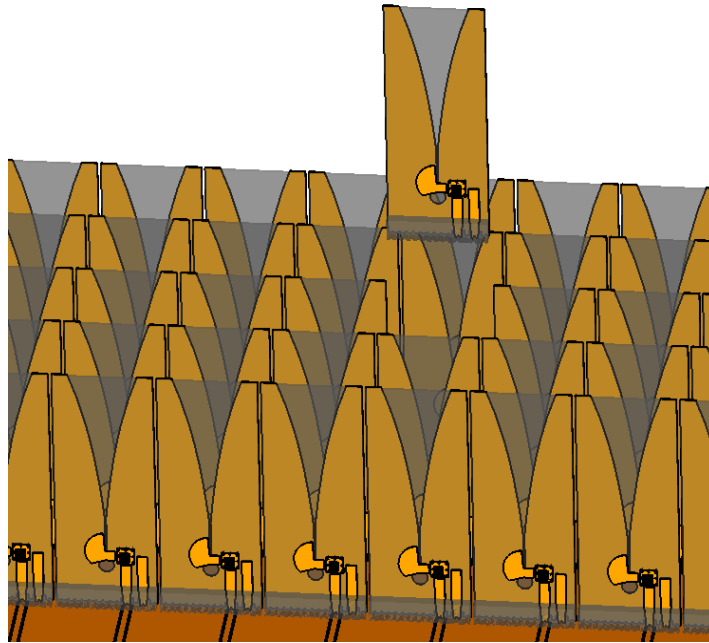


Figure 1.2: Planar Vivaldi Array with Modular, Surface Mountable Elements

Modular antenna packages like the ones shown in Figure 1.2 would not only ease the fabrication and assembly of an array, but would also allow for the quick removal of failed elements. The active packages in the illustration are surface mounted onto a coplanar waveguide (CPW) motherboard, which contains the array's feed network and control lines. An array of surface-mountable elements could easily be assembled in an automated process. In order to minimize cost, the elements should be fabricated using low-cost PCB techniques, and other standard, automated techniques such as solder reflow and wirebonding.

1.3 Thesis Objectives

Generally stated, the objective of this thesis was to develop active Vivaldi antenna modules for use in low-cost phased arrays. The modules were to be designed such that they could be orthogonally mounted onto a coplanar waveguide motherboard, and fabricated using simple PCB processes. Specifically, the following deliverables were proposed:

Design a surface-mountable active Tapered Slot Antenna package for use in low cost phased arrays.

- Design packages that could be orthogonally-fed from a CPW motherboard, and could be manufactured using standard low cost PCB fabrication processes.
- Integrate a mixer into the microstrip feed of a Vivaldi antenna, and prototype the layout by designing and measuring an active slotline package.

Design, fabricate, and measure passive and active isolated Vivaldi antenna packages.

- Design an isolated Vivaldi antenna with roughly one octave of bandwidth, centered in X-band, on a 20 mil thick Rogers 5880 substrate.
- Design a castellated Vivaldi antenna package, and integrate it with an off-the-shelf frequency conversion IC. The packages were to be orthogonally mounted onto a CPW motherboard.

- Measure the return loss and radiation patterns of the Vivaldi elements, and compare the results with simulation data. Additionally, the efficiencies and radiation patterns of the passive and active configurations were to be compared.

Design, fabricate, and measure a linear phased array of active Vivaldi elements.

- Design an 8x1 element array of Vivaldi elements, with at least one octave of bandwidth at broadside, and capable of a 40° E-plane scan.
- Design modular, castellated Vivaldi antenna packages for use within the 8x1 element array. The packages were to be integrated with a mixer IC, and orthogonally mounted onto a CPW motherboard.
- Assemble the 8x1 element array, and design and build a phase control network to implement the beam scanning.
- Measure the array patterns for several frequencies and scan angles, and compare the results with simulation data.

CHAPTER 2

PROJECT OVERVIEW

2.1 Orthogonally-fed Vivaldi Antennas

As was stated in the introduction, it is desirable to design low-cost, active Vivaldi element packages, which may be incorporated onto a phased array motherboard using a surface-mount-like technique. Currently, the elements for many TSA arrays are designed with feed networks that are located on the same PCB as the antennas themselves. Such designs are not applicable for surface-mounting. In order to achieve a surface mountable Vivaldi antenna package, the antennas must be orthogonally fed. In [6], TSA were orthogonally fed using an aperture coupling configuration. Aperture coupling would not be usable at IF, and thus was not an acceptable solution for this project. Additionally, the paper made no reference to the method with which the TSA were mounted onto the ground plane.

For this project an orthogonal mounting scheme was developed that was simple, mechanically sound, and operated well for frequencies from DC through X-band. The solution was to employ castellated vias at the edge of the antenna packages. Castellated vias (or castellations) are essentially semicircular vias, and have been used to provide electrical connections for ceramic integrated circuit packages [7]. When implemented on PCB structures, castellated vias can be manufactured by fabricating standard plated-through vias, then simply cutting the vias in half. Therefore, a castellated board can be produced using the same low-cost processes used to manufacture other PCB structures. Figure 2.1 illustrates the general concept of using castellations for surface mount applications.

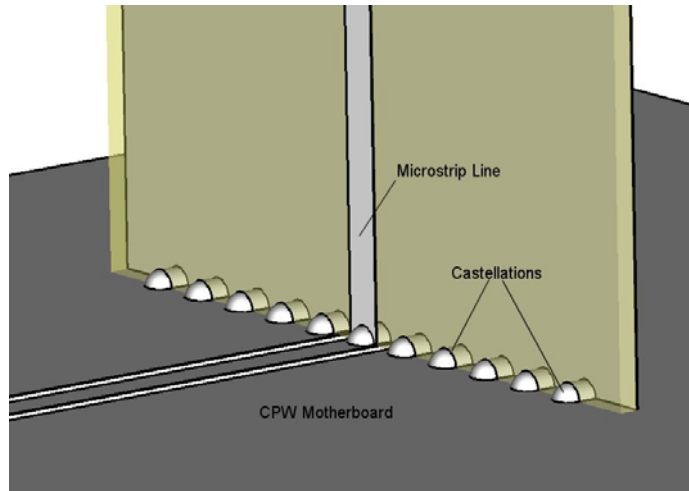


Figure 2.1: CPW-Microstrip Castellated Interconnection

In the scheme shown in Figure 2.1, a microstrip PCB is orthogonally mounted on a coplanar waveguide motherboard. In order to mount the microstrip board, solder is reflowed through the castellations. The castellations provide an electrical connection between the CPW signal line and the microstrip line, an electrical connection between the CPW and microstrip ground planes, and a mechanical connection between the two boards. The CPW signal ground doubles as a ground plane for an antenna mounted onto the motherboard.

In order to evaluate the electrical and mechanical performance the castellated interconnection, a simple prototype of the structure shown in Figure 2.1 was designed, built, and measured. The prototype consisted of a castellated microstrip PCB mounted on a small CPW motherboard. Both transmission lines were designed on 31 mil thick FR-4 substrates. Additionally, a 62 mil thick FR-4 support package was attached as shown in Figure 2.1. Because the Vivaldi antennas for this thesis were specified to operate through X-band, the castellated interconnection needed to perform well up to 12 GHz. The prototype structure was analyzed using CST Microwave Studio, a full wave,

3D, computational electromagnetics software package, which utilizes the Finite Integration-Time Domain method. Time domain methods are well suited for analyzing wideband problems, thus CST was used to simulate many of the broadband structures encountered in this thesis.

The simulations of the prototype were designed to analyze what effect the castellations, the perpendicular junction between the CPW and microstrip lines, and the support package had on overall electrical performance of the structure. Because the castellations extend all the way through the mounted element, a stub equal to the width of the element's substrate is added to the coplanar feed line.

At 12 GHz, a 31 mil long stub of CPW is roughly .05 wavelengths long, and can be considered electrically short. The prototype was simulated with and without castellated vias; and, it was concluded that at 12 GHz the extra length had very little effect. However, if castellations are to be used at higher frequencies, or with thicker substrates, such a stub may be electrically large, and would have to be accounted for. A more significant effect in the performance of the prototype was caused by the junction between the CPW and the microstrip. In general, a change in height of a transmission line tends to introduce capacitance, thereby lowering the line impedance. Furthermore, the addition of a dielectric covering to a transmission line also lowers the line impedance. As a result, the CPW-to-microstrip transition at the castellated interconnection may be viewed as a section of transmission line with lower impedance. In order to compensate for capacitance at the junction, a linear taper of both the CPW and microstrip lines was applied at the transition. Figure 2.2 shows simulation results comparing CPW-to-microstrip transitions with and without compensation.

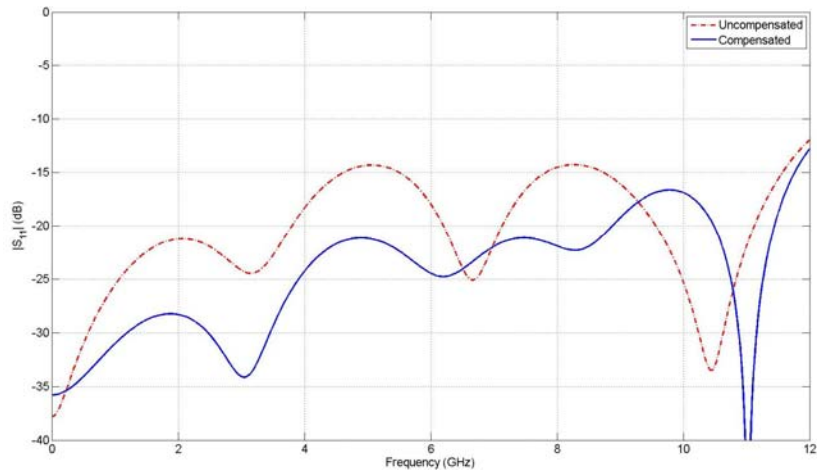


Figure 2.2: Simulated Return Loss of CPW-Microstrip Transition

The results indicate that the compensation at the castellated interconnection does indeed improve the return loss at the junction. An inexpensive prototype of the design was fabricated and measured. A small, 50 ohm microstrip trace on a 31-mil-thick PCB was orthogonally mounted onto a 50 ohm grounded CPW motherboard using castellated vias. The microstrip trace was 1.54 mm in width, and the CPW trace was 1.27 in width with a gap of 0.51 mm. The castellated vias were 0.5 mm in diameter and spaced 1 mm apart. The ends of both the microstrip and CPW lines were terminated in end-launch coaxial connectors to facilitate measurements. Figure 2.3 shows a comparison between the measured and simulated return loss of the prototype. Time windowing was performed on the measured results to remove reflections from the coaxial connectors.

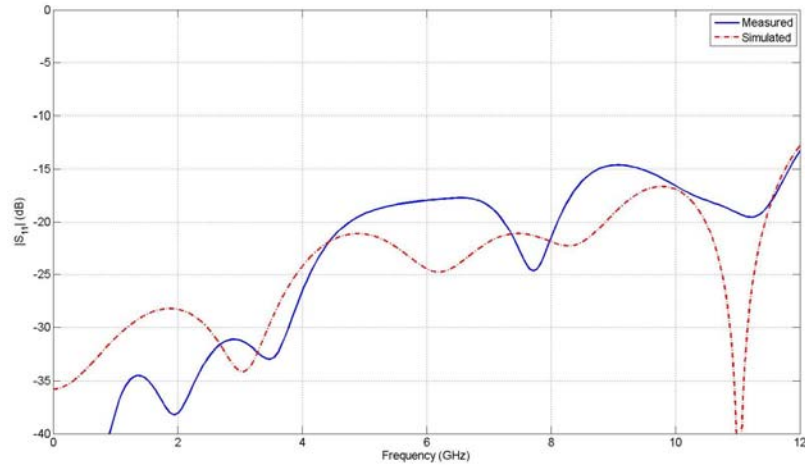


Figure 2.3: Measured Return Loss of CPW-Microstrip Transition

There is relatively good agreement between the measured and simulated results. The measured results demonstrate that the castellated interconnection has better than 15 dB return loss over the desired band of operation. The Vivaldi antennas in this thesis were manufactured on a 20-mil-thick Rogers 5880 substrate ($\epsilon_r = 2.2$, $\tan\delta = .001$), with a 62-mil-thick support package, and were mounted on an FR-4 CPW motherboard. The castellated interconnection for this configuration was designed and simulated. A plot of the simulated return loss for the design is shown in Figure 2.4.

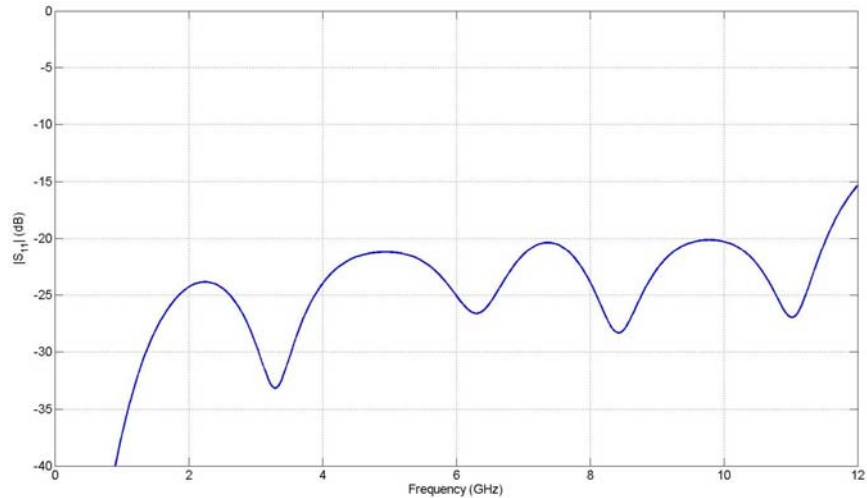


Figure 2.4: Simulated Return Loss of CPW-Microstrip Transition

2.2 Active Packages

The Vivaldi antennas designed for this thesis were used as elements in active antenna packages. The motivation for using an active antenna scheme was described in Chapter 1. In general, Vivaldi antennas (as well as other TSA) consist of two transmission line structures: the radiating tapered slotline, and a feed line, which is typically stripline or microstrip. In [8] and [9], two and three terminal semiconductor devices were integrated with TSA slotline structures. However, the impedance of a slotline transmission line tends to be fairly high, and is not suitable for integration with ICs designed for the typical 50 ohm reference impedance. Alternatively, electronic devices may be integrated with the antenna feed line, which would present a 50 ohm impedance. In [10], active components were integrated within the microstrip feed network of a linear array of TSA elements, which was printed on a single card. In this thesis, an active device was integrated with the microstrip feed of the Vivaldi antenna. For the best performance, the device was integrated such that the amount of

transmission line between it and the radiating structure was minimized. In practice, an active package would contain a full RF front-end. For simplification, only a mixer IC was integrated with the active packages in this project. An off the shelf mixer chip, the Hittite HMC130 IC, was chosen as the active component. The HMC130 is a double balanced diode mixer which has a bandwidth from 6 to 11 GHz, requires an LO drive power between 9 and 15 dBm, and has a conversion loss of 7 dB. Additionally, it is packaged on a 1.48 mm square, surface mountable die. A datasheet for the HMC130 is included in Appendix C.

In order to evaluate the performance of the mixer when integrated within the microstrip feed, an active slotline prototype was designed and built. The prototype consisted of a slotline fed by a microstrip line, which was integrated with the mixer IC. The slotline was terminated with a second microstrip feed line. In order to transfer a signal from the microstrip to the slotline, which is on the other side of the substrate, a microstrip-to-slotline transition is required. At the transition the microstrip line is terminated in a radial stub and the slotline is terminated in a circular cavity as shown in Figure 2.5.

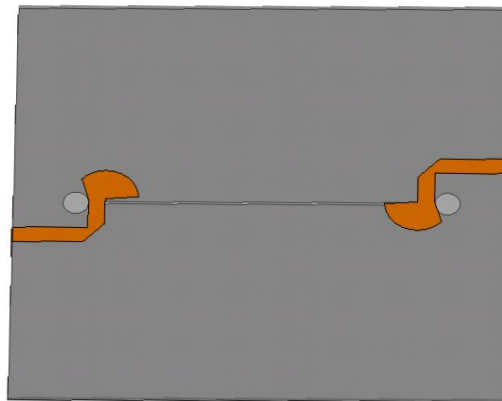


Figure 2.5: Simulation Geometry for Microstrip-fed Slotline

The radial stub and circular cavity are designed to present a virtual short circuit and virtual open circuit respectively, over a wide band of operation. The input impedance and bandwidth at the transition can be controlled by varying the radius and flare angles of the stub, the width of the slotline, and the diameter of the circular cavity [11]. A microstrip-to-slotline transition was designed such that it had better than 15 dB return loss from 6 to 11 GHz, which corresponded to the mixer bandwidth. The structure shown in Figure 2.5 was simulated in CST Microwave Studio, and a design meeting desired specs was achieved. The simulated slotline was 3 cm long and located on a 20-mil-thick Duroid substrate. The same microstrip-to-slotline transition was used in the Vivaldi elements described in Chapters 3 and 4, and dimensions are shown in Appendix B. Figure 2.6 shows the simulated return loss of the designed microstrip-fed slotline.

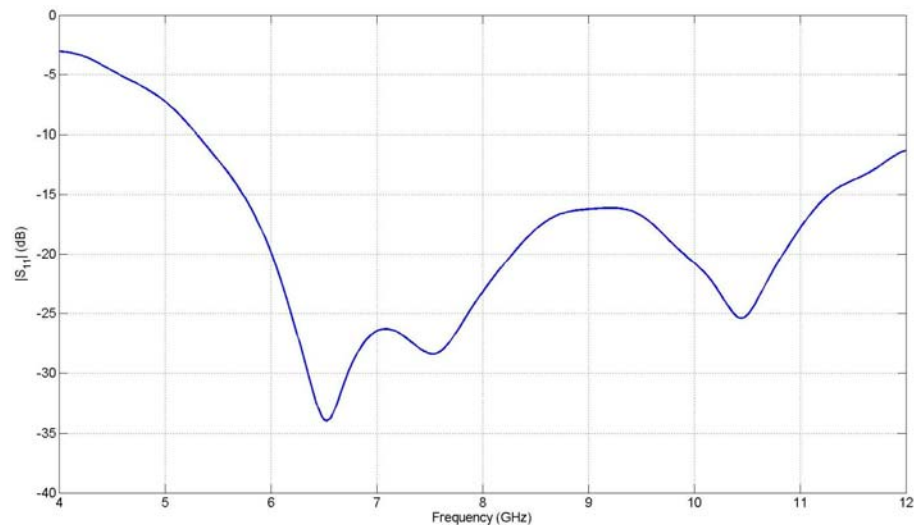


Figure 2.6: Simulated Return Loss of Microstrip-fed Slotline

Figure 2.7 illustrates the layout that was used to integrate the IC with the microstrip feed of the structure designed above.

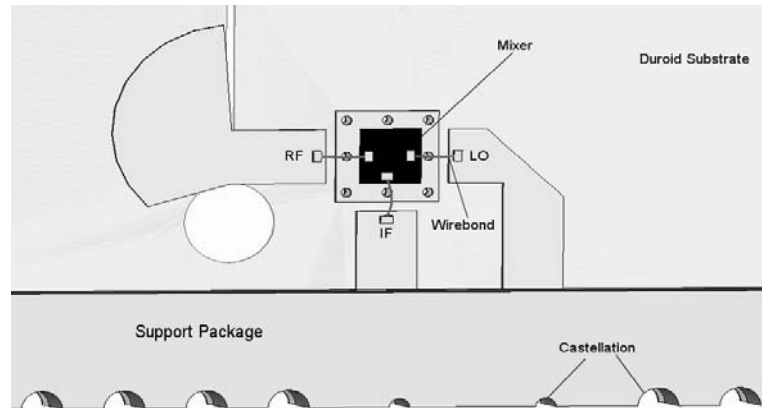


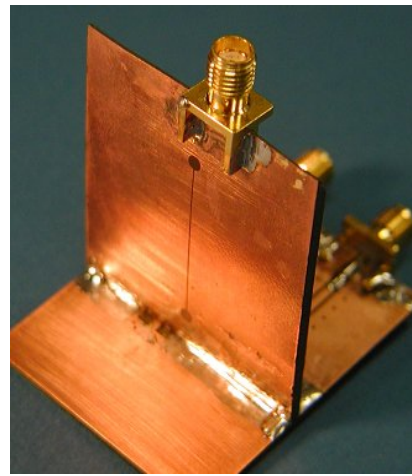
Figure 2.7: Feed Layout of Active Slotline Prototype

The mixer package was mounted onto a copper pad, which was connected to the metallization on the opposite side with vias, and served as a local ground for the IC. Microstrip feed lines for the IF and LO signals were included, and connected to lines on the motherboard with castellated vias. Note that the castellations for the IF and LO feed lines are 0.5 mm in diameter, while the other castellations are 1 mm in diameter. This was done so that the vias would fit within the width of the tapered microstrip lines, which was 0.92 mm. The RF line is a shortened version of the microstrip feed line designed above. All of the feed lines were matched to 50 ohms, which on 20-mil-thick Duroid corresponds to a width of 1.47 mm. An electrical connection between the IC and the microstrip feed lines was achieved using gold bondwires. Wirebonding is a commonly used technique, and may be carried out in automated processes. Gold-plated jumper tabs were attached to the copper lines to provide a gold-on-gold connection for wirebonding. In practice the lines could be gold plated, which would make the jumper

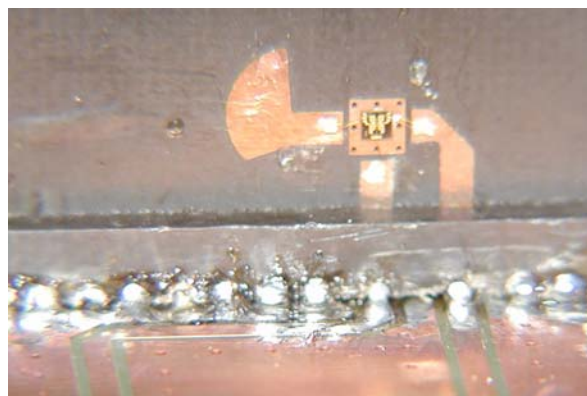
tabs unnecessary. Both the mixer and the jumper tabs were connected to the copper surface using conductive silver epoxy. The prototype was fabricated on a 20-mil-thick Rogers 5880 Duroid substrate by E-Fab, Inc. of Santa Clara, CA. In addition, a small CPW motherboard printed on FR-4 was also fabricated. The active package was soldered onto the CPW on a hotplate. A small rig was used to hold the package in place during the reflow cycle. Figure 2.8 shows images of the completed prototype.



(a)



(b)



(c)

Figure 2.8: (a) Front View; (b) Back View; (c) Close-up of Integrated Feed of Active Slotline Prototype

In order to determine the performance of the prototype, the conversion loss of the structure was measured. The conversion loss was found by taking the ratio of the input IF power, which was supplied by a network analyzer, to the output RF power, which was measured using a spectrum analyzer. A signal generator was used to supply the LO drive of 15 dBm. A plot of the conversion gain (the reciprocal of conversion loss) vs. frequency is shown in Figure 2.9.

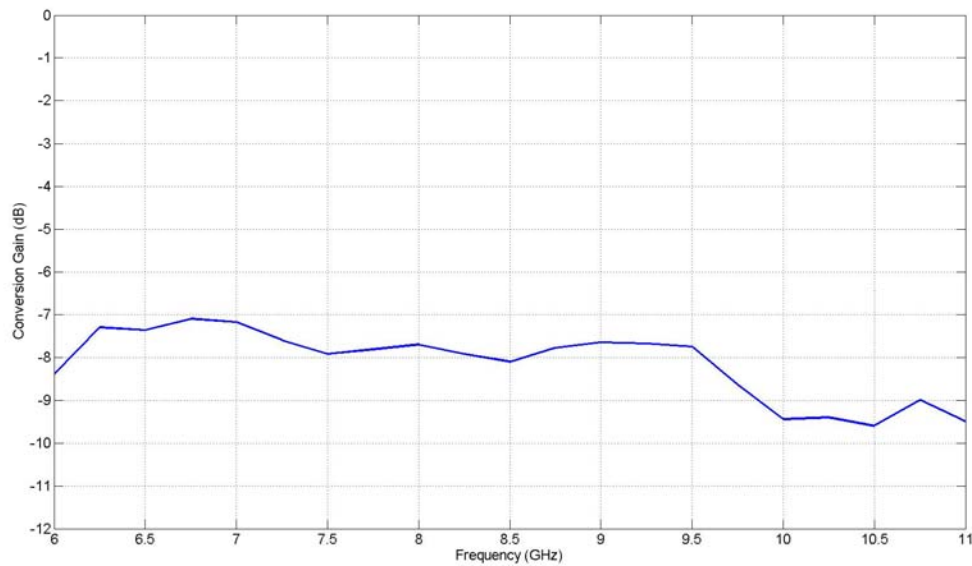


Figure 2.9: Measured Conversion Gain of Active Slotline Prototype

The measured conversion gain of the prototype is about 0.5 to 1.5 dB lower than the device conversion gain provided by the manufacturer. These discrepancies correlate well with the simulated insertion loss of the slotline structure. Therefore, it was concluded that the scheme used to integrate the mixer was acceptable for use with the Vivaldi elements.

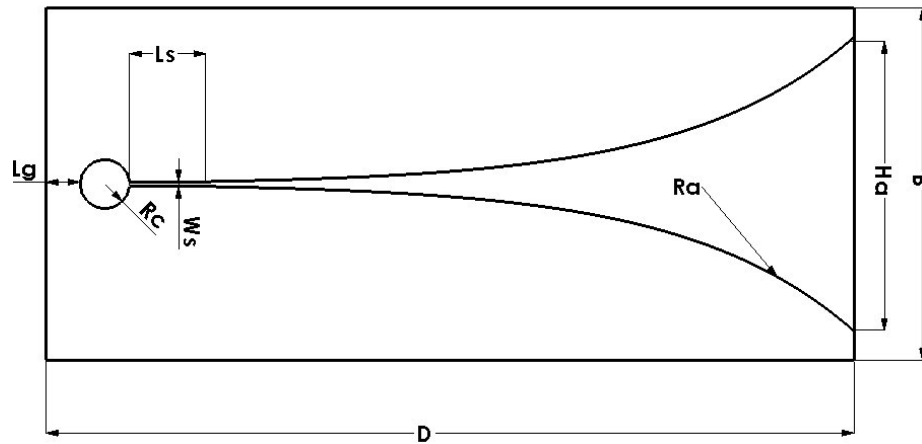
CHAPTER 3

INDIVIDUAL VIVALDI ANTENNA

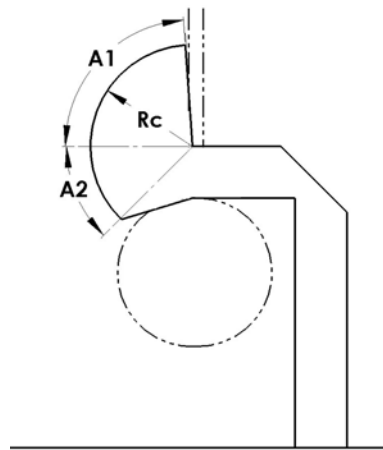
3.1 Vivaldi Design

The Vivaldi antenna is a member of a class of elements known as tapered slot antennas (TSA). TSA were introduced in 1974 by Lewis et al [12], and since then have been studied as isolated radiators and as elements in phased arrays. Essentially, TSA may be thought of as planar analogs to horn antennas. A horn antenna is implemented by the flaring of a metallic waveguide; likewise, TSA are implemented by the flaring of a slotline. As a slotline is widened, it becomes an increasingly efficient radiator. On a TSA, waves propagating on the slotline are shed into free space as they travel along the tapered section. It is this traveling wave radiation characteristic that allows TSA to operate over wide bandwidths. Many different taper profiles have been utilized for TSA; the name Vivaldi was introduced by Gibson [13] in 1979, and specifically refers to TSA with exponentially flared slots.

A single element, microstrip-fed Vivaldi antenna was designed for this thesis. A microstrip feed was chosen rather than a stripline feed so that the mixer could be integrated on the same layer as the feed lines, eliminating the need for vias to transfer signals between layers. However, unlike stripline feeds, microstrip feeds are unshielded; therefore, they are free to radiate, and may add asymmetry to a Vivaldi's radiation pattern. Also, microstrip lines are generally wider than striplines of the same impedance, and will take up more space on the structure. Figure 3.1 shows the typical layout of a microstrip-fed Vivaldi antenna.



(a)



(b)

Figure 3.1: Important Parameters for the (a) tapered slot, (b) microstrip feed of Vivaldi Antenna

The impedance and radiation characteristics of a Vivaldi antenna can be controlled by varying the parameters illustrated in Figure 3.1. Important parameters in the design of a TSA include the length of the antenna, D , and the width of the open end of the slotline, H_a . Because TSA are traveling wave antennas, they are generally multiple free space wavelengths long when used as isolated radiators. Typical values for D given in literature range between $2\lambda_0$ and $12\lambda_0$. Likewise, the width of the taper opening also

should be electrically large, and H_a is typically greater than $\lambda_0/2$ [11]. Since the mechanism of radiation in a TSA comes from the tapered slotline, the opening rate, R_a , is also a critical design parameter. As was stated, the taper profile for a Vivaldi antenna is exponential, and is given as

$$x = c_1 e^{R_a z} + c_2, \text{ where}$$

$$c_1 = \frac{x_2 - x_1}{e^{R_a z_2} - e^{R_a z_1}}, \text{ and} \quad (3.1)$$

$$c_2 = \frac{x_1 e^{R_a z_2} - x_2 e^{R_a z_1}}{e^{R_a z_2} - e^{R_a z_1}}$$

In order to excite a mode on the slotline, a microstrip-to-slotline transition, which includes the microstrip feed line and radial stub shown in Figure 3.1a, and the circular cavity shown in Figure 3.1b, is required. Such a transition was designed in Chapter 2, and was included in the Vivaldi antenna designed in this chapter.

The Vivaldi was designed to operate over a frequency range of 6 to 11 GHz, which is the bandwidth of the HMC130 mixer. The substrate was specified to be 20-mil-thick Duroid. All other parameters were free to vary, although the length was kept relatively short in order to preserve mechanical stability and to keep costs down. Simulations were performed using CST Microwave Studio. Initially, solutions were found for elements backed by an infinite ground plane. When good solutions were obtained, they were re-simulated on a finite ground plane of 12 cm x 10 cm, which was the size of the motherboard used for measurements. The primary consideration for designing the Vivaldi element was that the bandwidth requirement was met. It was also desirable to have patterns which were well-formed, but specific performance requirements such as beamwidth and sidelobe levels were not set. Figure 3.2 shows the

simulated return loss for the designed Vivaldi antenna on both finite and infinite ground planes.

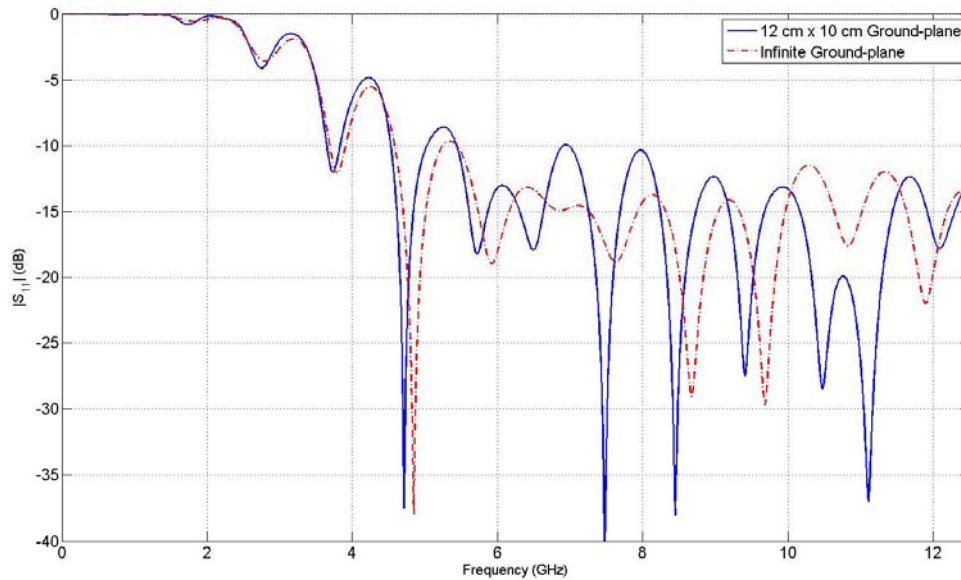


Figure 3.2: Simulated Return Loss of Isolated Vivaldi Element

The designed Vivaldi exhibits better than 10 dB return loss from about 5 GHz to greater than 12.5 GHz. The bandwidth for an element on a finite ground plane is roughly the same as that for an element on an infinite ground; however, the element on the infinite ground plane has generally lower return loss within the band of operation. The radiation patterns for this element are shown in section 3.3.1, and are compared with measured results. Since the designed element met the bandwidth requirement, it was considered an acceptable design for fabrication.

3.2 Fabrication and Assembly

The Vivaldi packages were fabricated by E-Fab, Inc. The feed layout for the passive element was as shown in Figure 3.1b and the feed layout for the active element was

similar to the layout used for the active slotline prototype described in Chapter 2. Full dimensioned drawings of the packages are included in Appendix B. A CPW motherboard was fabricated on a FR-4 substrate. The antenna and its motherboard are shown in Figure 3.3.

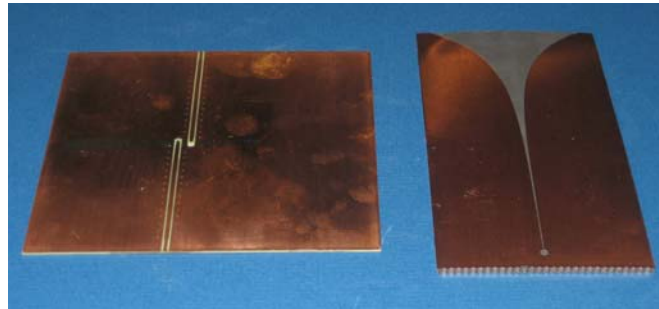


Figure 3.3: Fabricated Vivaldi Element and Motherboard

It was found that the 20 mil thick Duroid substrate was very flexible, and that the copper lamination caused the antenna to warp noticeably.

A more refined process was used to mount the Vivaldi Antennas than was used assemble the prototypes described in Chapter 2. Rather than using a fixed rig on a stationary hotplate, the antenna was assembled on a conveyor-belt, which ran over a hotplate. The hotplate consisted of multiple sections that were heated to a different temperature. Solder-paste was applied to the castellations, and the Vivaldi packages were held in place on the motherboard using clips. The moving setup was designed to approximate the ideal temperature profile for reflowing solder. In addition, it allowed the amount of time the IC was exposed to high temperatures to be minimized. Images of an assembled antenna-motherboard structure are shown in Figure 3.4 and Figure 3.5.

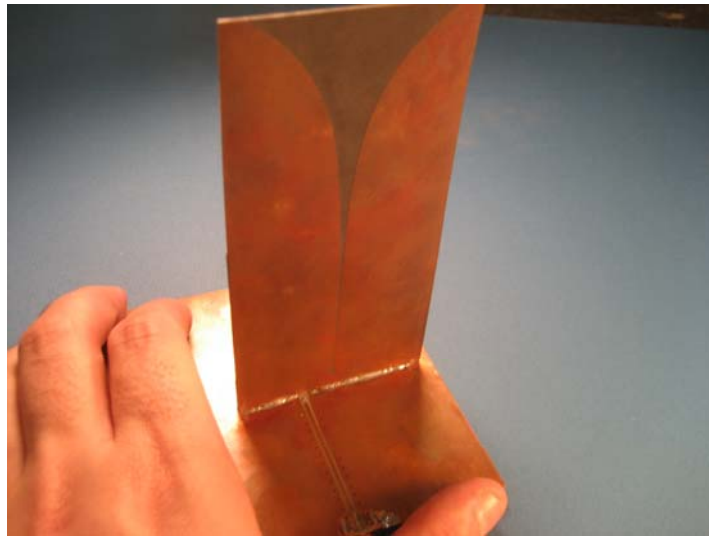


Figure 3.4: Vivaldi Antenna Mounted on CPW Motherboard

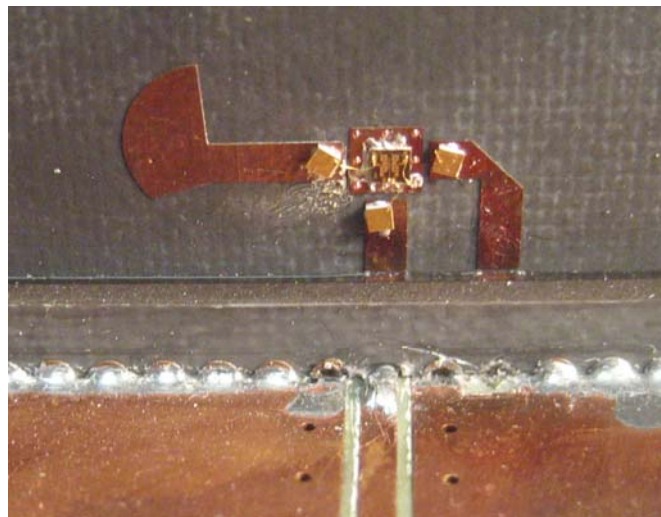


Figure 3.5: Close-up of Castellated Interconnection for Active Vivaldi Antenna Package

3.3 Measurements

In order to validate the simulation solutions, and to compare the performances of the passive and active Vivaldi elements, the return loss and radiation patterns were measured for the fabricated antennas.

3.3.1 Passive Vivaldi Measurements

The return loss of the passive Vivaldi antenna was measured in order to validate the computational results. Time-windowing was applied in order to remove reflections caused by the SMA connector from the measurement. Because the orthogonal CPW-to-microstrip transition is located close to the Vivaldi's microstrip feed, it was not possible to window it out of the measurements. The measured return loss is compared to the simulated return loss (on a finite ground plane) in Figure 3.6.

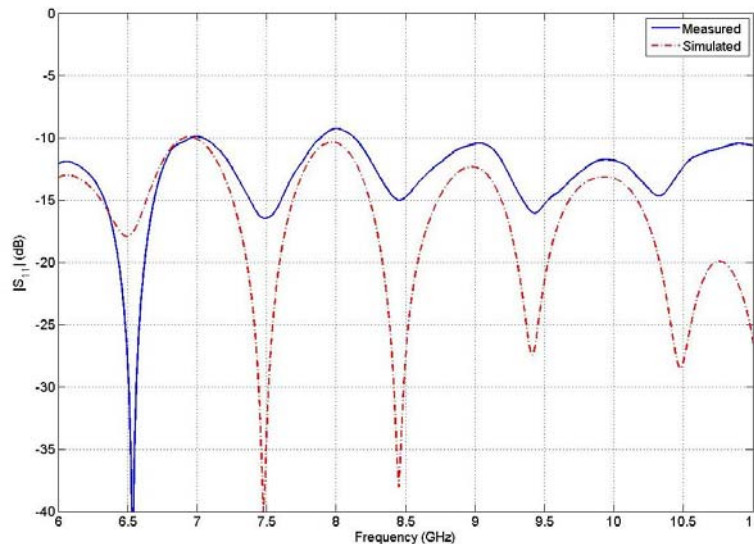


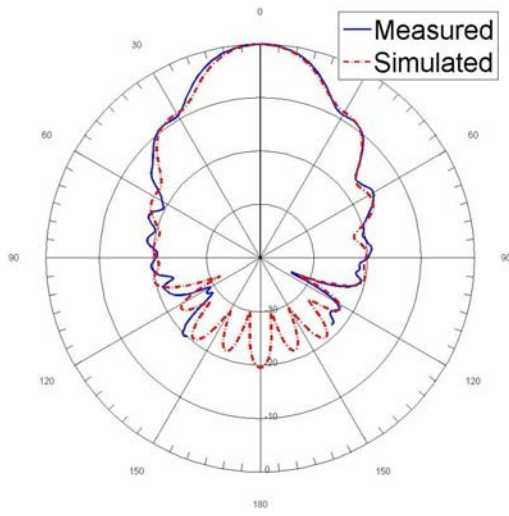
Figure 3.6: Measured Return Loss of Passive Vivaldi Antenna

There is fairly good agreement between the measured and simulated results. The peaks and nulls generally agree, although the measured return loss is higher than the simulated return loss. This discrepancy can be attributed to reflections from the CPW-microstrip transition.

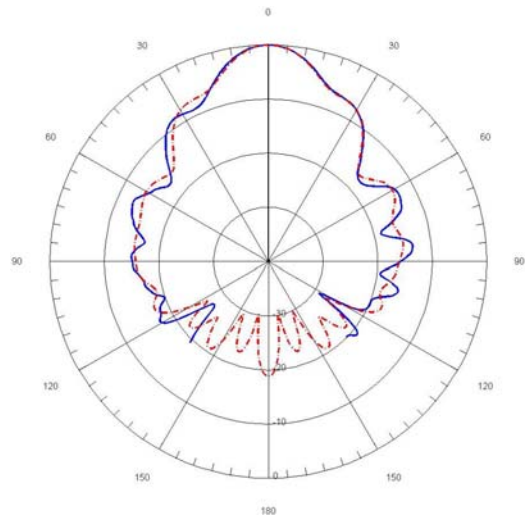
In addition to return loss, both the co-polarization and the cross-polarization far-field radiation patterns were measured. The AUT (antennas under test) was used as a receive antenna, while the probe antenna was the transmit antenna. The probe antennas were C-band and X-band open-ended waveguides (OEWG). The AUT was mounted on a rotary arm, and was separated from the probe antenna by a distance of 48 inches (1.22 meters). An antenna's far-field is defined as the region where the radial component of the antenna's radiated field is small enough to be considered negligible. The radial distance from an antenna to its far-field is given as

$$R_{ff} = \frac{2D^2}{\lambda} \quad (3-1)$$

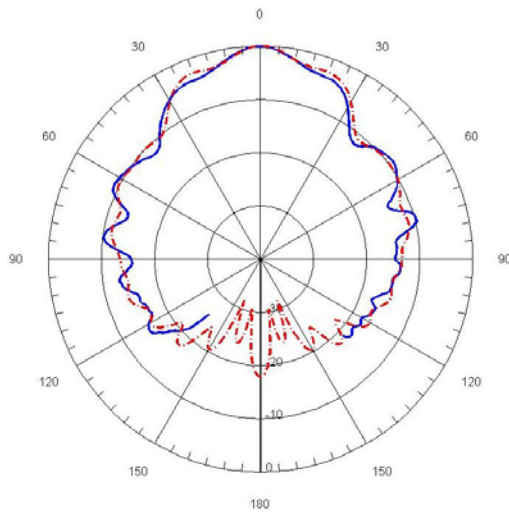
where D is the largest physical dimension of the antenna, and λ is the free space wavelength. The largest dimension of the Vivaldi antenna was its height, which was 12.0 cm. At the highest frequency of operation (11 GHz) the free space wavelength was 2.72 cm. Given these values, R_{ff} is 1.06 meters; therefore, the AUT to probe spacing was sufficient for a far-field measurement. Figure 3.7 and Figure 3.8 are plots which compare the measured far-field co-polarization patterns with simulated patterns for the E-plane and H-plane respectively. The simulated patterns were computed for a Vivaldi with a finite ground plane of 12 cm x 10 cm.



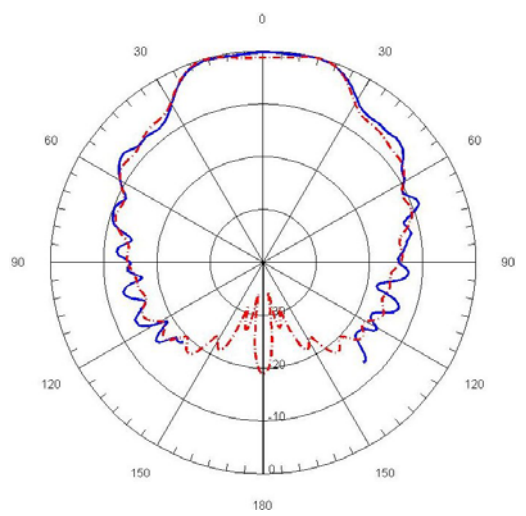
(a)



(b)

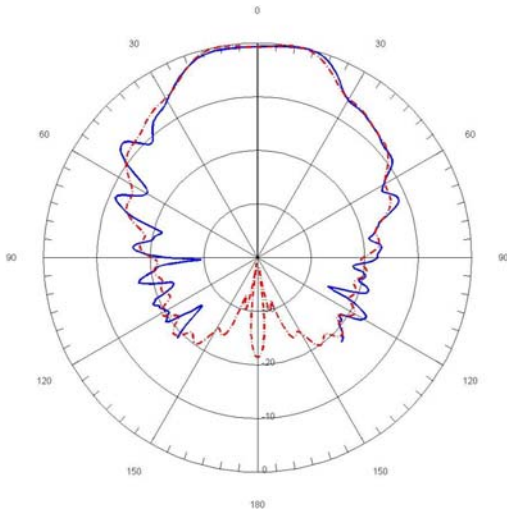


(c)

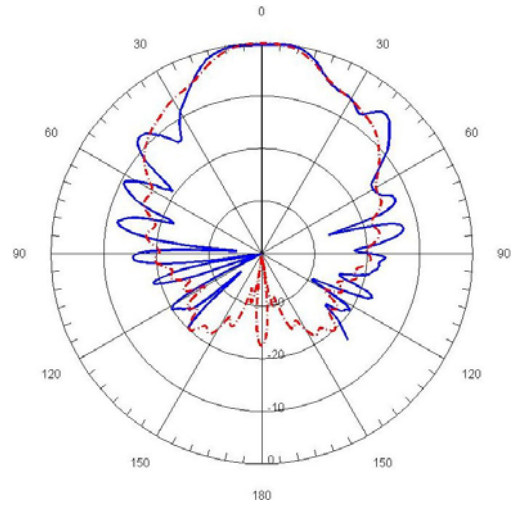


(d)

Figure 3.7: Measured vs. Simulated E-Plane Co-polarized Radiation Patterns of Passive Isolated Vivaldi Element at: (a) 6 GHz; (b) 7 GHz; (c) 8 GHz; (d) 9 GHz; (e) 10 GHz; (f) 11 GHz (**Continued next page**)

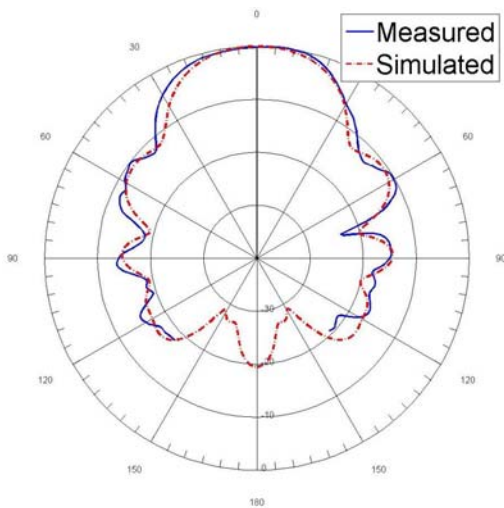


(e)

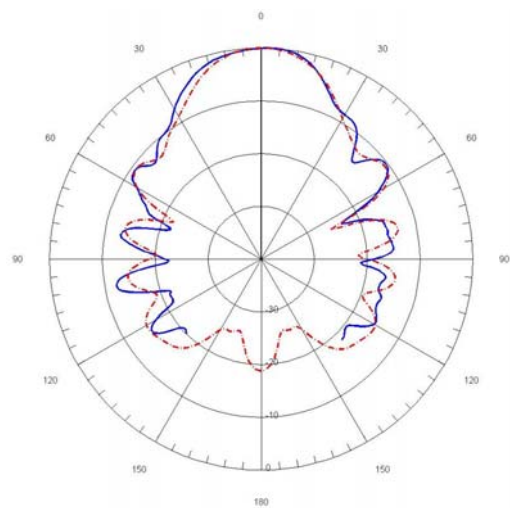


(f)

Figure 3.7, continued: Measured vs. Simulated E-Plane Co-polarized Radiation Patterns of Passive Isolated Vivaldi Element at: (a) 6 GHz; (b) 7 GHz; (c) 8 GHz; (d) 9 GHz; (e) 10 GHz; (f) 11 GHz



(a)



(b)

Figure 3.8: Measured vs. Simulated H-Plane Co-polarized Radiation Patterns of Passive Isolated Vivaldi Element at: (a) 6 GHz; (b) 7 GHz; (c) 8 GHz; (d) 9 GHz; (e) 10 GHz; (f) 11 GHz
(Continued next page)

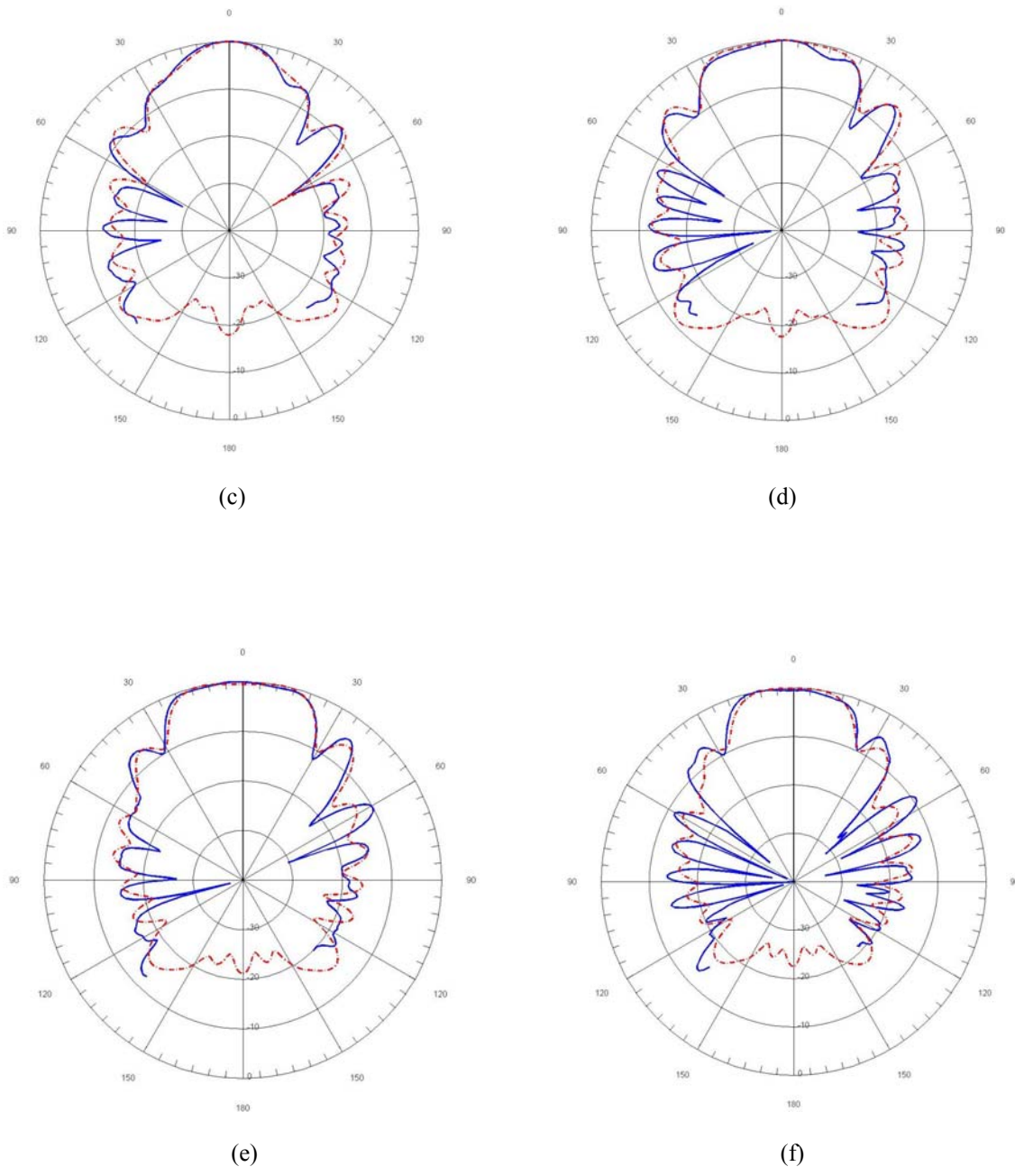


Figure 3.8, continued: Measured vs. Simulated H-Plane Co-polarized Radiation Patterns of Passive Isolated Vivaldi Element at: (a) 6 GHz; (b) 7 GHz; (c) 8 GHz; (d) 9 GHz; (e) 10 GHz; (f) 11 GHz

Although there is fairly good agreement between the measured and simulated results, some discrepancies exist, especially at higher frequencies. In both principle planes, the measured patterns display increased asymmetry and sidelobe levels relative to the

simulated patterns as frequency is increased. These discrepancies are likely due to spurious radiation from the antenna's CPW feed line. Additionally, the patterns may be affected by the bend in the antenna caused by the flexible substrate, and the metallic pedestal on which the antenna was mounted.

3.3.2 Active Vivaldi Measurements

In order to evaluate the performance of the active Vivaldi element, its far-field radiation pattern was measured for several frequencies. Because the measurement involved a conversion in frequency, the measurement loop shown in Figure 3.9 was used. The AUT was used as a receive antenna, and the received signal was downconverted to IF. In order to ensure the signal that the PNA receives is at the same frequency as the transmitted signal, an external mixer was added to the loop to upconvert the IF output from the AUT back to RF.

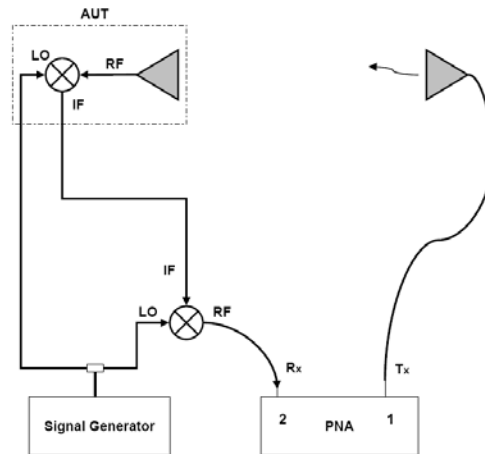


Figure 3.9: Schematic of Setup Used to Measure Active Antenna

The measured patterns for the active Vivaldi element are shown in Figure 3.10 and Figure 3.11.

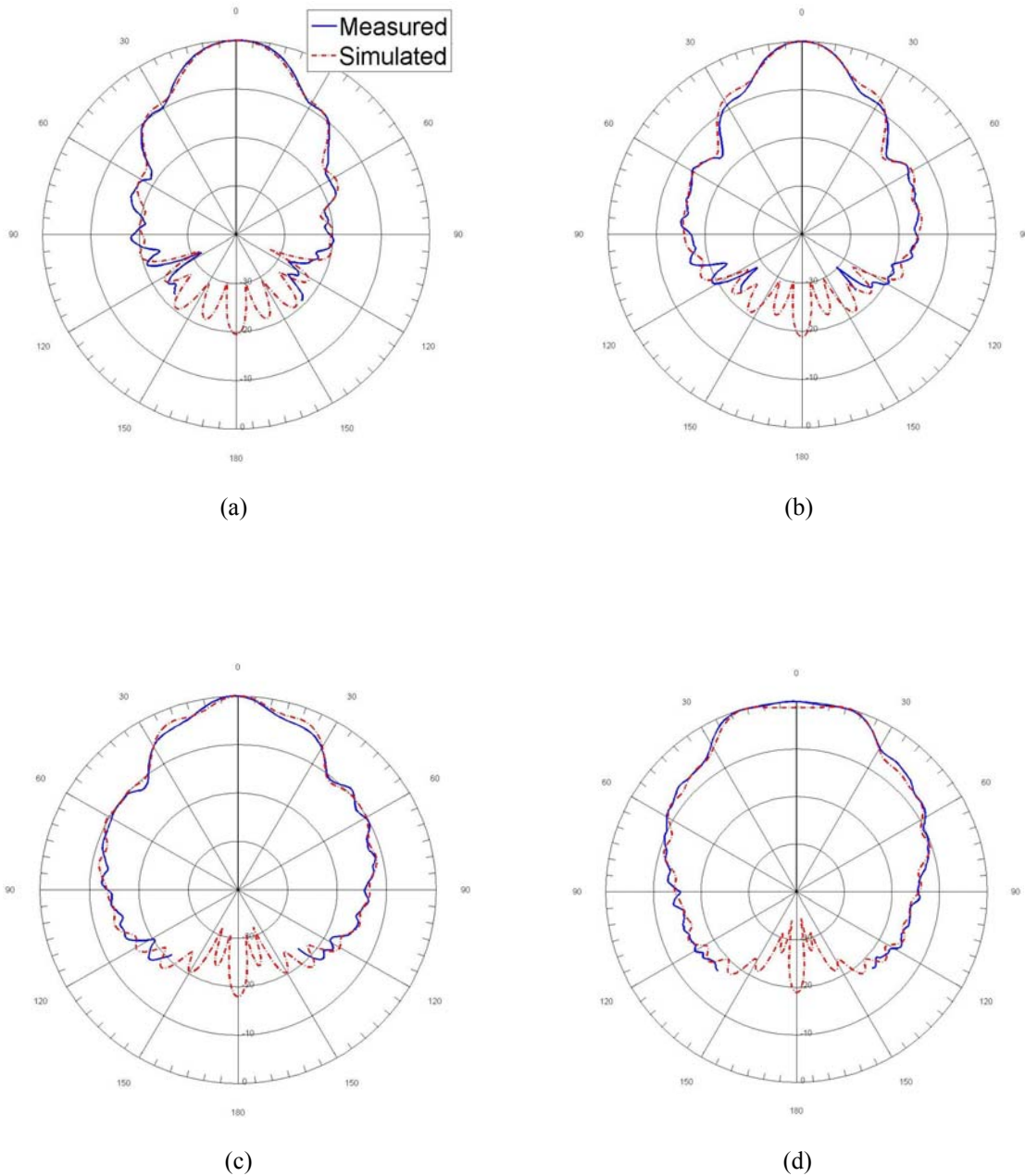
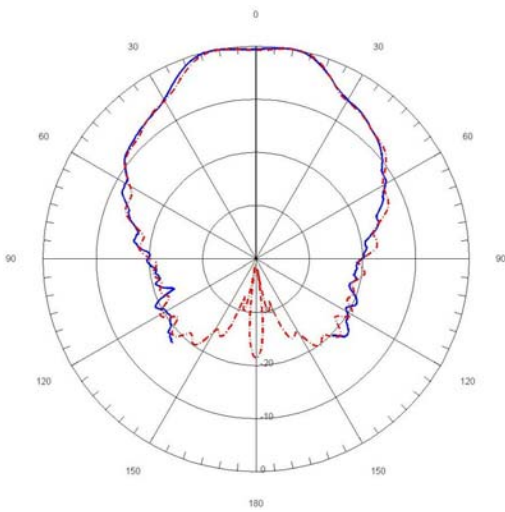
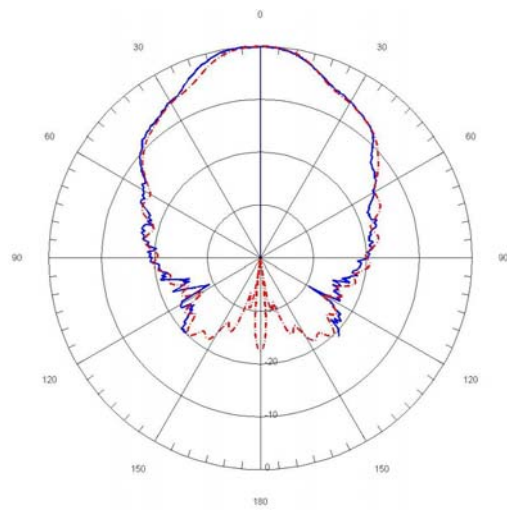


Figure 3.10: Measured vs. Simulated E-Plane Co-polarized Radiation Patterns of Active Isolated Vivaldi Element at: (a) 6 GHz; (b) 7 GHz; (c) 8 GHz; (d) 9 GHz; (e) 10 GHz; (f) 11 GHz
(Continued next page)

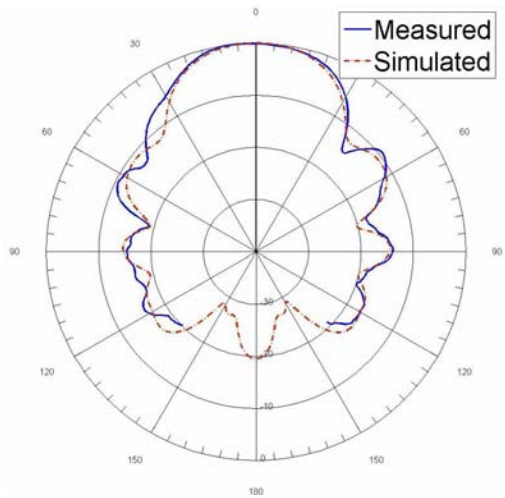


(e)

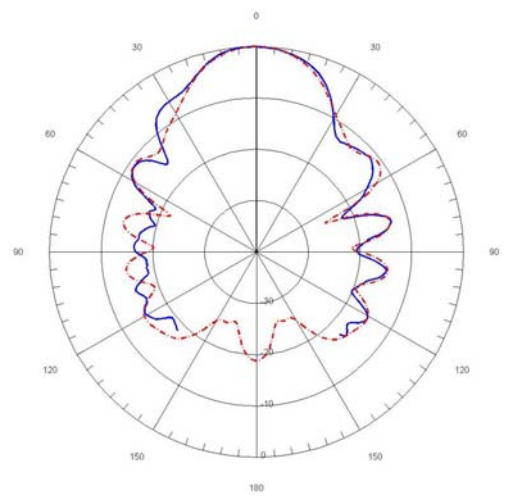


(f)

Figure 3.10, continued: Measured vs. Simulated E-Plane Co-polarized Radiation Patterns of Active Isolated Vivaldi Element at: (a) 6 GHz; (b) 7 GHz; (c) 8 GHz; (d) 9 GHz; (e) 10 GHz; (f) 11 GHz



(a)



(b)

Figure 3.11: Measured vs. Simulated H-Plane Co-polarized Radiation Patterns of Active Isolated Vivaldi Element at: (a) 6 GHz; (b) 7 GHz; (c) 8 GHz; (d) 9 GHz; (e) 10 GHz; (f) 11 GHz
(Continued next page)

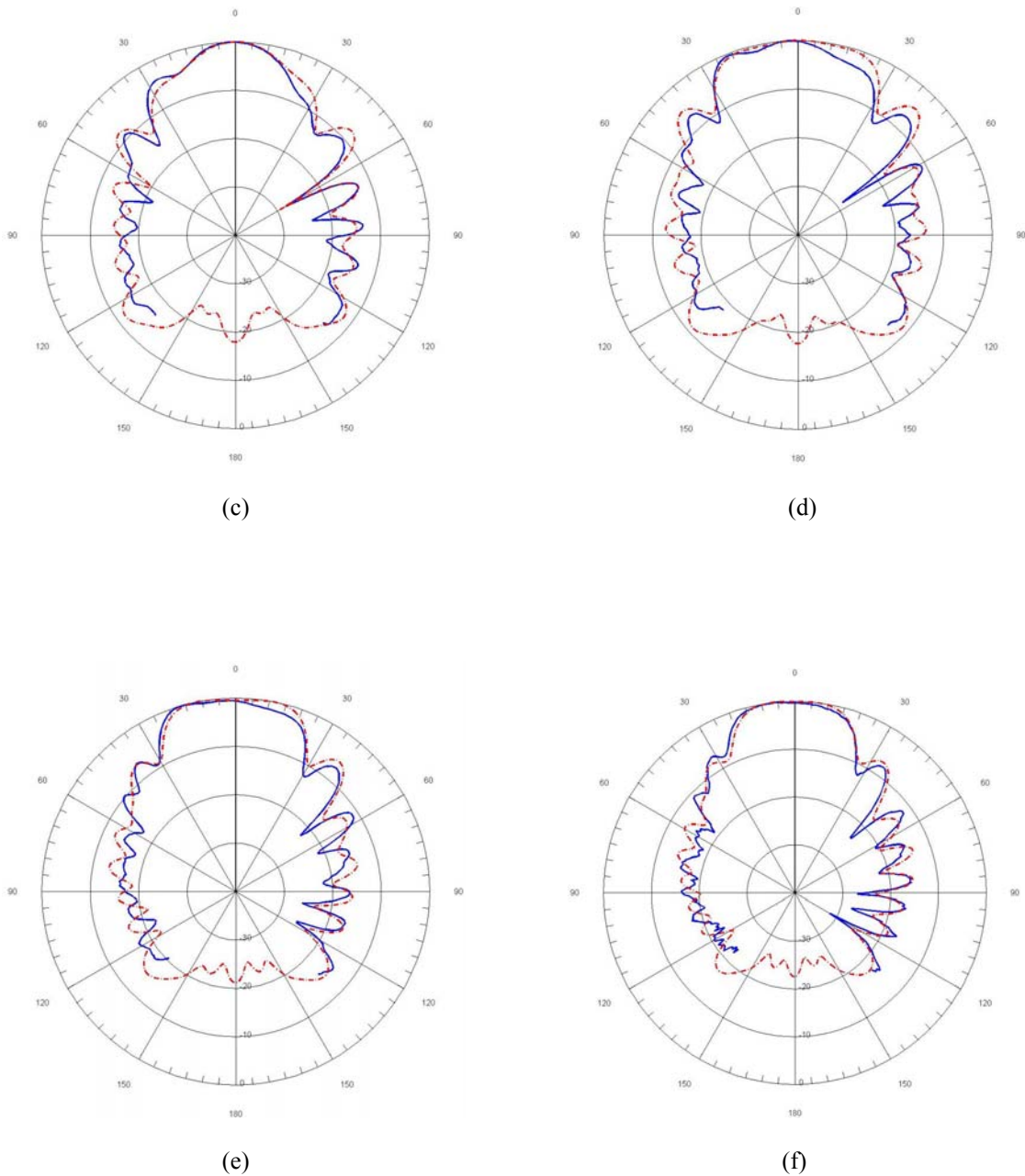


Figure 3.11, continued: Measured vs. Simulated H-Plane Co-polarized Radiation Patterns of Active Isolated Vivaldi Element at: (a) 6 GHz; (b) 7 GHz; (c) 8 GHz; (d) 9 GHz; (e) 10 GHz; (f) 11 GHz

In general, there is good agreement between the measured patterns for the active Vivaldi antenna and the simulated data. The measured E-plane patterns of the active Vivaldi antenna match the simulated data better than the same measurements for the passive Vivaldi, especially at 10 GHz and 11 GHz. The H-plane patterns also agree

fairly well, although there is some asymmetry in the main beam. It is possible that this asymmetry is caused by the bend of the antenna, as well as the metallic pedestal backing the antenna.

3.3.3 Comparison of Active and Passive Elements

One of the primary advantages of using active antennas is that frequency conversion takes place at the antenna, eliminating transmission through lossy feed networks. As was explained in Chapter 1, integrating a mixer at the antenna should help improve the efficiency of a system, as well as reduce spurious radiation from feed lines. In this section, the efficiencies and radiation patterns of the passive Vivaldi element and the active Vivaldi element will be compared.

The difference in efficiency between the passive and active elements was determined by comparing $|S_{21}|$, which was measured for each element in the far-field range. The AUT were separated from the probe antennas by a distance of approximately 1.2 meters. A C-band OEWG was used as the probe antenna for measurements from 6-8GHz, and an X-band OEWG was used for measurements from 9-11GHz. As was noted, the setups used to measure the passive and active elements differed, as such, each measurement loop contained different sources of loss. Although both setups used the same RF cables, the passive loop contained an extra length of RF cable. In the active loop, the external mixer and the IF cable in the setup shown in Figure 3.9 added loss to that measurement. The cable losses and the conversion loss of the external mixer were measured, and the $|S_{21}|$ measurements were adjusted accordingly. Measurements were taken for several RF frequencies, with the IF held constant at 100 MHz. The results of the measurements for both the passive and active

elements are shown in Table 3.1. The value Δ is the difference between the $|S_{21}|$ values of the active and passive configurations. Additionally, the insertion loss of a CPW line with same dimensions as the feed for the passive Vivaldi antenna was measured, and the results are included in Table 3.1, as are estimated values of the mixer conversion loss, which were obtained from the device datasheet.

Table 3.1: Comparison of Passive and Active Vivaldi Elements

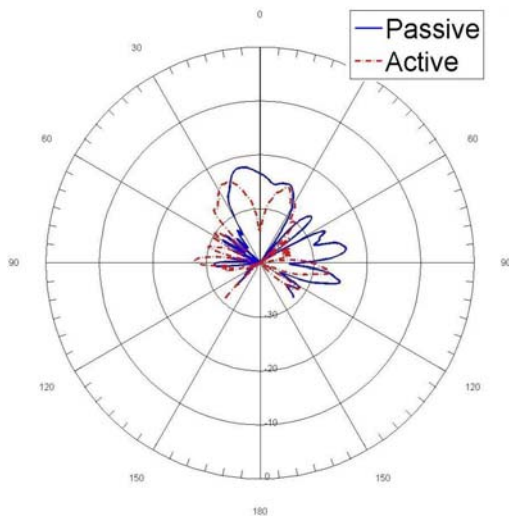
Frequency	$ S_{21} $ (Passive Antenna)	$ S_{21} $ (Active Antenna)	Δ	Mixer Conversion Loss	CPW Insertion Loss
6.0 GHz	-31.2 dB	-37.3 dB	-6.1 dB	8.0 dB	1.6 dB
7.0 GHz	-33.0 dB	-37.3 dB	-4.3 dB	7.3 dB	1.8 dB
8.0 GHz	-34.0 dB	-38.2 dB	-4.2 dB	6.8 dB	2.1 dB
9.0 GHz	-40.5 dB	-44.4 dB	-3.9 dB	6.8 dB	2.4 dB
10.0 GHz	-39.8 dB	-44.1 dB	-4.3 dB	6.8 dB	3.0 dB
11.0 GHz	-39.7 dB	-44.5 dB	-4.8 dB	7.3 dB	3.3 dB

In order to check the results obtained, the mixer conversion loss was added to Δ , while the CPW insertion loss was subtracted, and the calculated totals were found to be within +/- 1 dB. Theoretically, the total difference between the two antenna configurations when all losses are considered should be close to 0 dB. The +/- 1 dB differences may be the result of drift between measurements, as well as differences between the actual mixer conversion loss and the estimated values. In general, the results indicate that the active configuration has a higher efficiency than the passive configuration once conversion loss is taken into account. This improvement in efficiency is the result of frequency conversion at the antenna, which allows for the transmission of a low-

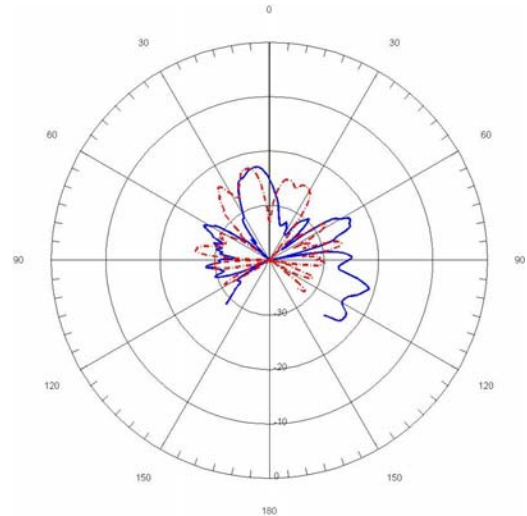
frequency IF signal through the antenna's lossy CPW feed line, rather than a high-frequency RF signal.

As was stated previously, frequency conversion at the Vivaldi element should help improve the overall radiation patterns of the prototype structure. The results shown in the previous two sections demonstrate that the measured co-polarization patterns for the active antenna configuration agree better with the simulated patterns than do the patterns for the passive configuration. The patterns for the passive configuration are likely affected by radiation leaking from the microstrip and CPW feed lines. Because downconversion takes place at the antenna in active configuration, the amount of transmission line over which the RF signal must propagate is limited, as a result, the source of spurious radiation, is significantly reduced.

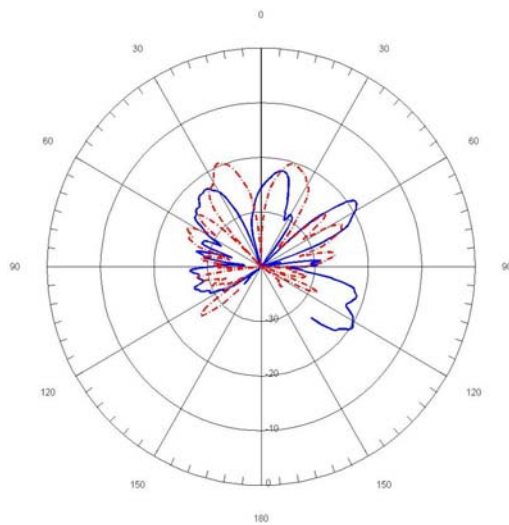
Another effect of the antennas' feed lines is to introduce asymmetry into the structures. Such asymmetry has the effect of increasing cross-polarization levels. The cross-polarized radiation patterns were measured for both the passive and active Vivaldi configurations. Figure 3.12 and Figure 3.13 show comparisons between the measured cross-polarization patterns of the two configurations.



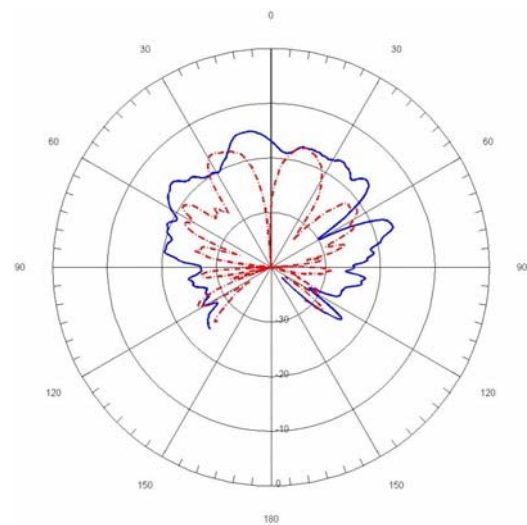
(a)



(b)



(c)



(d)

Figure 3.12: E-Plane Cross-polarized Radiation Patterns of Passive and Active Isolated Vivaldi Elements at: (a) 6 GHz; (b) 7 GHz; (c) 8 GHz; (d) 9 GHz; (e) 10 GHz; (f) 11 GHz
(Continued next page)

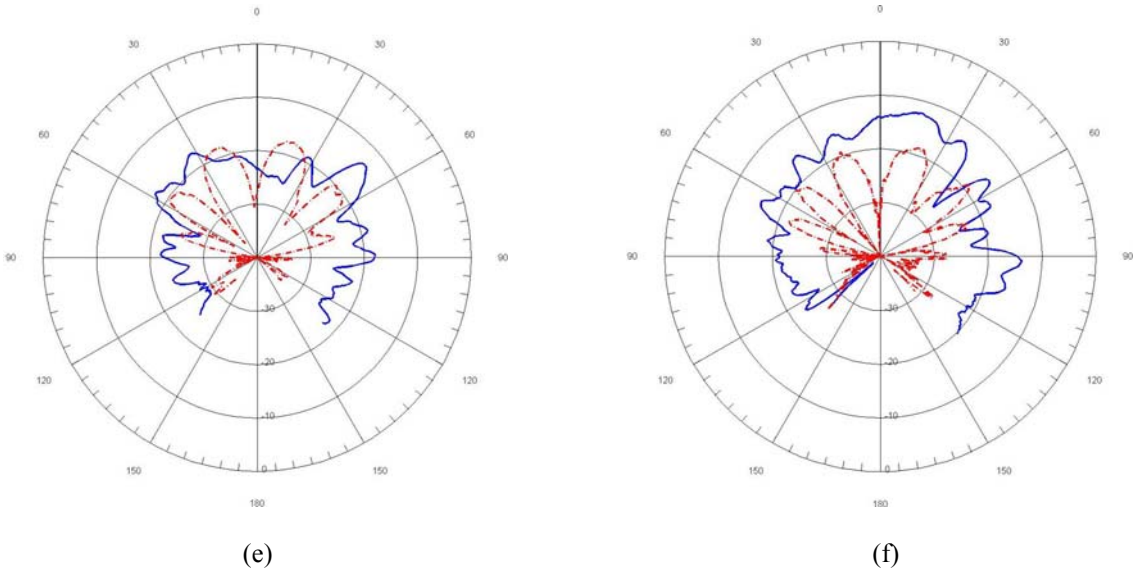


Figure 3.12, continued: E-Plane Cross-polarized Radiation Patterns of Passive and Active Isolated Vivaldi Elements at: (a) 6 GHz; (b) 7 GHz; (c) 8 GHz; (d) 9 GHz; (e) 10 GHz; (f) 11 GHz

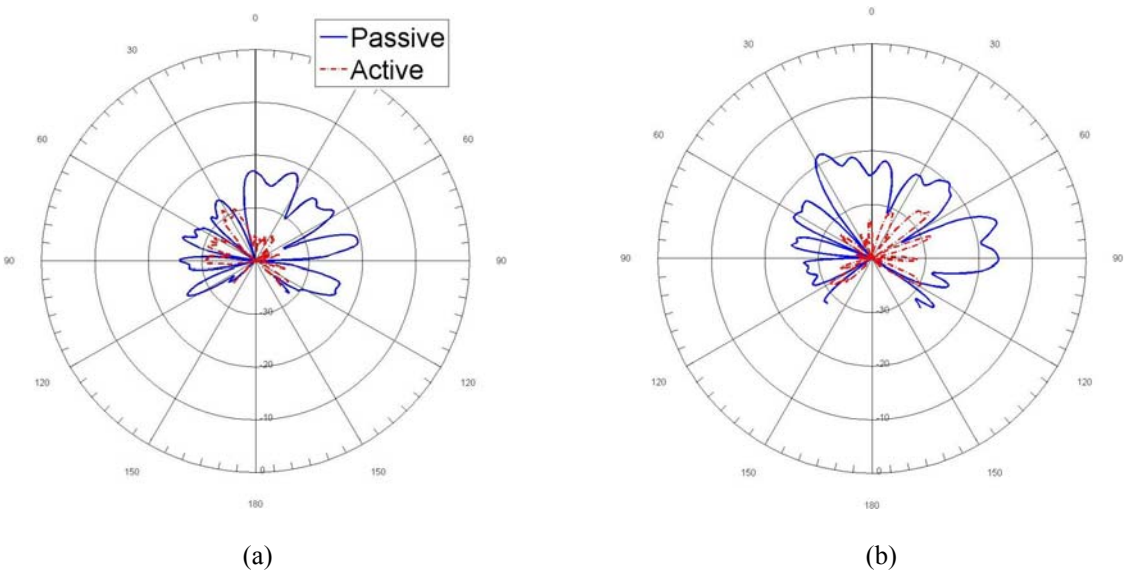
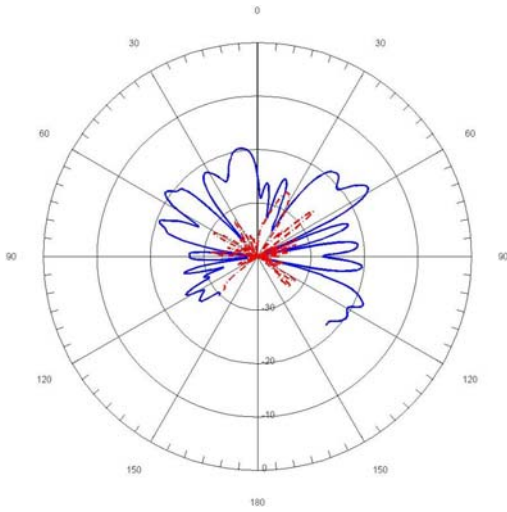
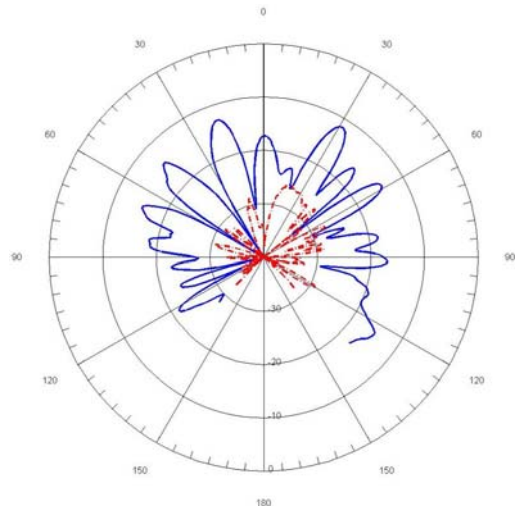


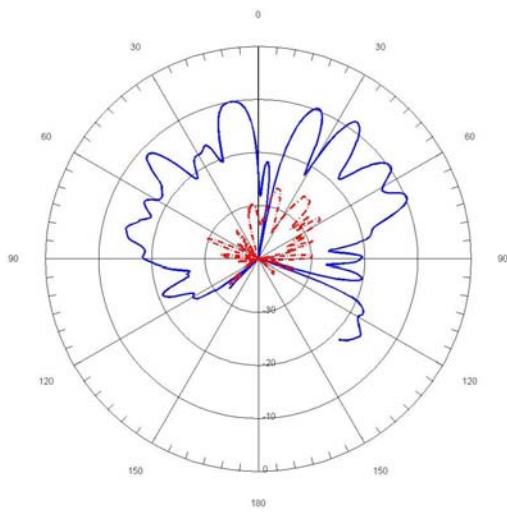
Figure 3.13: H-Plane Cross-polarized Radiation Patterns of Passive and Active Isolated Vivaldi Elements at: (a) 6 GHz; (b) 7 GHz; (c) 8 GHz; (d) 9 GHz; (e) 10 GHz; (f) 11 GHz
(Continued next page)



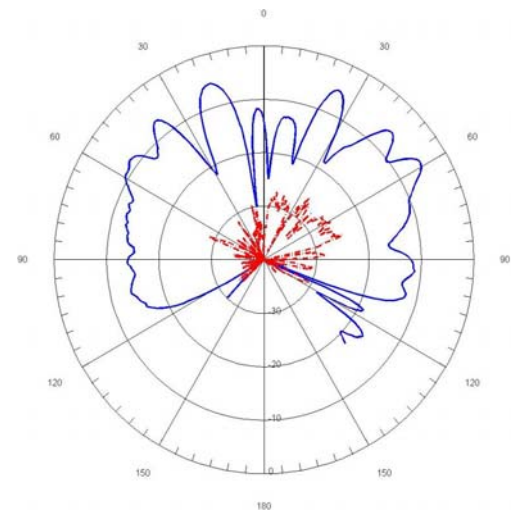
(c)



(d)



(e)



(f)

Figure 3.13, continued: H-Plane Cross-polarized Radiation Patterns of Passive and Active Isolated Vivaldi Elements at: (a) 6 GHz; (b) 7 GHz; (c) 8 GHz; (d) 9 GHz; (e) 10 GHz; (f) 11 GHz

In the E-plane, the peak cross-polarization level of the passive Vivaldi is generally higher than that of the active element. Radiation from the radial stub is most likely the primary source of cross-pol for the active element in the E-plane. In the passive configuration, the microstrip feed also radiates at the RF frequency, thereby leading to the higher cross-pol. In the H-plane, the cross-polarization is much higher for the passive configuration, which is most likely caused by radiation from the CPW feed line. In the active configuration, the CPW feed lines carry LO and IF signals, and therefore, do not contribute to the RF radiation patterns at the measurement frequency. The high frequency LO signal will introduce significant cross-pol at that frequency. However, in practice an oscillator could also be integrated, thereby limiting all high frequency signals to the antenna package.

3.4 Summary

The results obtained demonstrate the viability of the active Vivaldi element configuration. In general, the active configuration was shown to exhibit improvements in both efficiency and radiation patterns over the passive configuration. For this project, the analysis of the isolated element was performed primarily as the first step in designing an array of elements. However, there are a number of applications that make use of isolated Vivaldi elements. Such applications would most likely require elements with better bandwidth and radiation characteristics than the element presented here. The Vivaldi element designed in this thesis had slightly more than an octave of bandwidth, which appeared to be limited by the bandwidth of the microstrip-to-slotline transition. Additionally, the antenna's sidelobe levels are fairly high, and its gain varies

substantially as a function of frequency. One method that has been shown to improve the radiation characteristics of isolated TSA elements is the incorporation of corrugated slots along the edges of the antenna [14]. The Vivaldi element from this thesis was resimulated with corrugations, and the antenna's radiation patterns improved substantially. The results of the simulations are presented in more detail in Appendix A.

CHAPTER 4

ACTIVE VIVALDI ARRAY

4.1 Array Design

4.1.1 Background

Arrays of Vivaldi antennas have been widely studied due to their broad bandwidth and good performance at wide scan angles. Tapered Slot Antennas were first proposed as elements for phased arrays by Lewis et. al in 1974 [12]. Vivaldi elements couple strongly when located in an array environment; therefore, mutual coupling has a dominant effect on the performance of a Vivaldi array. As a result, the design of Vivaldi antennas as an array element may be very different from the design of an isolated element. Elements which perform poorly on their own may operate very well when used in an array. For instance, while isolated Vivaldi elements are multiple wavelengths long, array elements may be one wavelength or less [15]. Although mutual coupling is desirable from a performance standpoint, it complicates the analysis of Vivaldi arrays. Full wave analyses are the only way to accurately compute the effects of coupling, and because Vivaldi elements are electrically large, even small arrays can be computationally demanding to analyze. For that reason, Vivaldi elements are often simulated in an infinite array using a periodic boundary condition. Infinite array analysis is often a very good approximation for large arrays, but it has been shown [17] that truncation effects may be severe in small arrays of Vivaldi antennas. For the design of the array in this thesis, elements were first simulated in an infinite array environment, and then a finite array of the elements was simulated.

4.1.2 Design of 8x1 Linear Array

The design specs for the array were established such that the finished product would provide a good demonstration of concept without being excessively difficult and expensive to fabricate. It was decided that an 8x1 element linear array would be a good demonstration, while still being a feasible prototype to construct. As was the case for the isolated Vivaldi element, the array was designed to have 2:1 VSWR bandwidth from 6-11 GHz. Additionally, it was designed such that it was capable of an E-plane scan of 40 degrees from broadside.

In [4] Kasturi designed and built a 16x15 planar array of stripline-fed Vivaldi elements. For reference, a 16x1 linear subarray was removed from the array, and active reflection coefficients of elements in the array were found empirically. The active reflection coefficient provides a measure of the reflection coefficient for an element in an array in which all elements are driven. For a uniformly-lit, N-element linear array, the active reflection coefficient of an element with index m is given as [16].

$$\Gamma_m^a = \sum_{n=1}^N S_{mn} e^{-jkn d_x \sin \theta_o} \quad (4.1)$$

where S_{mn} are the n-port scattering parameters of the array, k is the free space wavenumber, d_x is the linear spacing between elements, and θ_o is the scan angle. Figure 4.1 shows the active reflection coefficient for a central element in the linear array, which was calculated from measured S-parameters.

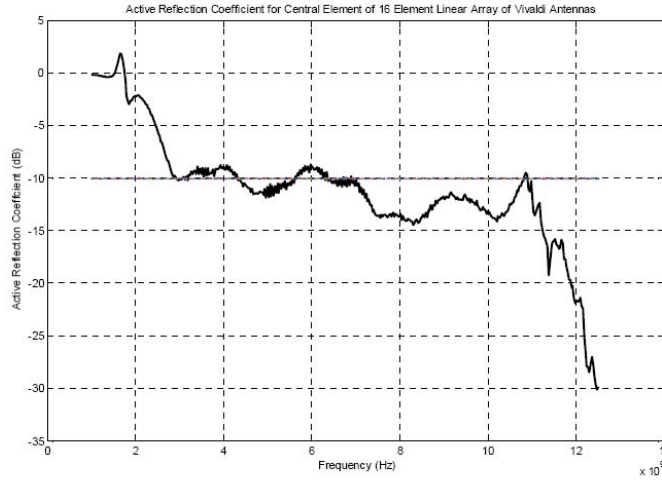


Figure 4.1: Measured Active Reflection Coefficient for Central Element in 16x1 Array of Vivaldi Antennas (see [4] for Array Dimensions)

The measurements demonstrated that the 16x1 linear array operates well from 3 to 12 GHz. It was concluded that the linear subarray represented a good baseline from which to design the 8x1 array for this project.

Like the isolated element, the array elements were designed to be microstrip-fed Vivaldi antennas with 20 mil thick Duroid substrates. As such, the microstrip-to-slotline transition designed in Chapter 2, and incorporated on the isolated element, was also utilized to feed the array elements. The 16x1 array described above was used to provide a basis for the dimensions of the antennas' height, aperture width, and opening rate. The width of the antenna modules was designed such that the elements could be spaced close enough to avoid grating lobes, while providing enough space to fit the mixer IC and feed lines. In order to prevent grating lobes, elements must be spaced less than a certain distance, d_{\max} , which is given as [18]

$$d_{\max} = \frac{\lambda_o}{1 + \sin \theta_o} \quad (4-2)$$

where λ_o is the free space wavelength at the highest frequency of operation, and θ_o is the maximum scan angle. The maximum operating frequency of the array was specified to be 11 GHz and the maximum scan angle was specified to be 40 degrees from broadside. Using these values, the maximum allowable spacing was found to be 16.3 mm. The layout of the Vivaldi packages, which is described in more detail in section 4.2.1, was designed such that the inter-element spacing was 15 mm, which is less than d_{\max} . With 15 mm spacing, the grating lobe frequency for a 40 degree scan is 12.1 GHz.

Simulations for both infinite and finite array setups were performed in Ansoft HFSS, a commercially available software package which utilizes the Finite Element Method (FEM). Infinite array simulations are less computationally intensive than finite array simulations; therefore, the array elements were initially designed in an infinite array. Also, since a practical array would consist of many more elements than the 8x1 array designed for this project, the infinite array results may be useful for a future design of a large array of these elements. Figure 4.2 shows the computed active reflection coefficient for an infinite linear array of electrically-connected Vivaldi antennas aimed at broadside.

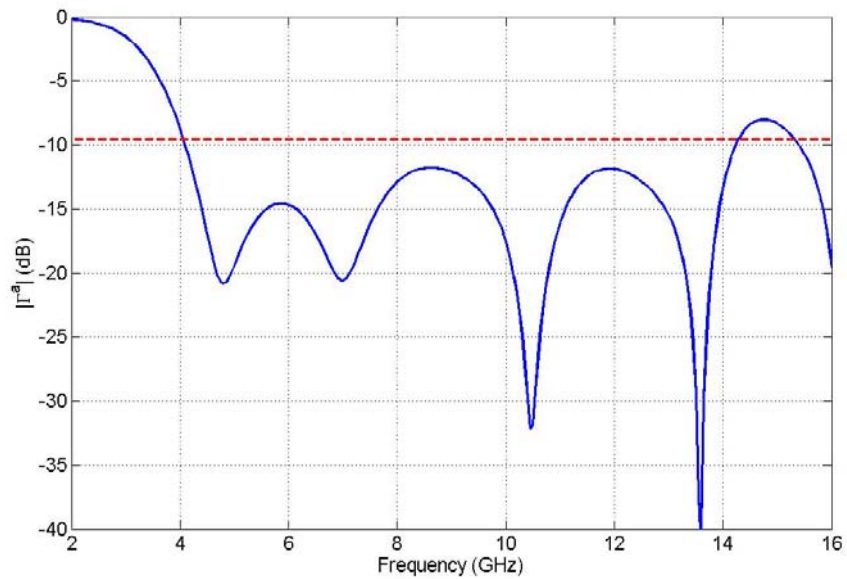


Figure 4.2: Simulated Active Reflection Coefficient for Infinite-by-1 Array of Vivaldi Antennas

The dashed line in Figure 4.2 represents an active reflection coefficient corresponding to $VSWR = 2$ (-9.54 dB). Therefore, it is apparent that the infinite array is in band over a frequency range from 4 GHz to 14 GHz, a bandwidth of 3.5:1. However, the bandwidth would be limited depending on the grating lobe frequency corresponding to the maximum scan angle. As was stated, for a 40 degree scan the grating lobe frequency for this array was 12.1 GHz. The E-plane scan performance was evaluated at angles of 20, 30 and 40 degrees from broadside. The VSWR computed at those scan angles are shown in Figure 4.3

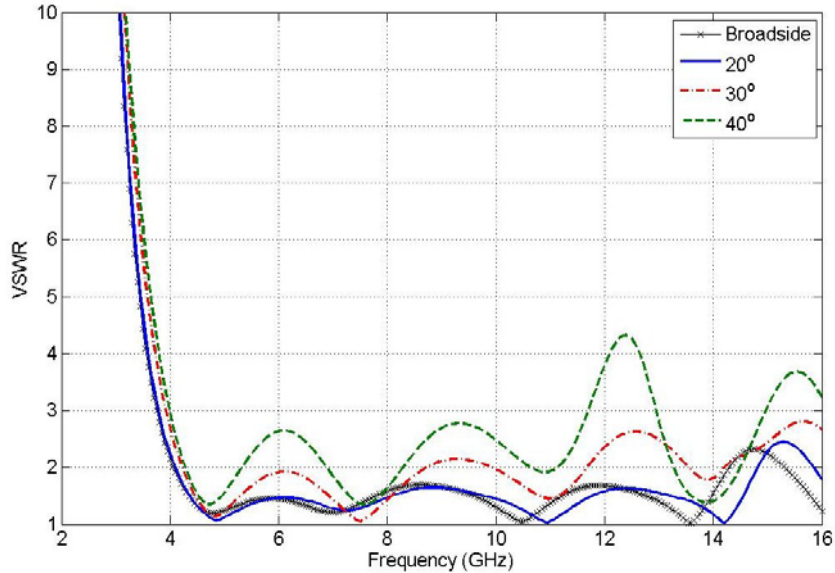
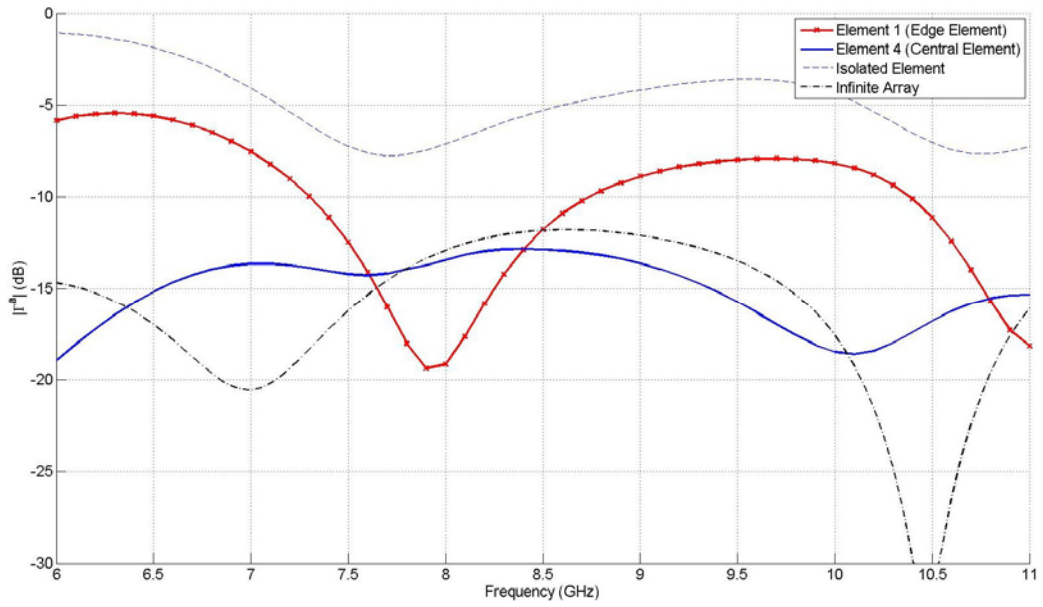


Figure 4.3: Simulated VSWR of Infinite-by-1 Array of Vivaldi Elements for Several Scan Angles

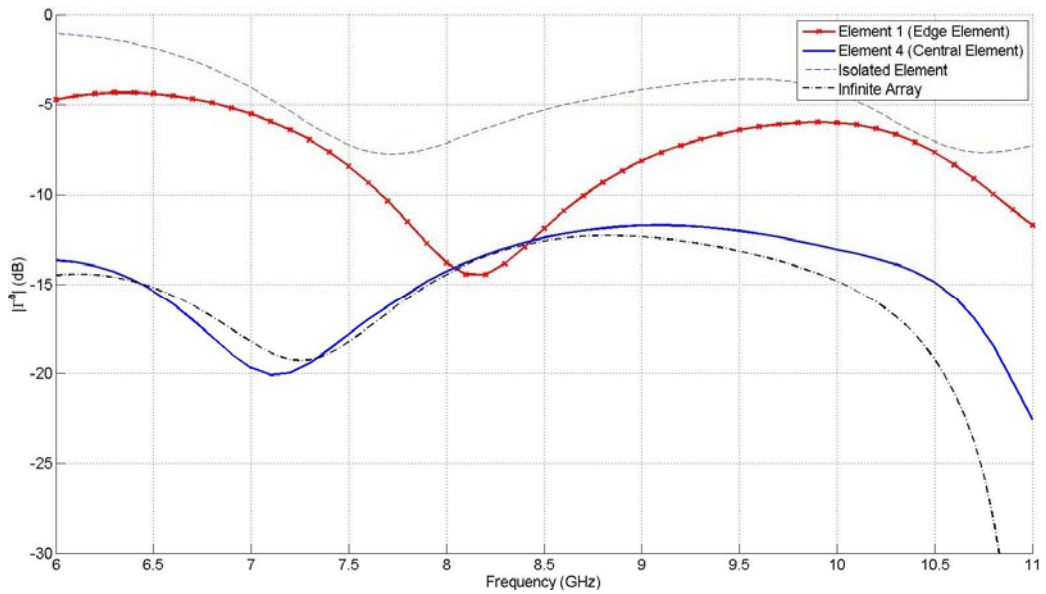
The array performance for a 20 degree scan is very similar to the broadside performance, in fact, the upper limit of the 2:1 VSWR bandwidth increases slightly. As the array is scanned further from broadside, its performance worsens. For a 30 degree scan the maximum VSWR in the band of interest (6-11 GHz) was 2.14, and for a 40 degree scan it was 2.87. The VSWR curve for a 40 degree scan has large peak at around 12.3 GHz, which most likely corresponds to the onset of a grating lobe. Because the array was designed to be a receive antenna, the relatively high VSWR of 2.87 was deemed acceptable.

While infinite array analysis is a good predictor for the performance of large arrays of Vivaldi antennas, it is less suitable for use in the design of small arrays. In small arrays, truncation effects may severely affect performance. As the size of an array is reduced, there are fewer elements; therefore, the effects of mutual coupling are weaker, especially towards the edge of the array. Since mutual coupling is utilized to

improve the bandwidth of the array elements, truncation may reduce bandwidth for elements near the array edge. Additionally, scattering and diffraction from the array edges may lead to resonances within the band of operation, which may cause further discrepancies between the results of infinite and finite array analyses. In order to determine the severity of truncation effects, the full 8x1 array was simulated in HFSS. A brute force method of meshing the entire structure and solving was employed. A port was assigned at each of the 8 elements in the array, and the 8-port scattering matrix was computed. The active reflection coefficients for the elements in the array were found as a post-processing step by applying the computed S-parameters in Equation 4-1. The structure was meshed assuming no phase shift between elements, which may cause some inaccuracy in the computations when a phase shift is introduced. This is because the adaptive mesher used in HFSS refines the mesh based on field intensity. When the array is scanned, the field intensity on the structure will change, and the broadside mesh may not accurately capture these changes. Figure 4.4 shows the active reflection coefficient for a central element and for an edge element in the finite array at scan angles of 0, 20, 30, and 40 degrees from broadside. The active reflection coefficients are compared with those of an infinite array comprised of the same elements, as well as with the return loss of an element isolated from the array environment. Note that the array is scanned towards the higher indexed elements. The array has the same dimensions as the one shown in Figure B.3 in Appendix B, but with elements electrically connected, and without the dummy elements present.

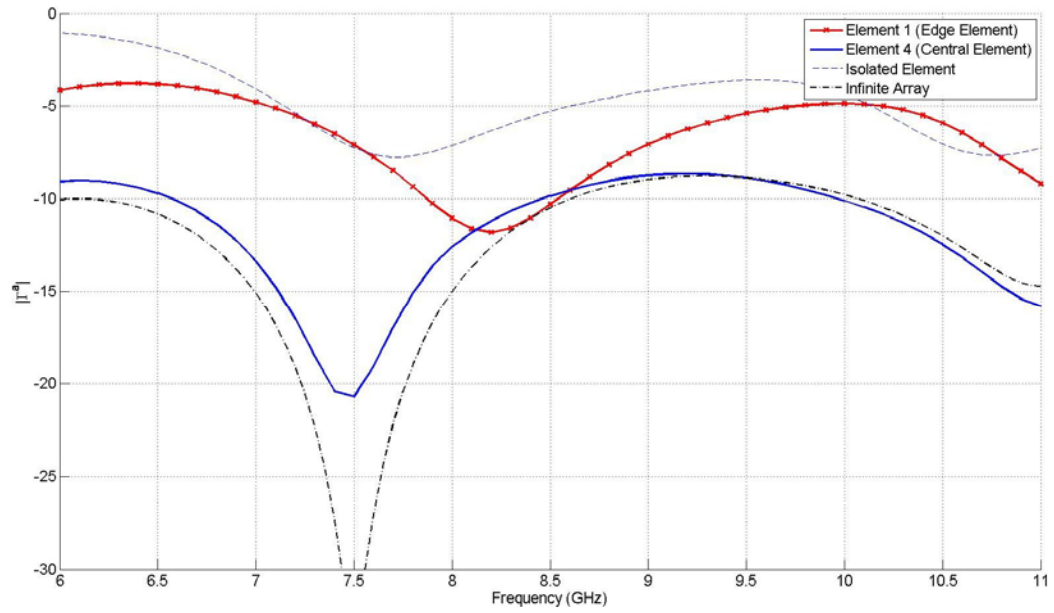


(a)

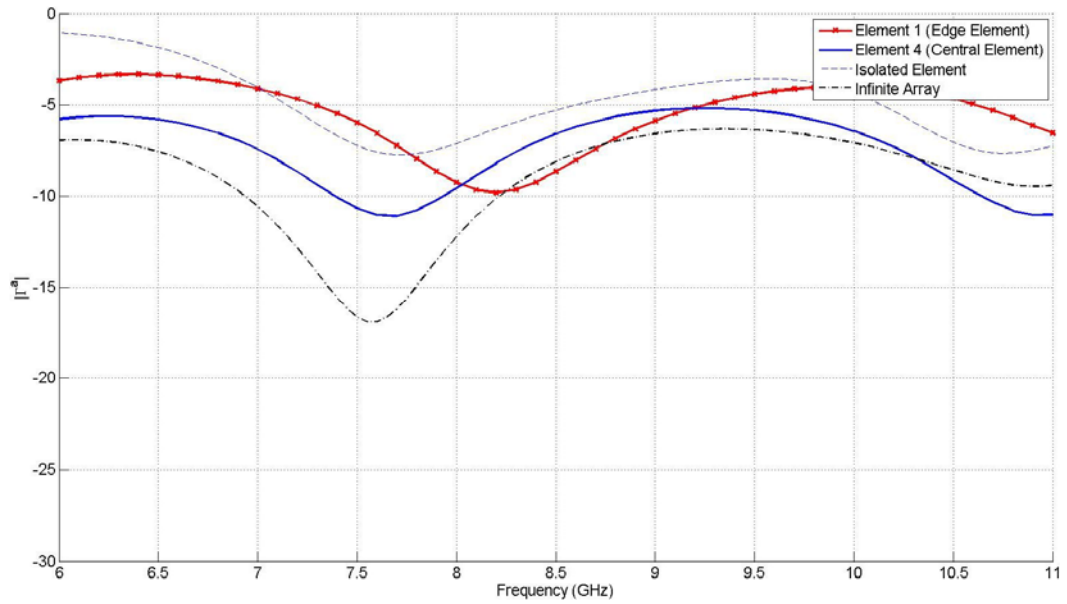


(b)

Figure 4.4: Simulated Active Reflection Coefficients of Elements in an 8x1 Array of Vivaldi Elements for scan angles of (a) 0°; (b) 20°; (c) 30°; (d) 40° (Continued next page)



(c)



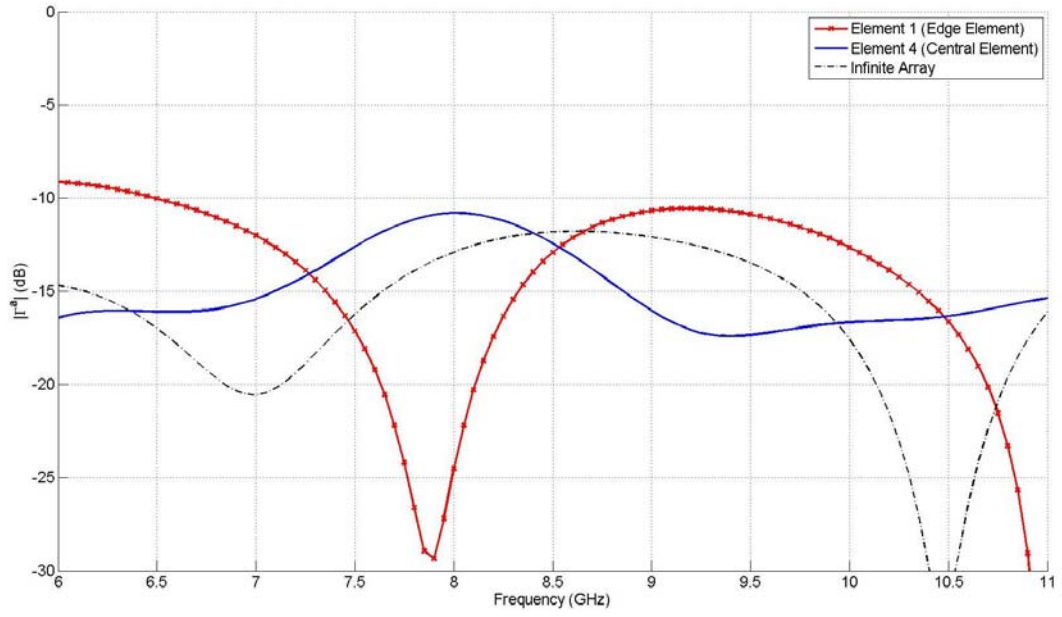
(d)

Figure 4.4, continued: Simulated Active Reflection Coefficients of Elements in an 8x1 Array of Vivaldi Elements for scan angles of (a) 0°; (b) 20°; (c) 30°; (d) 40°

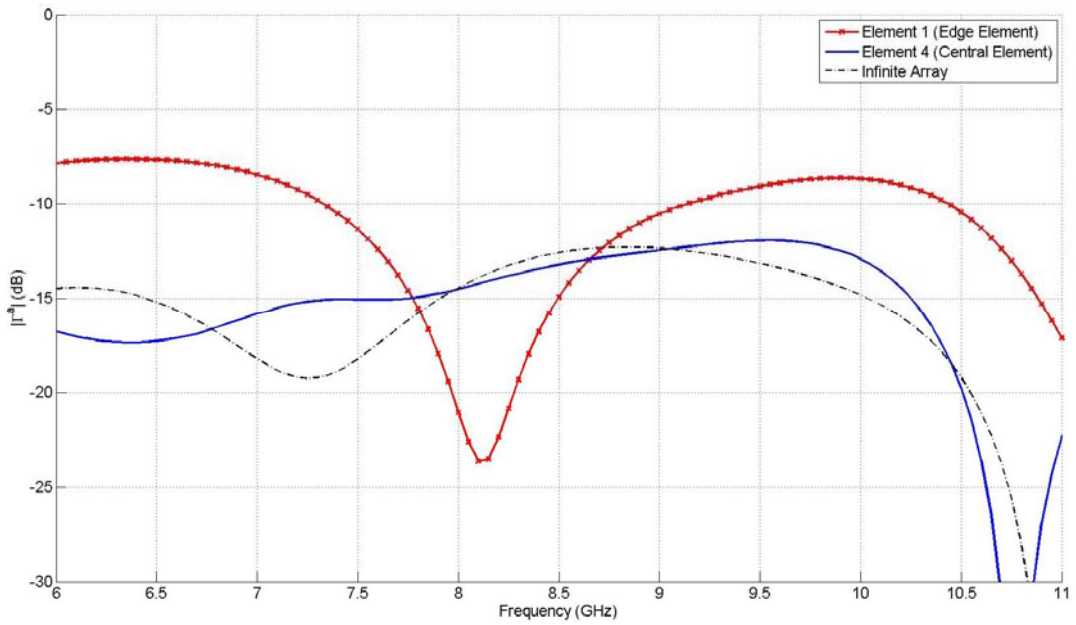
The results of the finite array simulations indicated that significant truncation effects occur in the 8x1 array. The results for the central element agree fairly well with the

infinite array results in terms of the peak magnitude; however, there are some discrepancies in the locations of peaks and nulls, especially at broadside. At a 40 degree scan, the peak active reflection coefficient is about 1 dB higher than that of the infinite array; this may be caused by truncation effects, or by the inaccuracies of using a broadside mesh. The performance of the edge element is significantly worse than that of the central element. The results for the edge element fall between those of the infinite array and those of the isolated element.

In order to improve the performance of the finite array, dummy elements were added to the array's edges. A dummy element is simply a non-excited element, which is terminated in a matched load. Dummy elements are utilized to provide a less abrupt termination of the array, and as a result, reduce truncation effects. Because dummy elements are purely passive, they do not need to be integrated with electronics, and do not significantly increase the complexity of an array's feed network. The 8x1 array was resimulated with a single dummy element included at both of the array's edges. Figure 4.5 shows the computed active reflection coefficients for elements within this array.

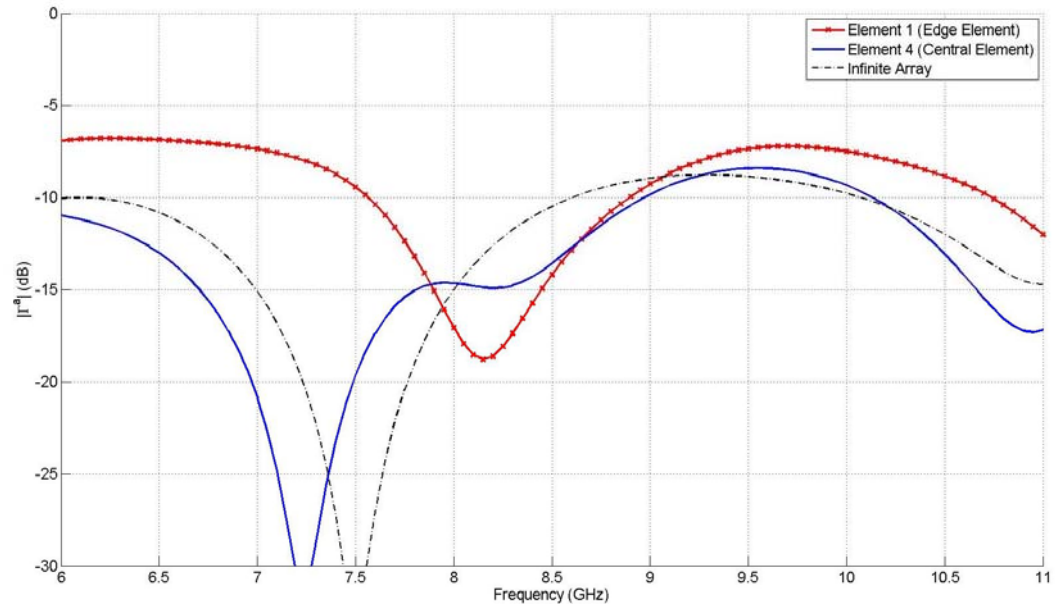


(a)

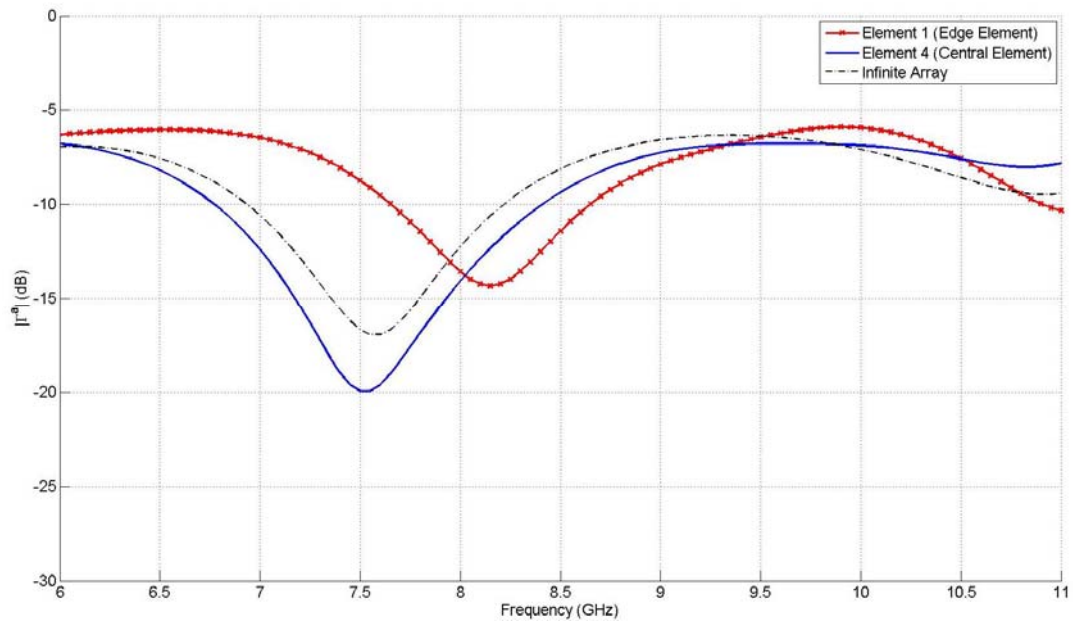


(b)

Figure 4.5: Simulated Active Reflection Coefficients of Elements in an 8x1 Array (Edge Elements Terminated) of Vivaldi Elements for scan angles of (a) 0° ; (b) 20° ; (c) 30° ; (d) 40°
(Continued next page)



(c)



(d)

Figure 4.5, continued: Simulated Active Reflection Coefficients of Elements in an 8x1 Array (Edge Elements Terminated) of Vivaldi Elements for scan angles of (a) 0°; (b) 20°; (c) 30°; (d) 40°

The plots above indicate that adding dummy elements improves the performance of the edge element. At broadside, the edge element exhibits an active reflection coefficient better than 10 dB across most of the band. The array was also simulated with two dummy elements on either edge; however, it was determined that the additional elements had little impact on the array's performance.

4.1.3 Effects of Modularity

Ultimately the Vivaldi elements in the array were to be fabricated as modular packages. In the simulations described above, all the array elements were electrically connected. However, it has been shown [19] that separating elements in a TSA array leads to severe impedance anomalies, which may significantly reduce bandwidth. The 8x1 array described in the previous section was resimulated with electrically separated elements. A gap one substrate thickness (20 mil) in width was introduced between each element, while all other array parameters were left the same. Figure 4.6 shows the active VSWR for a central element in the array with element separation compared to the VSWR of the same element in the array with connected elements.

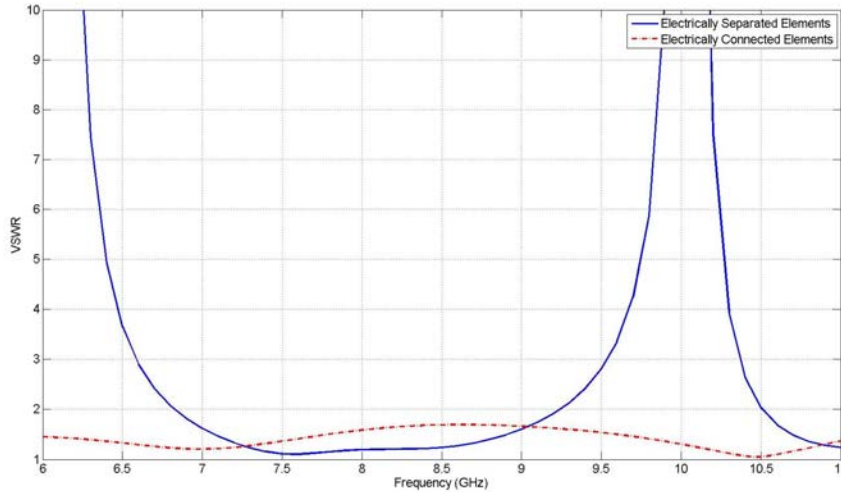


Figure 4.6: Simulated VSWR for Central Element in 8x1 Array of Vivaldi Antennas with and without Electrical Separation Between Elements

It is apparent that impedance anomalies occur around 6 GHz and 10 GHz, limiting the 2:1 VSWR bandwidth for broadside scan to 2 GHz. Such anomalies were studied in [20], and were attributed to slotline resonances excited in the interelement gaps. These resonances were shown to occur at frequencies when the gaps were odd multiples of $\lambda/4$ in length. In order to make use of modular Vivaldi elements in phased arrays, a method must be developed to suppress these resonances. For this project, copper strips were soldered across the gaps to suppress slot resonances. However, such a method of connecting elements is not amenable with the low cost techniques discussed in this thesis. In the absence of a low cost solution for suppressing slot resonances, the gap-induced anomalies described here remain a major obstacle preventing the widespread use of modular TSA elements.

4.2 Array System Components and Assembly

4.2.1 Active Element Layout

The layout of the array elements was similar to the layout of the individual Vivaldi antenna described in Chapter 3, but on a smaller scale. As was explained in the previous section, the active element packages had to fit within a spacing of 16.36 mm in order to prevent the onset of grating lobes. Additionally, since there was a 20 mil gap between elements, the maximum width of the antenna packages was limited to 15.85 mm. In order to minimize coupling, the feed lines were separated by two substrate thicknesses (40 mil). Using these guidelines, an element with a width of 14.49 mm was designed. The fabricated Vivaldi element packages are shown in Figure 4.7. Dimensioned drawings of this element are included in Appendix B.

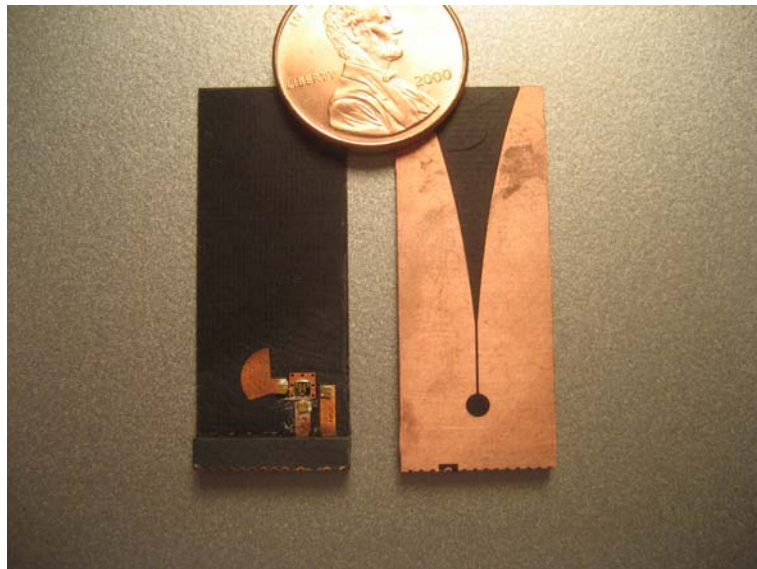


Figure 4.7: Active Vivaldi Element Packages

4.2.2 Array Feeding and Phase Control Networks

In order to measure the array, power division and phase control networks were required. A practical version of the array designed in this thesis would have power division networks printed onto the array motherboard. However, for the prototype array, separate connectorized power dividers were used to feed both the IF and LO signals. Each element was fed with CPW LO and IF feed lines, which were printed onto the array motherboard (see Figure 4.11 on page 64). The power division networks were connected to the motherboard using short lengths of coaxial cables. A primary concern was whether the LO power delivered to each element would be sufficient to drive the mixer diodes. In order to ensure that enough power was delivered, an amplifier was placed directly at the input of the LO power divider.

In order to electronically scan the main beam of the array, a phase control network was required. In a phased array, the main beam is steered by introducing a progressive phase shift between elements. The progressive phase required to scan the main beam to an angle θ_o is given as

$$\Delta\phi = -kd_x \sin \theta_o \quad (4-3)$$

where k is the free space wavenumber and d_x is the spacing between elements. For this project, commercial, off the shelf, phase shifters were used to produce the required inter-element phasing. Considerations for choosing phase shifters included cost, availability, simplicity of operation, size, frequency of operation, insertion loss, and total phase shift. Since the antenna elements were integrated with mixers, each active element had both IF and LO ports. If the mixers are modeled as signal multipliers, then the RF signal (after high-pass filtering to remove the image frequency) is given as

$$\begin{aligned}
V_{RF} &= KV_1 \cos(2\pi f_{LO}t + \Delta\phi_{LO}) \cdot V_2 \cos(2\pi f_{IF}t + \Delta\phi_{IF}) \\
&= \frac{KV_1V_2}{2} \cos(2\pi(f_{LO} + f_{IF})t + \Delta\phi_{LO} + \Delta\phi_{IF})
\end{aligned} \tag{4-4}$$

where $\Delta\phi_{LO}$ and $\Delta\phi_{IF}$ are phase shifts of the LO and IF signals respectively, and K is a conversion constant. From 4-4 it can be concluded that a phase shift introduced at either the LO or IF frequencies will produce the same phase shift at RF. Therefore, a choice existed of whether to implement the phase shifters at IF or at LO. For this project, the LO signal had to have a large enough power to turn on the diode mixers, therefore, losses in the LO feed network needed to be avoided. It was decided to incorporate the phase shifters into the IF feed network, since losses at IF were more tolerable. Similarly, there was some freedom about what frequencies to use for the IF and LO signals. To further prevent losses in the LO feed network, it was desirable to use a higher IF frequency, such that the LO frequency could be reduced.

A component search yielded several different models of phase shifters, including mechanical, digital, and analog implementations. The different options of phase shifters are summarized below:

- Mechanical phase shifters are operated by manually adjusting a length of transmission line to shift phase, and thus require no external control networks. They are also broadband, and their total achievable phase shift increases as a function of frequency. However, commercially available mechanical phase shifters were found to be relatively expensive, large, and fairly cumbersome to implement.

- Digital phase shifters use switched transmission lines to achieve discrete phase shifts. Off-the-shelf digital phase shifters were identified to have the same cost and size problems as the mechanical phase shifters. Additionally, some means of inputting digital logic would have been required, thereby adding to the complexity of use.
- Analog phase shifters use continuously variable input signals to control phase. Analog phase shifters may utilize ferrites or variable reactive elements such as varactor diodes. Available analog phase shifters were found to have higher insertion loss, and to be relatively narrowband. Also, an external voltage control network was required to control multiple phase shifters. However, a commercially available analog phase shifter that was relatively inexpensive, small, and worked at desirable frequencies was located, and thus was deemed to be the best choice for this project.

The JSPHS-1000 model phase shifter from Mini-Circuits was chosen. The model operated over the frequency band of 700 MHz to 1000 MHz, which corresponded to desirable IF frequencies. Other attractive features included the comparatively low cost of the components (\$26 per part), the fact that the devices were surface mountable, and the fact the width of each phase shifter fit within the interelement spacing of the array. A datasheet for the JSPHS-1000 is included in Appendix C. One difficulty was that each phase shifter was only capable of 180° phase shift, while 360° phase shift was required to produce the necessary scan. For that reason, two cascaded phase shifters were used to produce a single phase shifter.

A CPW IF power division/phase control board was assembled on a 31 mil thick FR-4 substrate. An 8-way power divider was created using seven 2-way surface mount power dividers. The surface mount power dividers were inexpensive (\$0.99/part), and operated from 600 MHz to 1100 MHz. Two cascaded phase shifters were used on seven of the eight branches of the 8-way power divider. The phase at the first element in the array was used as the reference; therefore, phase shifters were not required in the branch feeding that element. The two phase shifters on each branch were controlled with a common DC voltage, which was fed on the underside of the board. Figure 4.8 is an image of the completed IF control board.

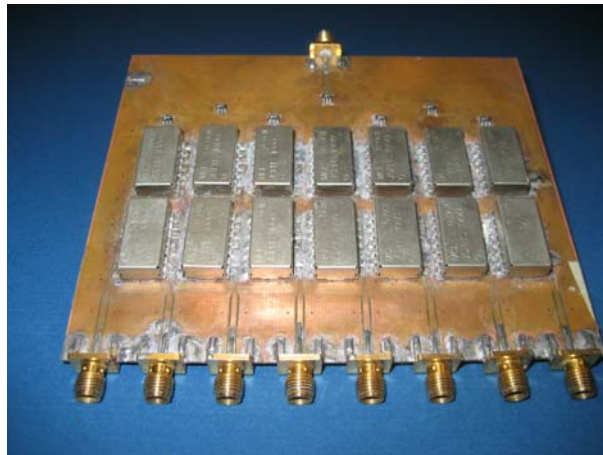


Figure 4.8: IF Control Board

Different DC control voltages were required at each branch of the IF control board; therefore, it was necessary to design a DC control network. Measurements indicated that a full 360° phase shift could be achieved for a DC voltage range from 1 to 14 volts, at a frequency of 850 MHz. A simple voltage control network was designed, which

used seven non-inverting op-amp voltage amplifiers. The schematic for a non-inverting voltage amplifier is shown in Figure 4.9.

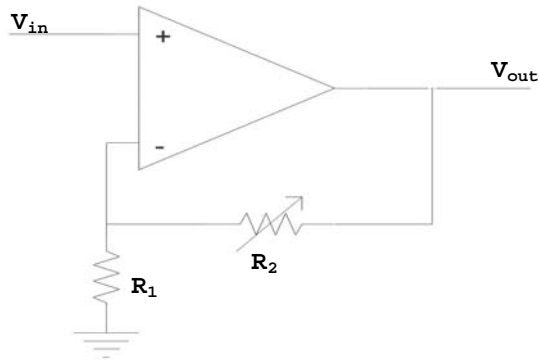


Figure 4.9: Non-inverting Voltage Amplifier

The output voltage for this circuit is given as

$$V_{out} = V_{in} \left(1 + \frac{R_2}{R_1} \right) \quad (4-5)$$

An input voltage of 1 volt and an R_1 value of 1 k Ω were used, so in order to produce a voltage between 1 volt and 14 volts, R_2 needed to vary between 0 Ω and 13 k Ω . Potentiometers were used to produce the variable resistance for R_2 . Figure 4.10 shows the control network, which was constructed on a powered breadboard.

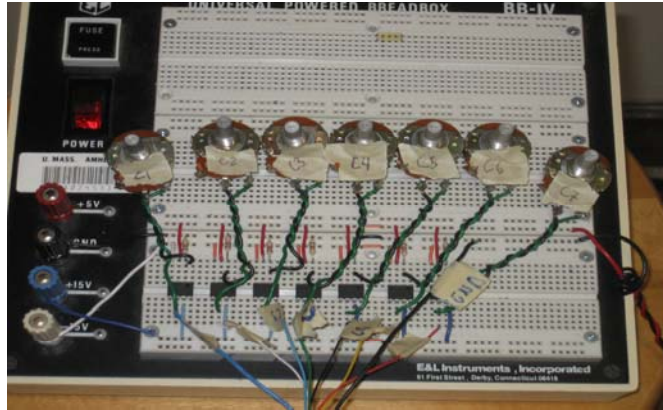
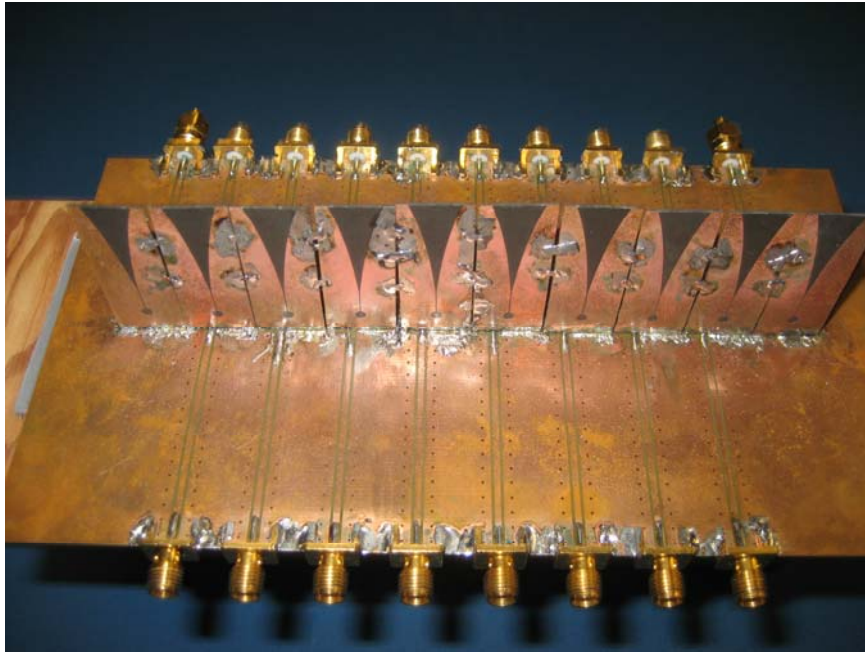


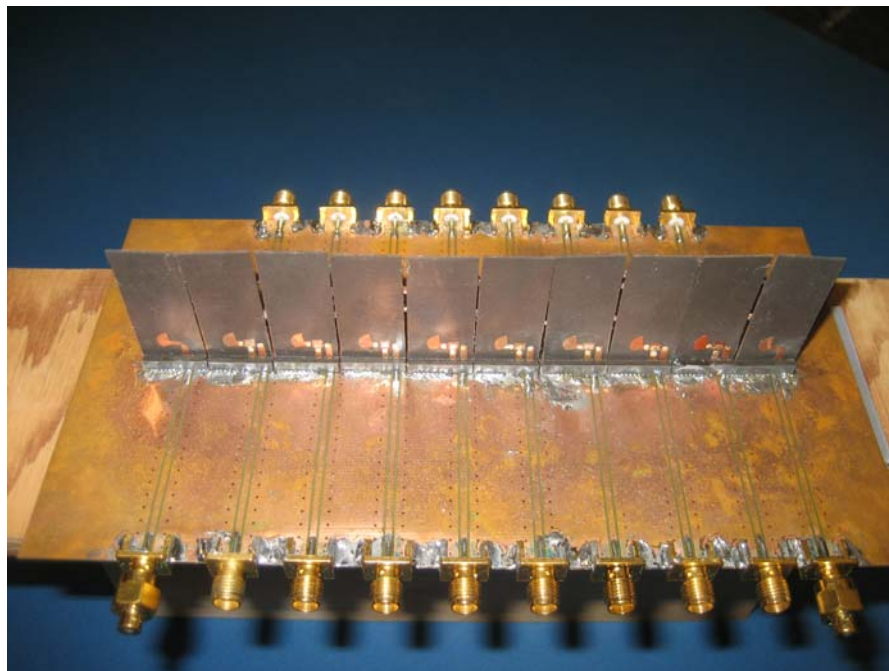
Figure 4.10: DC Control Network

4.2.3 Array Assembly

The assembly of the array of Vivaldi elements was significantly more challenging than the mounting of a single element. In the previous case, the entire motherboard was heated on a conveyer belt-type hotplate to facilitate solder reflow through the castellations. If the same method were used to construct the array, all of the elements would have had to have been mounted simultaneously, otherwise some elements would have been exposed to the reflow cycle multiple times. Some sort of rig could have been used to hold all of the elements in place; however, it was found that the adhesive used to attach the support package to the antenna board failed when exposed to high temperatures. For that reason, the packages could not be mounted on a hotplate. Instead, a soldering iron with a fine tip was used to reflow solder paste under the castellations. Once the elements were soldered in place, the slots between the elements were shorted by soldering copper strips across the gap. Figure 4.11 shows the completed array. Note that the elements in the array are somewhat misaligned with respect to one another due to the method of construction. A dimensioned drawing of the array is included in Appendix B.



(a)



(b)

Figure 4.11: Assembled Vivaldi Array (a) Front View; (b) Back View

4.3 Array Measurements

The performance of the active array was evaluated by measuring its radiation patterns for several frequencies and scan angles. It would have been very difficult to mount the array and its power dividing networks onto the rotating positioner used in the far-field measurement scheme; instead, the array patterns were measured using a planar near-field scan. A planar scan measures the near-field radiation from the AUT on an imaginary planar surface. A Fourier transform of the measured near-field is then performed to compute the far-field patterns. Through the use of holographic projection, it is also possible to calculate an aperture field at an arbitrary distance from the antenna. Near-field planar scans are well-suited for measuring the patterns of high gain antennas [21]. A drawback to using planar measurements is that the maximum far-field angle that may be computed is limited. Since the array was fairly directive (~ 16 dBi), a planar scan was considered to be an acceptable method. Because of the frequency conversion at the array, a similar method of measurement to the one shown in Figure 3.9 was used. Figure 4.12 shows the setup used to measure the array patterns.

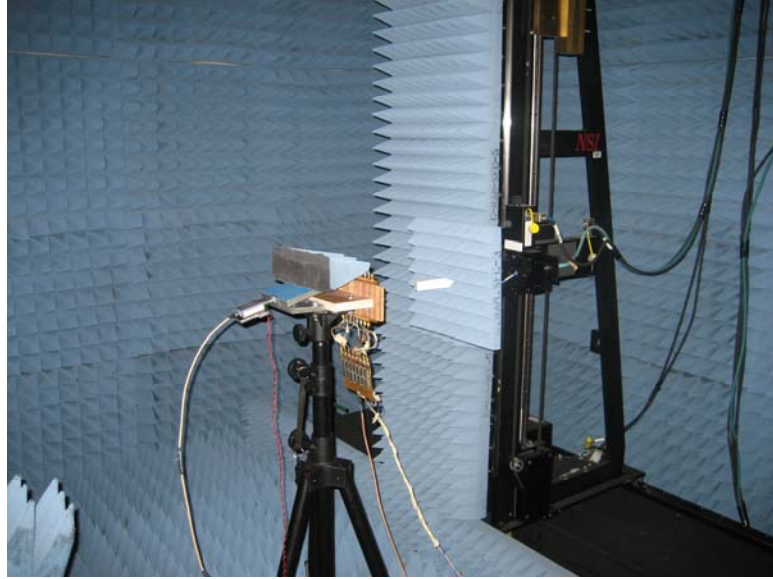


Figure 4.12: Near-field Measurement Setup

When the array was measured, the effects of amplitude and phase errors needed to be considered. In large, periodic arrays, the general effect of random excitation errors is to increase the array's average sidelobe level [18]. In practical phased arrays, such excitation errors are largely caused by limited manufacturing tolerances, and are usually assumed to be small and uncorrelated (zero mean). The primary source of excitation errors in the 8x1 prototype array was from the coaxial cables used to connect the LO and IF power dividers to the array motherboard. The lengths of the cables were not controlled; therefore, an arbitrary inter-element phase error was introduced. Additionally, the cables were chosen to be flexible, and as a result, suffered from higher attenuation and lesser phase stability. Other sources of phase errors included limited manufacturing tolerances, the misalignment of the array elements, and the integrated mixer ICs. In a practical active phased array, the phase errors caused by the integrated electronic components would be of great concern. The phase error between the

integrated mixer ICs was measured to be approximately $\pm 20^\circ$ at 11 GHz and maximum LO drive. Amplitude errors were largely caused by differing mixer conversion losses at each of the active elements. The prototype array was not large enough such that the excitation errors could be assumed to be zero mean; therefore, the errors had the effect of scanning the array's main beam from broadside, as well as raising the sidelobe level, as shown in the measured pattern in Figure 4.13.

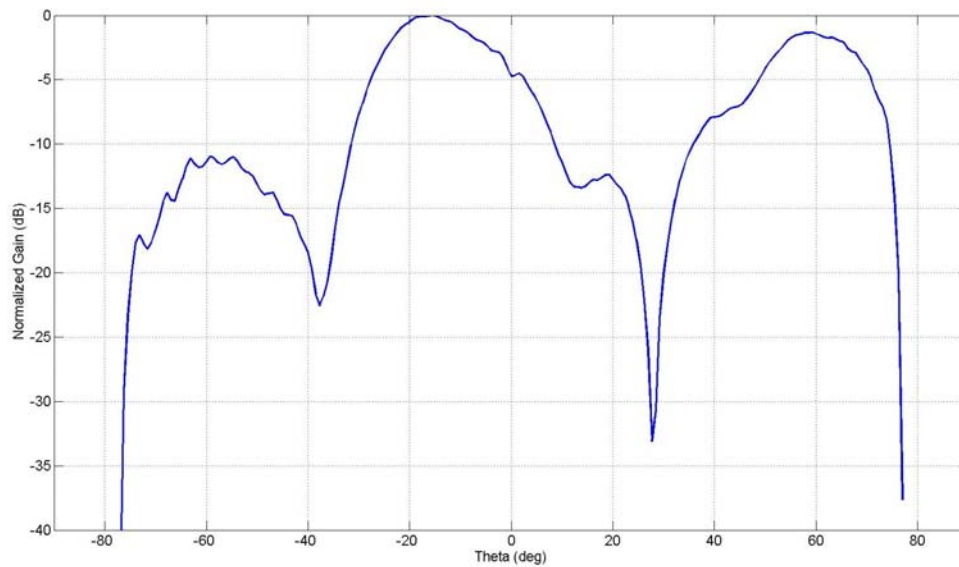


Figure 4.13: Measured Broadside Radiation Pattern for Vivaldi Array with Excitation Errors

In order to determine the array's excitation errors, the measurement loop $|S_{21}|$ was obtained when each element was individually excited. The measured inter-element amplitude errors, δ , and phase errors, Φ , at an RF frequency of 8 GHz are shown in Table 4.1.

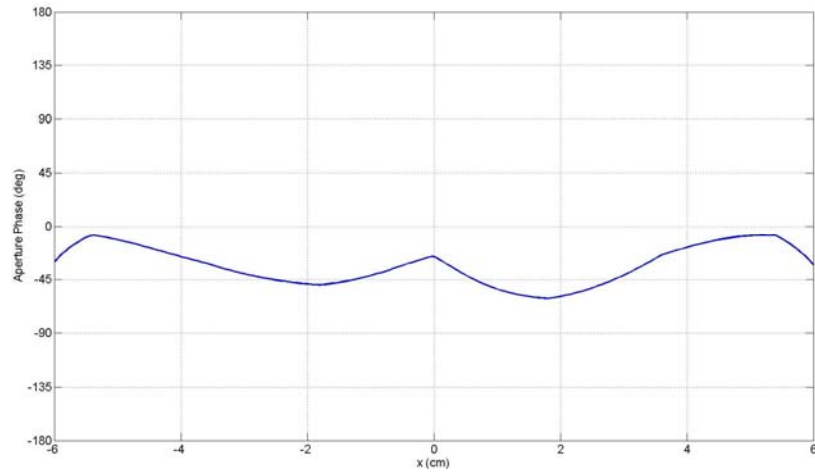
Table 4.1: Excitation Errors in 8x1 Array

Element #	Δ	Φ
1	-4.3 dB	0°
2	-0.5 dB	-111°
3	-2.0 dB	-24°
4	0 dB	-128°
5	-0.2 dB	-137°
6	-1.1 dB	176°
7	-0.9 dB	-122°
8	-1.4 dB	138°

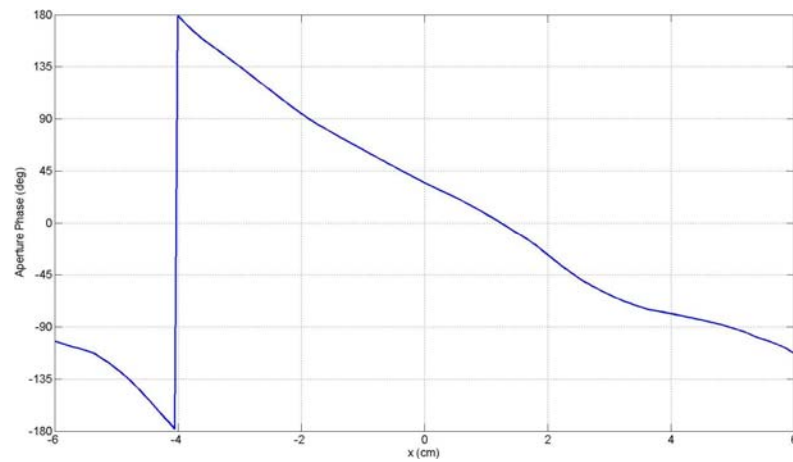
From the results in Table 4.1, the RMS amplitude error and RMS phase error were calculated as 1.1 dB and 116° respectively. The amplitude errors in the array were determined to have much less of an effect on the array's pattern than the phase errors. Additionally, amplitude correction would have been much more difficult to implement; therefore, only phase errors were corrected for.

The array's E-plane pattern was measured at frequencies of 6 GHz, 8 GHz, and 10 GHz, and for scan angles of 0°, 20°, and 40°. At each frequency the phase errors were calculated, and then corrected for using the phase control network described in section 4.2.2. As was discussed, the phase shifters were controlled using potentiometers in a DC voltage-divider network. The phase shift for each of the branches of the phase control network was measured using a network analyzer, and the potentiometer dials at each branch were adjusted until the prescribed phase shift was achieved. The array was then measured with the applied phase shift/correction. Amplitude errors and some residual phase error existed after the correction was applied. This residual error was

determined by measuring the aperture field using holographic back-projection. Plots of the measured aperture phase are shown in Figure 4.14.



(a)

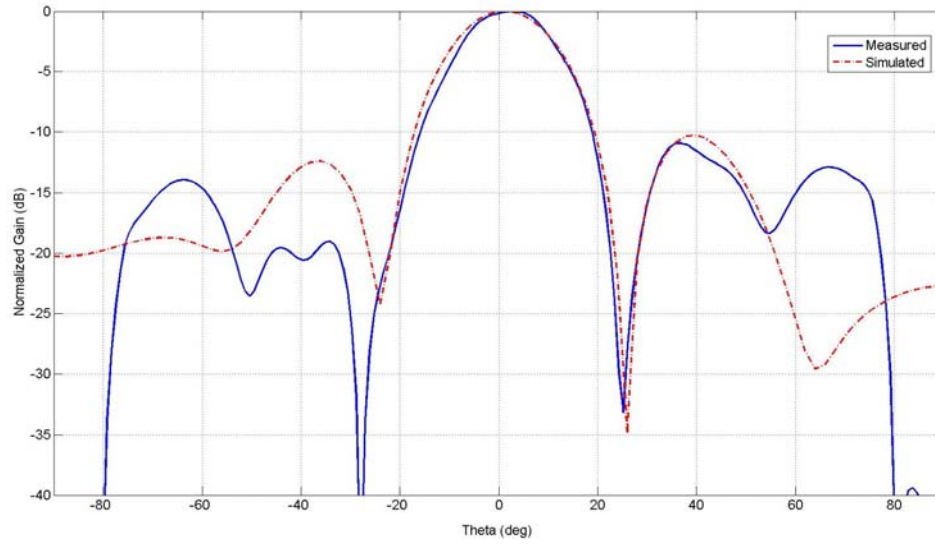


(b)

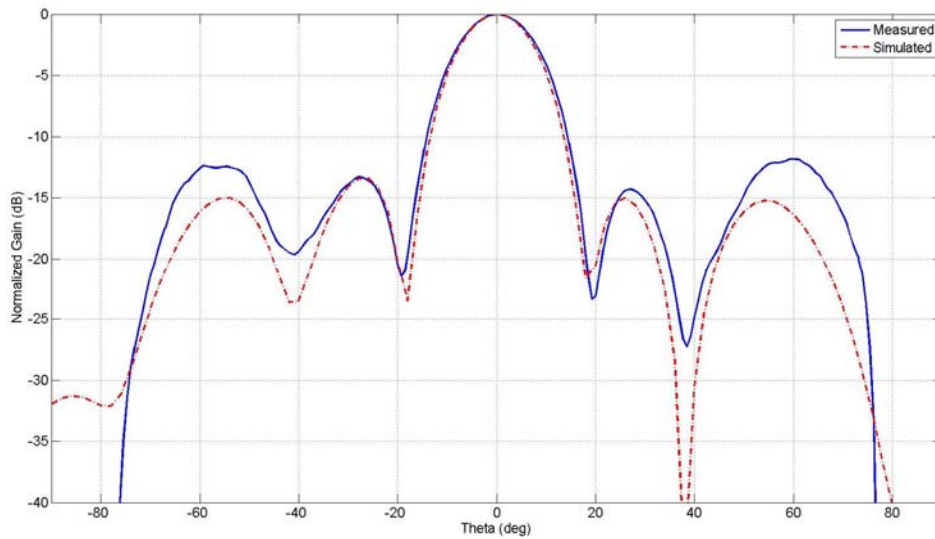
Figure 4.14: Measured Phase at Array Aperture for Scan Angles of (a) 0° , (b) 20°

The amplitude and phase at each element were extracted from the measured aperture field and applied to the HFSS simulations. The measured far-field radiation patterns of

the array are compared with the corrected simulation patterns in Figure 4.15, Figure 4.16, and Figure 4.17. The simulated array was backed with a finite ground plane.

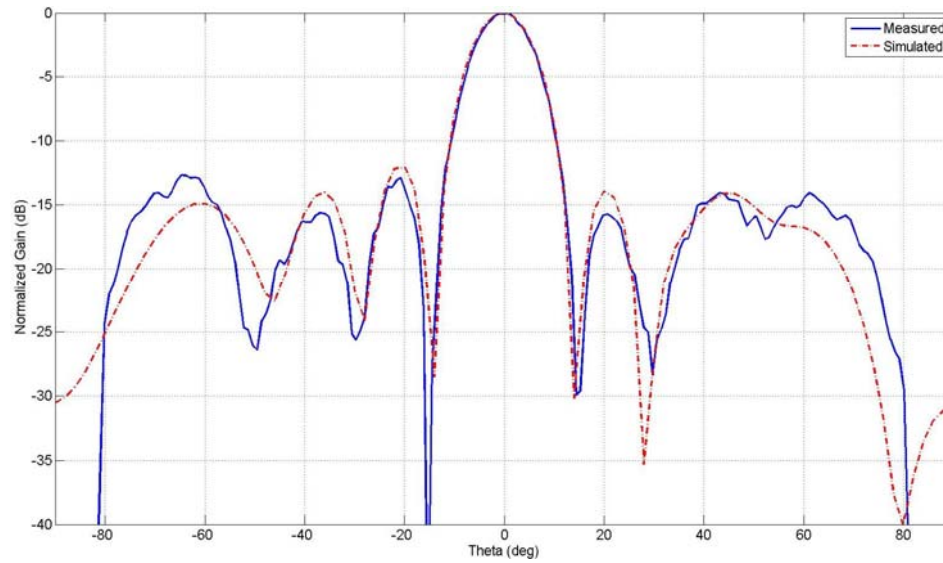


(a)



(b)

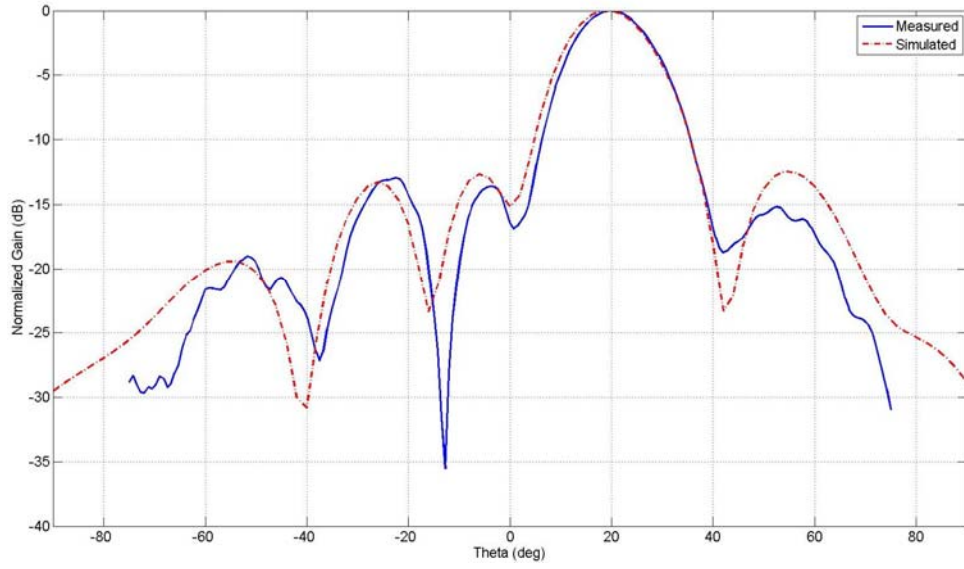
Figure 4.15: Measured vs. Simulated E-Plane Radiation Patterns for 8x1 Array of Vivaldi Elements (0° scan) at: (a) 6 GHz, (b) 8 GHz, (c) 10 GHz (**Continued next page**)



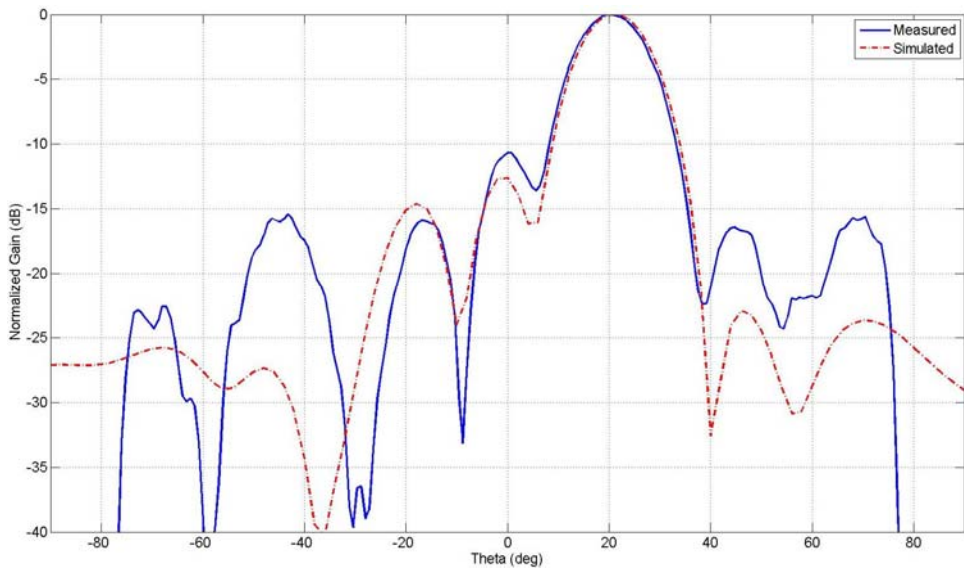
(c)

Figure 4.15, continued: Measured vs. Simulated E-Plane Radiation Patterns for 8x1 Array of Vivaldi Elements (0° scan) at: (a) 6 GHz, (b) 8 GHz, (c) 10 GHz

At broadside, the main beams of the measured array exhibits excellent agreement with the simulations. The measurements show higher sidelobes than were predicted at wide far-field angles. It is possible that these high sidelobes are the result of excitation errors, and that the corrections applied to the HFSS simulations were not fully accurate. However, the sidelobes decrease somewhat as the maximum far-field angle is increased. This seems to indicate that the high sidelobes may be partially due to truncation effects in the Fourier transform algorithm utilized by the near-field range software.

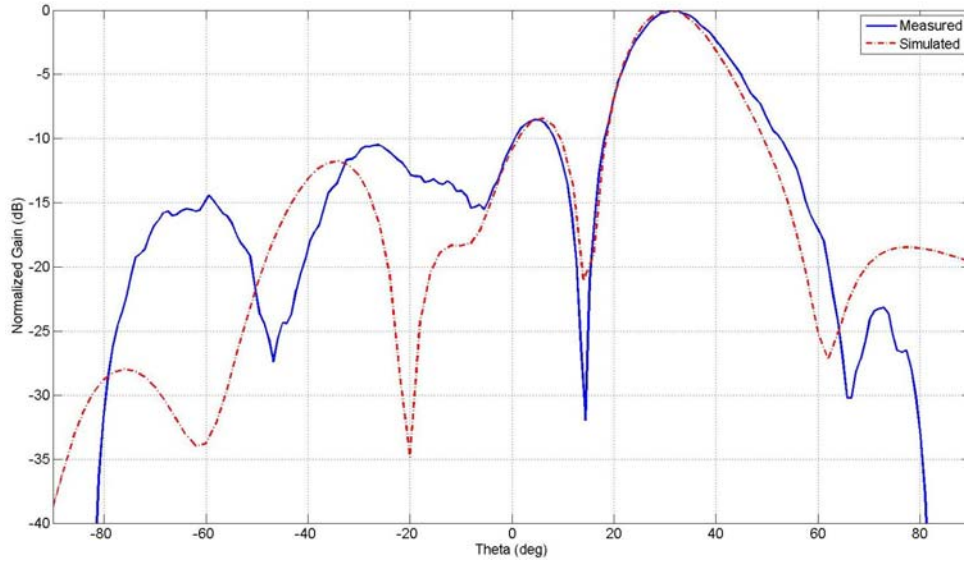


(a)

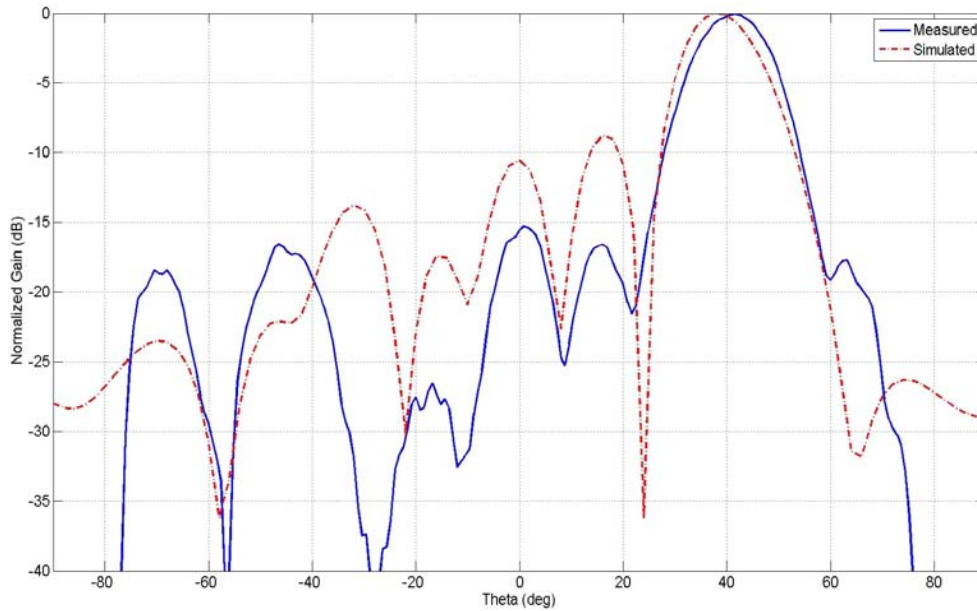


(b)

Figure 4.16: Measured vs. Simulated E-Plane Radiation Patterns for 8x1 Array of Vivaldi Elements (20° scan) at: (a) 8 GHz, (c) 10 GHz



(a)



(b)

Figure 4.17: Measured vs. Simulated E-Plane Radiation Patterns for 8x1 Array of Vivaldi Elements (40° scan) at: (a) 8 GHz, (c) 10 GHz

At 20 degree scan, there is increased disagreement in the sidelobe levels of the measured and simulated patterns. Additionally, at 8 GHz there is also some discrepancy in the main beam. The 3 dB beamwidth for the measured pattern is about

1.5 degrees narrower than the simulated pattern. These disagreements probably result from errors in the correction that was applied to the simulations. For a 40 degree scan increased discrepancies exist between the measured and simulated values. At 10 GHz, the simulated and measured main beams are located at somewhat different angles, and there is significant disagreement between the sidelobe levels of the two patterns. At 8 GHz, the main beam of the measured pattern is broader than that of the simulated pattern. Since the main beam is on the outer edge of the planar scan's field of view, this discrepancy may be a truncation effect.

4.4 Summary

In general, the prototype active array designed in this thesis provided a successful demonstration of concept. The measured performance of the array agreed well with simulation results when excitation errors were factored in. Without correction, the array's performance was dominated by excitation errors. In the future, such errors could be largely avoided by using cables with controlled lengths and employing a better method of construction for the array. Amplitude errors could be reduced by ensuring that each mixer is driven with roughly the same LO power, thereby maintaining more uniform conversion losses. Finally, a more precise phase control network using digital phase shifters could also help reduce errors, and would make it much easier to apply phase shifts/corrections.

CHAPTER 5

CONCLUSION AND FUTURE WORK

A method for manufacturing low-cost phased arrays of Tapered Slot Antenna elements was explored in this thesis. The novel aspect of this research was the development of low-cost active Vivaldi elements, which were manufactured using standard PCB fabrication techniques, and were capable of being orthogonally mounted onto a phased array motherboard. The following is a summary of the important accomplishments and results achieved in this thesis:

A simple, low-cost method of orthogonally mounting end-fire antennas was achieved using castellated vias. A castellated CPW-to-microstrip transition with better than 15 dB return loss from 0 to 12 GHz was designed. Several prototypes were constructed, and the electrical performance of the castellated interconnection was validated. In general, the use of castellated vias proved to be an effective means of surface mounting endfire antennas. If proper solder reflow parameters are used, the limiting factor in the structural integrity of a castellated interconnection would be the strength of the copper plating in the castellated vias and of the adhesive connecting the support package. A foam support could be used to reinforce the castellated interconnections.

Passive and active castellated Vivaldi element packages were designed, fabricated, and measured. An isolated Vivaldi element with a 2:1 VSWR bandwidth from 5 to 12.5 GHz was designed and implemented in passive and active configurations.

Both antennas were orthogonally mounted onto a 12 cm x 10 cm CPW motherboard. The active antenna was integrated with the HMC130 mixer IC, which had a bandwidth from 6 to 11 GHz. Both the passive and active configurations were measured, and the results obtained agreed well with simulated values. In general, the active antenna exhibited improvements in performance over the passive configuration. Specifically, the E-plane radiation patterns of the active Vivaldi showed better agreement with simulations than did the passive element. Furthermore, the active element also exhibited improved relative efficiency, and lower cross-polarization levels.

An 8x1 phased array of active, castellated Vivaldi elements was designed, fabricated, and measured. An element, which exhibited 3.5:1 bandwidth in an infinite linear array, was developed. Additionally, it exhibited a scan volume of 30 degrees, and performed adequately to 40 degrees. Finite array analyses indicated that while the performance of central elements in an 8x1 array comparable to those in an infinite array, truncation effects had a significant impact on the performance of edge elements. These truncation effects were mitigated somewhat through the use of dummy elements at the array edges. An 8 element array of active Vivaldi elements was fabricated and assembled. Each element was integrated with an HMC130 mixer chip and mounted onto a CPW motherboard. In order to scan the array and correct for phase errors, a phase control network was constructed with voltage-controlled analog phase shifters. The array patterns were measured for several frequencies and scan angles. The measured patterns exhibited good agreement with simulated patterns, and most discrepancies between the measured and simulated results could be attributed to excitation errors.

In the future, the work done in this thesis could be expanded upon in a variety of ways. For simplicity, the elements in this thesis were integrated with only frequency conversion ICs. In a practical array, it would be ideal to integrate a full RF front end with the antennas. It would be desirable include oscillators at each element so that only low frequency baseband and synchronization signals would need to be transferred from the motherboard to the element packages. Planar and dual-pol arrays of castellated elements would be more challenging to feed than the linear array presented in this thesis. A multilayered motherboard could be used to accommodate the multiple feed networks that would be required. A major source of cost in large phased arrays is the phase control network. For a low cost array, row-column beam steering method could be used. In such a scheme only one phase shifter is used at each row and each column of the array. In one direction, a shift is applied to the IF signal, and in the other direction the shift is applied to the LO (or synchronization) signal. The row-column steering method results in a dramatic decrease in the number of phase shifters required. However, the row-column technique would not be practical if there is significant phase error between the ICs on each element, such as the $\pm 20^\circ$ error measured for the mixers used in this project.

In general, the reduction of cost is an important design goal in all phased array systems. Given the excellent performance of TSA arrays, the idea of producing low-cost, active TSA elements is very attractive. If a low cost method for suppressing slot resonances in arrays of modular elements can be achieved, then the elements designed in this thesis may be a viable option for use in such an array.

APPENDIX A

ISOLATED VIVALDI ANTENNA WITH CORRUGATED EDGES

There are a number of applications which may make use of an isolated Vivaldi radiator. A Vivaldi element intended to operate as an isolated radiator was designed for this thesis and described in Chapter 3. The radiation patterns for this antenna varied significantly as a function of frequency, and exhibited fairly high sidelobes. One method used to improve the radiation patterns of TSA is to etch corrugated slots along the edges of the antenna's metallization as shown in Figure A.1 [14].

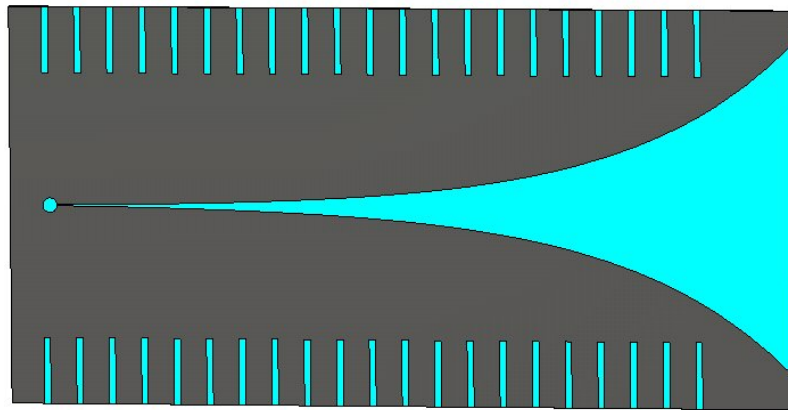
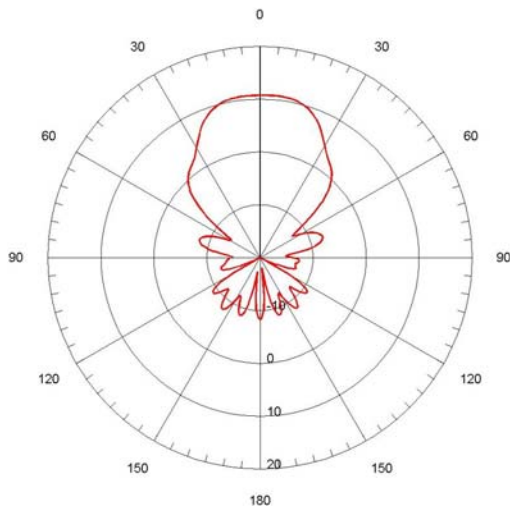
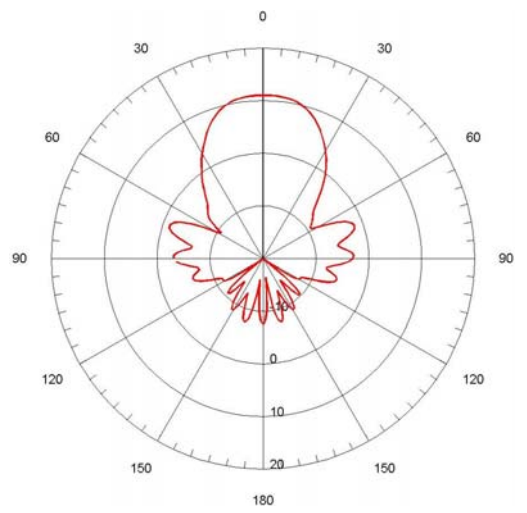


Figure A.1: Vivaldi Antenna with Corrugated Edges

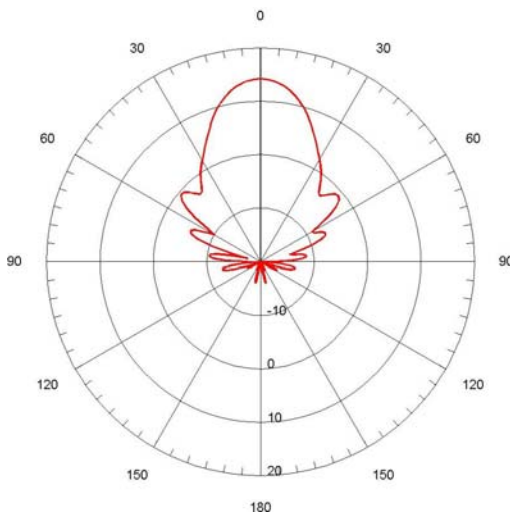
The antenna described in Chapter 3 was resimulated with slots that were 2 mm in width, 5 mm in depth, and spaced every 10 mm. Simulated gain patterns are shown in Figure A.2 and Figure A.3.



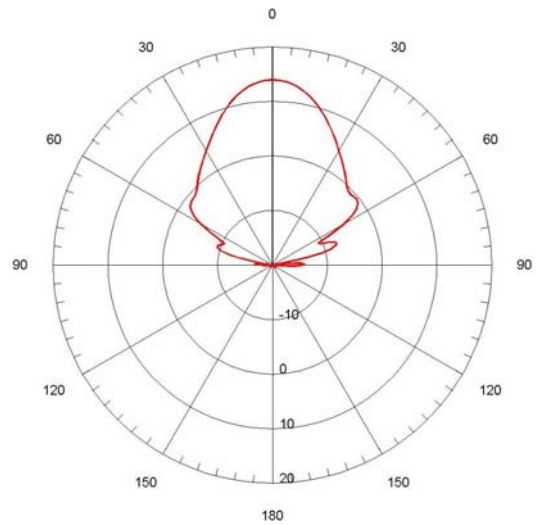
(a)



(b)



(c)



(d)

Figure A.2: E-Plane Gain Patterns for Isolated Vivaldi Antenna with Corrugations at (a) 6GHz, (b) 7 GHz, (c) 8 GHz, (d) 9 GHz, (e) 10 GHz, (f) 11 GHz (**Continued next page**)

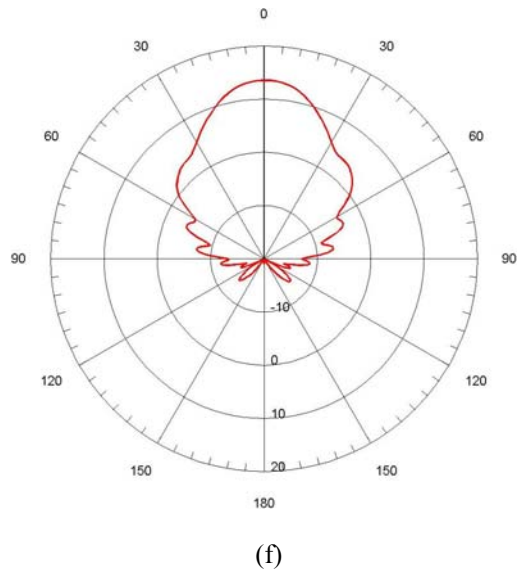
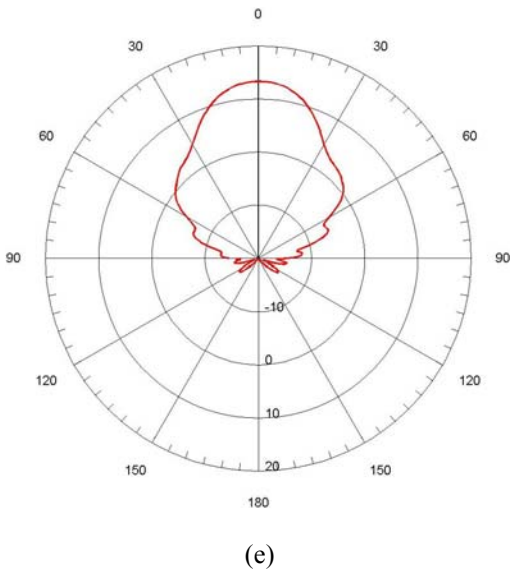


Figure A.2, continued: E-Plane Gain Patterns for Isolated Vivaldi Antenna with Corrugations at (a) 6GHz, (b) 7 GHz, (c) 8 GHz, (d) 9 GHz, (e) 10 GHz, (f) 11 GHz

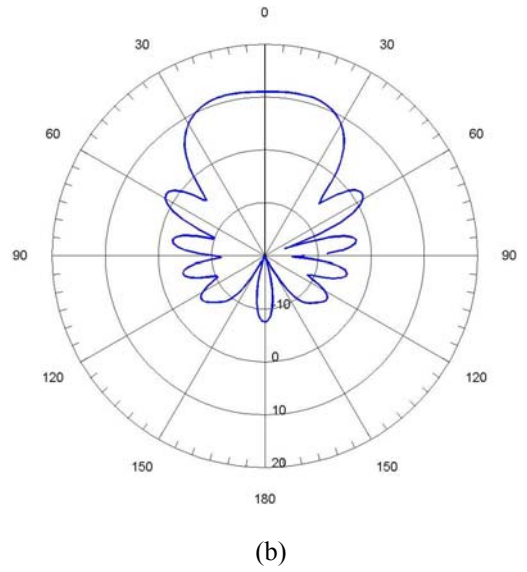
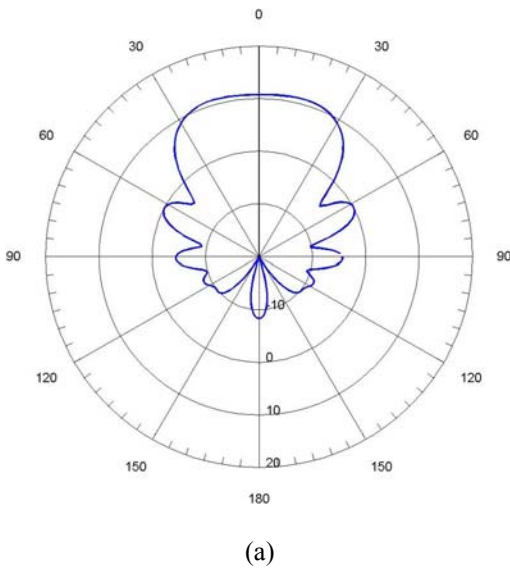
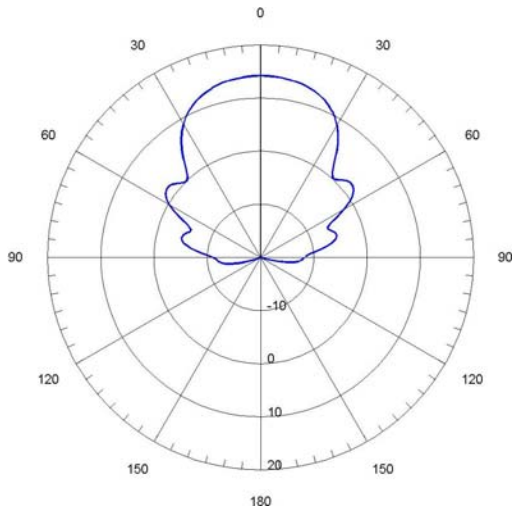
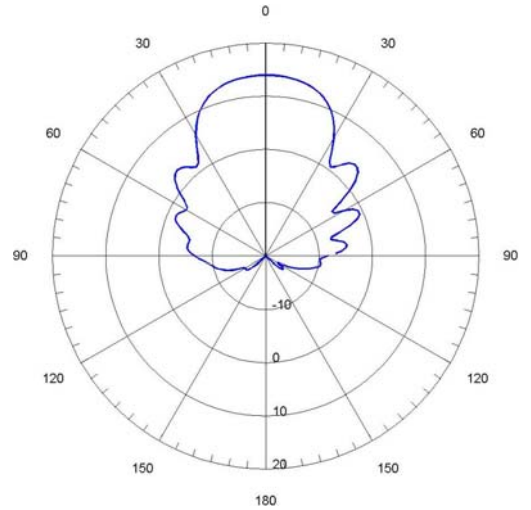


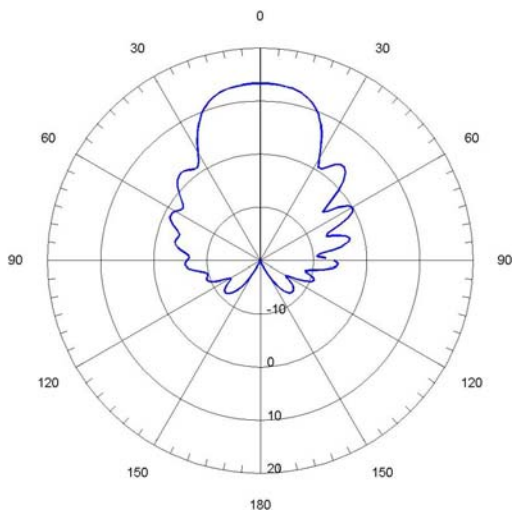
Figure A.3: E-Plane Gain Patterns for Isolated Vivaldi Antenna with Corrugations at (a) 6GHz, (b) 7 GHz, (c) 8 GHz, (d) 9 GHz, (e) 10 GHz, (f) 11 GHz **(Continued next page)**



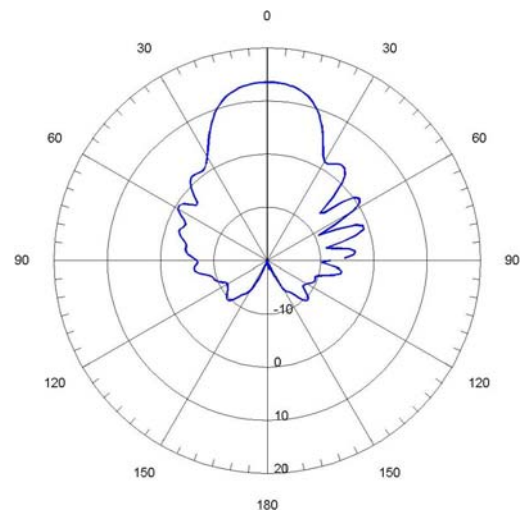
(c)



(d)



(e)



(f)

Figure A.3, continued: E-Plane Gain Patterns for Isolated Vivaldi Antenna with Corrugations at (a) 6GHz, (b) 7 GHz, (c) 8 GHz, (d) 9 GHz, (e) 10 GHz, (f) 11 GHz

The simulated results indicate that introducing corrugations to the sides of the Vivaldi element improves the antenna's overall radiation characteristics. In general, the sidelobe level is reduced when the corrugations are present. Additionally, the antenna's

beamwidth and gain varies less with frequency for the corrugated Vivaldi element. The E-plane and H-plane 3dB-beamwidths, gain, and sidelobe levels of the isolated Vivaldi antenna with and without corrugations are shown in Table A.1 and Table A.2.

Table A.1: E-Plane Radiation Characteristics of Isolated Vivaldi Antenna with and without Corrugations

Frequency	3dB BW (without slots)	3dB BW (with slots)	Gain (without slots)	Gain (with slots)	SLL (without slots)	SLL (with slots)
6 GHz	28.9°	45.7°	12.7 dBi	10.8 dBi	-16.5 dB	-18.3 dB
7 GHz	22.9°	40.5°	13.3 dBi	11.0 dBi	-13.8 dB	-12.3 dB
8 GHz	43.4°	25.9°	11.6 dBi	14.2 dBi	-9.8 dB	-14.8 dB
9 GHz	51.5°	28.1°	10.3 dBi	13.9 dBi	-10.4 dB	-14.4 dB
10 GHz	44.1°	34.4°	11.0 dBi	13.3 dBi	-17.1 dB	-19.1 dB
11 GHz	33.2°	32.8°	12.3 dBi	13.5 dBi	-15.1 dB	-17.3 dB

Table A.2: H-Plane Radiation Characteristics of Isolated Vivaldi Antenna with and without Corrugations

Frequency	3dB BW (without slots)	3dB BW (with slots)	Gain (without slots)	Gain (with slots)	SLL (without slots)	SLL (with slots)
6 GHz	43.4°	67.0°	12.7 dBi	11.0 dBi	-10.8 dB	-11.1 dB
7 GHz	33.1°	62.0°	13.3 dBi	11.3 dBi	-10.8 dB	-9.6 dB
8 GHz	28.6°	49.0°	11.6 dBi	14.2 dBi	-7.8 dB	-12.2 dB
9 GHz	52.8°	44.0°	9.0 dBi	13.9 dBi	-5.2 dB	-10.0 dB
10 GHz	44.9°	40.8°	10.8 dBi	13.3 dBi	-6.8 dB	-9.7 dB
11 GHz	37.0°	28.9°	12.4 dBi	13.7 dBi	-8.0 dB	-11.8 dB

APPENDIX B
DIMENSIONED DRAWINGS

Dimensioned drawings of the antenna elements fabricated in this thesis are presented in the following figures. Note that all lengths are in millimeters, and that all angular values are in degrees.

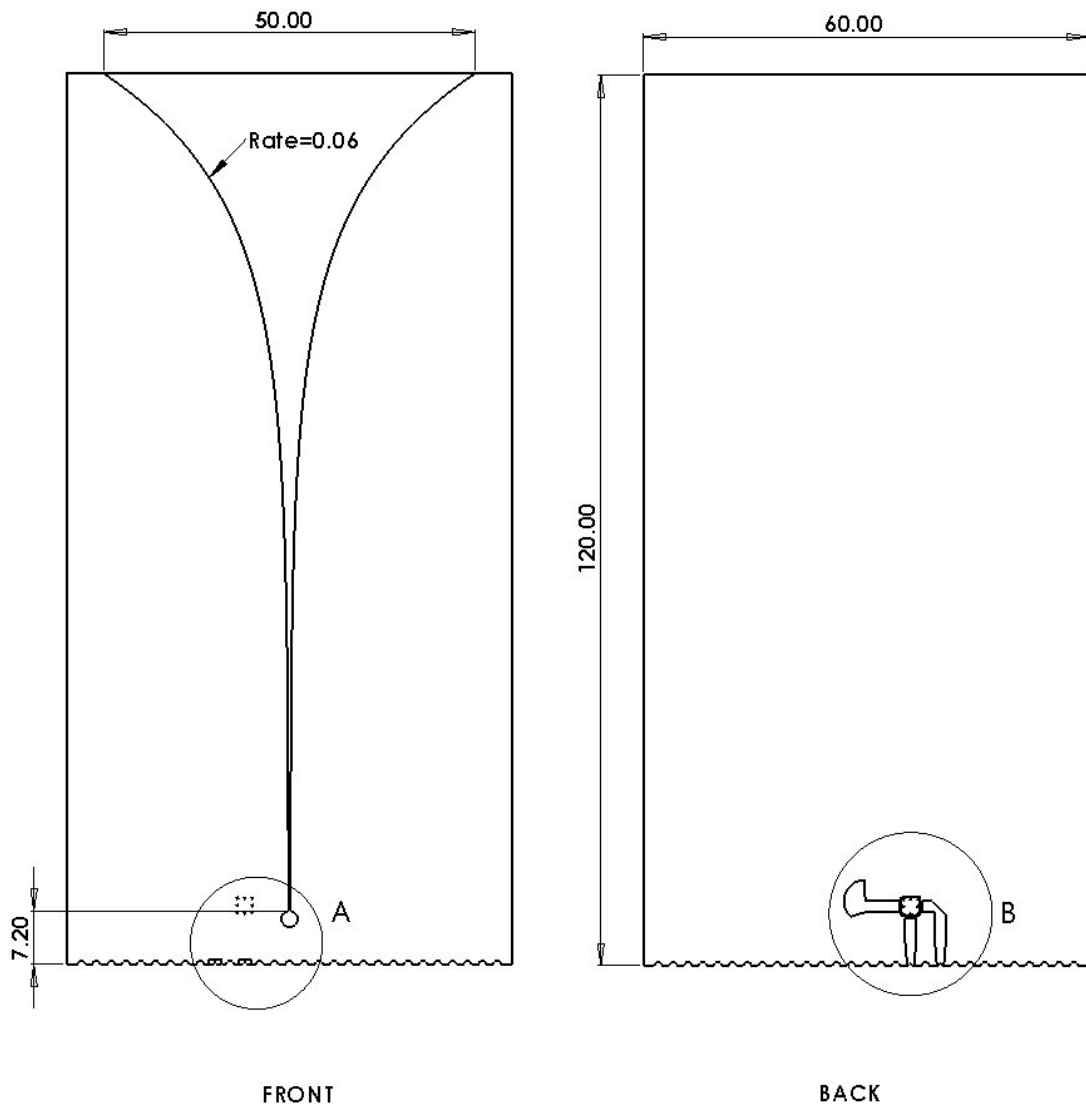
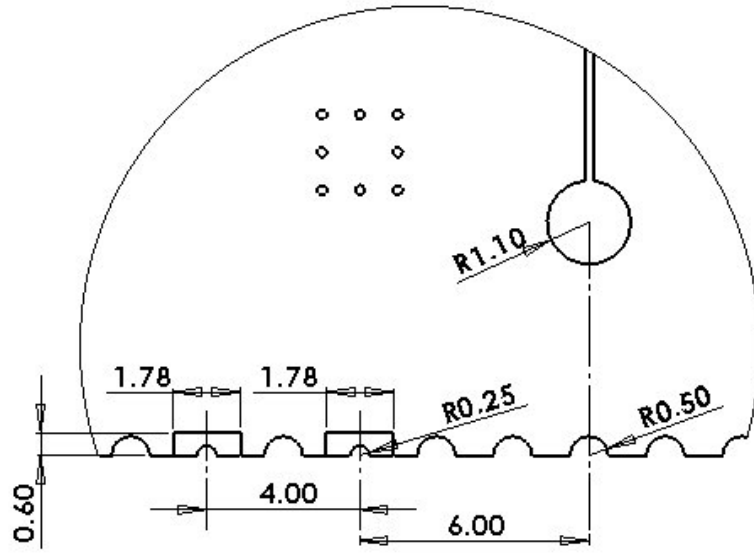
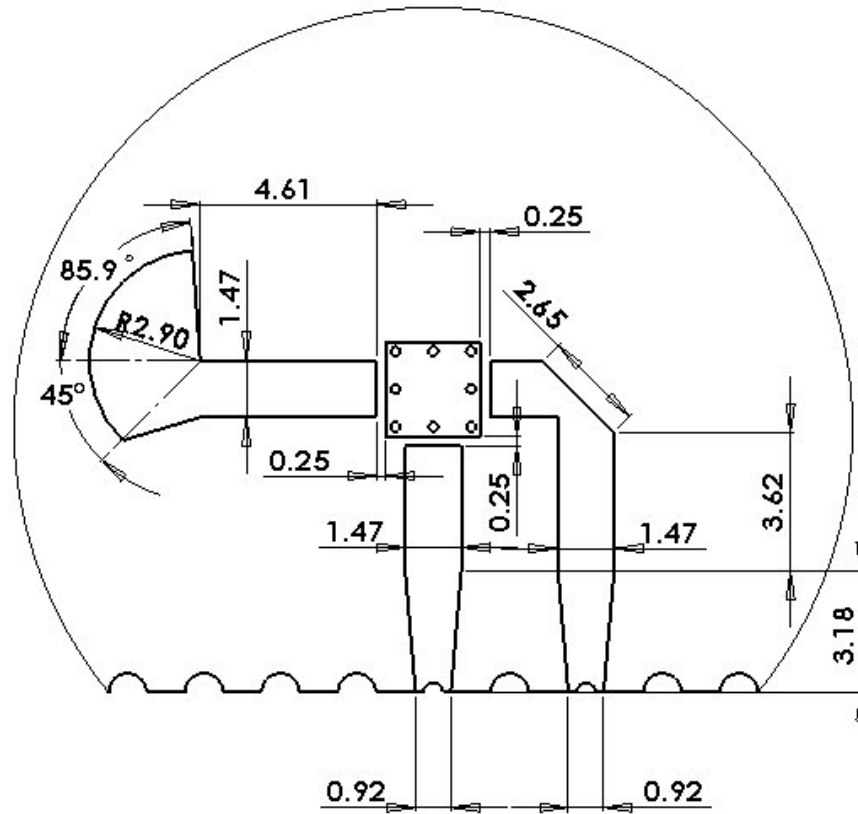


Figure B.1: Isolated Active Vivaldi Element (Continued next page)



DETAIL A



DETAIL B

Figure B.1, continued: Isolated Active Vivaldi Element

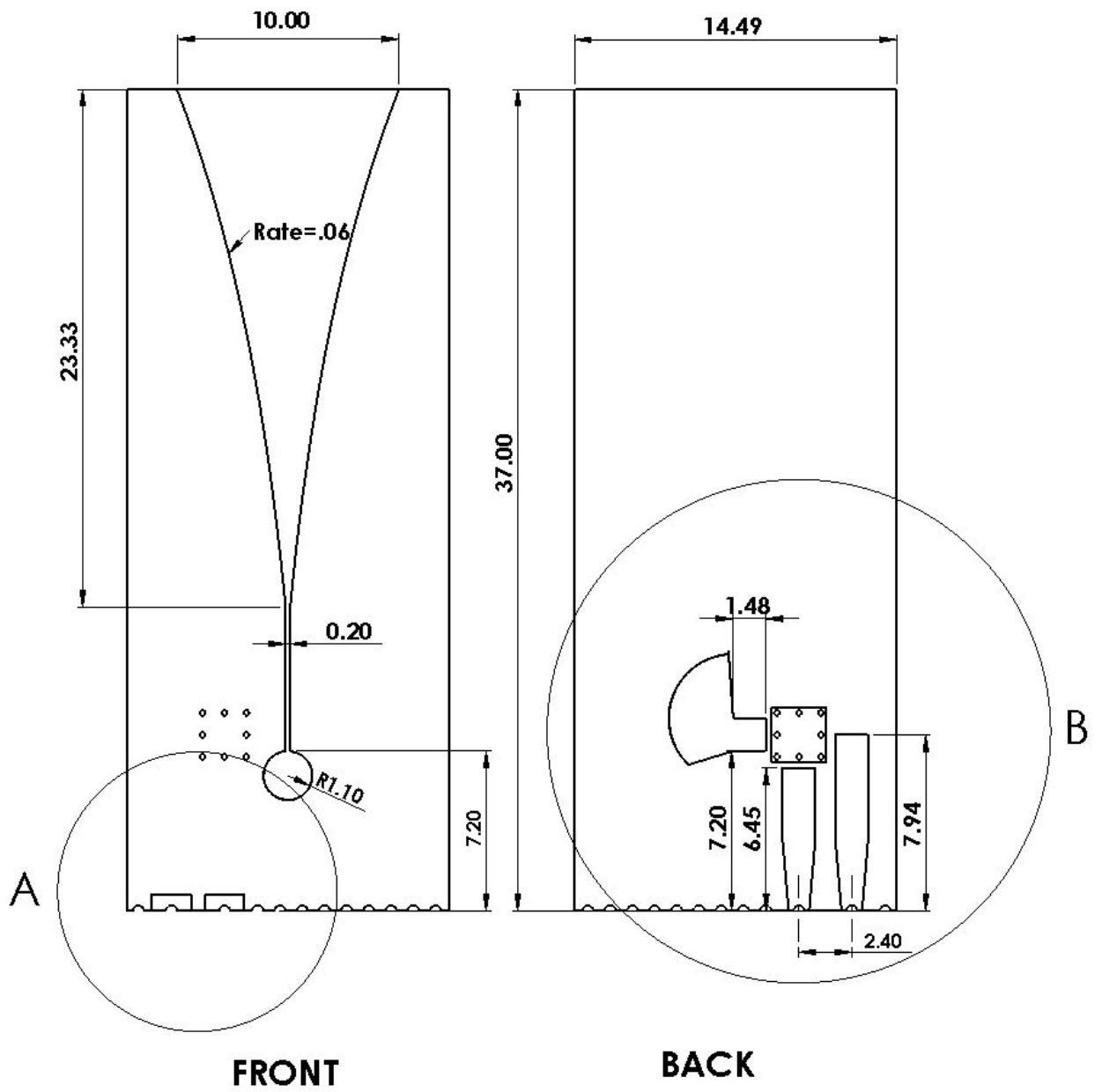
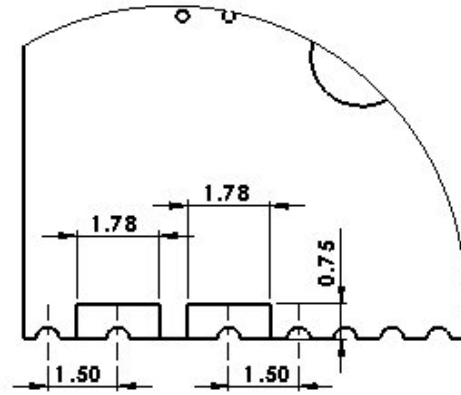
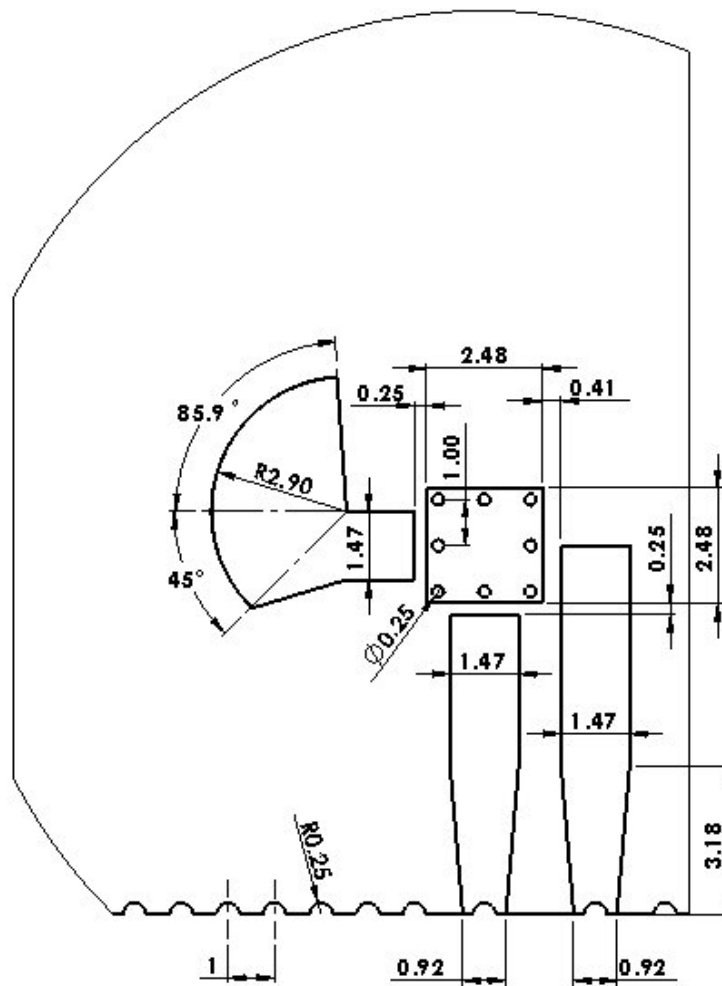


Figure B.2: Active Vivaldi Array Element (Continued next page)



DETAIL A



DETAIL B

Figure B.2, continued: Active Vivaldi Array Element

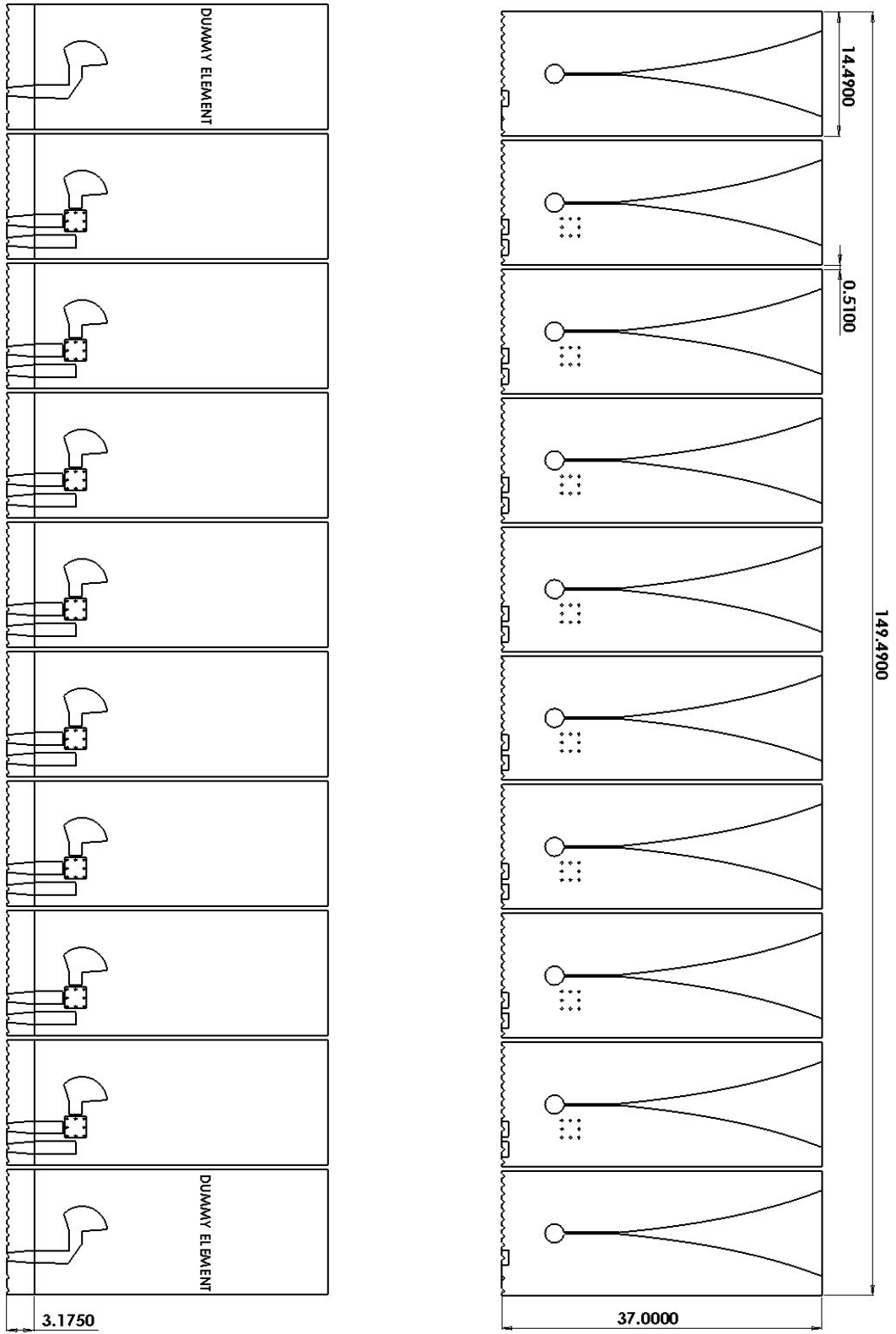


Figure B.3: Full 8x1 Vivaldi Array

APPENDIX C

COMPONENT DATASHEETS



HMC130

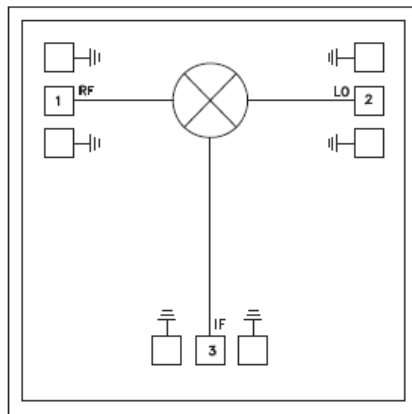
GaAs MMIC DOUBLE-BALANCED MIXER, 6 - 11 GHz

Typical Applications

The HMC130 is ideal for:

- Microwave & VSAT Radios
- Test Equipment
- Military EW, ECM, C³I
- Space Telecom

Functional Diagram



Features

- Conversion Loss: 7 dB
- LO to RF and IF Isolation: >32 dB
- Input IP3: +17 dBm
- No DC Bias Required
- Die Size: 1.45 x 1.3 x 0.1 mm

General Description

The HMC130 chip is a miniature double-balanced mixer which can be used as an upconverter or downconverter in the 6 to 11 GHz band. The chip can be integrated directly into hybrid MMIC's without DC bias or external baluns to provide an extremely compact mixer. It is ideally suited for applications where small size, no DC Bias, and consistent IC performance are required. This mixer can operate over a wide LO drive input of +9 to +15 dBm. It performs equally well as a Bi-Phase modulator or demodulator. See HMC137 data sheet.

Electrical Specifications, $T_A = +25^\circ\text{C}$, LO Drive = +15 dBm

Parameter	Min.	Typ.	Max.	Units
Frequency Range, RF & LO	6.0 - 11.0			GHz
Frequency Range, IF	DC - 2.0			GHz
Conversion Loss		7	9	dB
Noise Figure (SSB)		7	9	dB
LO to RF Isolation	32	40		dB
LO to IF Isolation	35	40		dB
IP3 (Input)	13	17		dBm
IP2 (Input)	45	55		dBm
1 dB Gain Compression (Input)	6	9		dBm

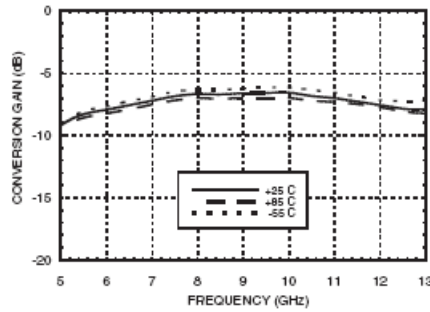
* Unless otherwise noted, all measurements performed as downconverter, IF = 100 MHz

For price, delivery, and to place orders, please contact Hittite Microwave Corporation:
20 Alpha Road, Chelmsford, MA 01824 Phone: 978-250-3343 Fax: 978-250-3373
Order On-line at www.hittite.com

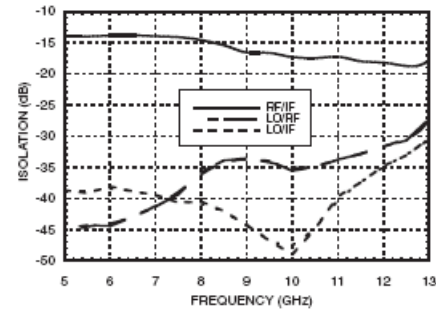
Figure C.1: Datasheet for HMC130 Mixer IC (Continued next page)

GaAs MMIC DOUBLE-BALANCED MIXER, 6 - 11 GHz

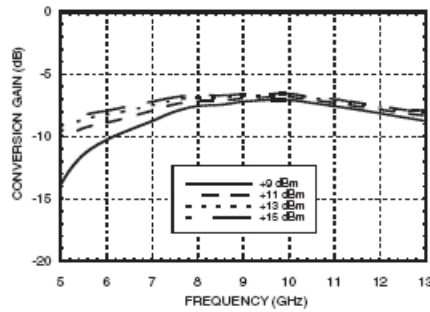
Conversion Gain vs. Temperature
@ LO = +15 dBm



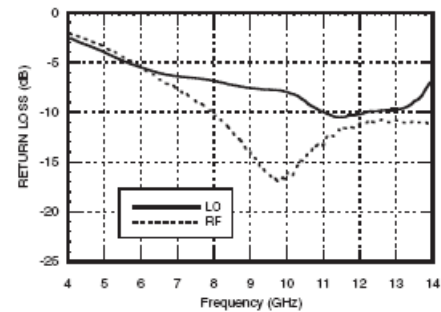
Isolation @ LO = +15 dBm



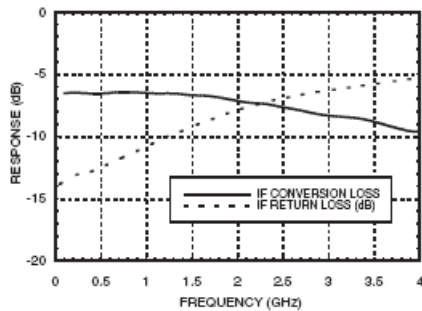
Conversion Gain vs. LO Drive



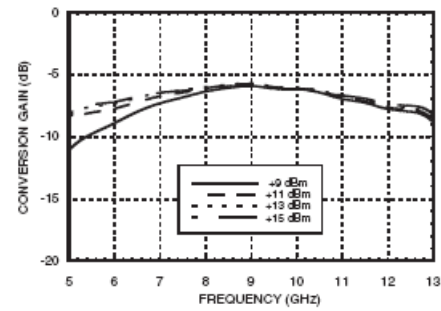
Return Loss @ LO = +15 dBm



IF Bandwidth @ LO = +15 dBm



Upconverter Performance
Conversion Gain vs. LO Drive

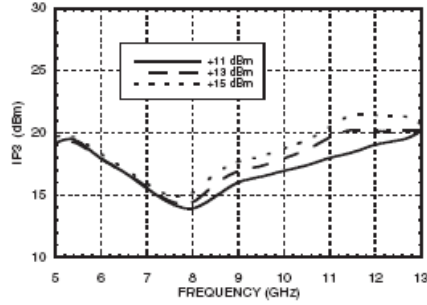


For price, delivery, and to place orders, please contact Hittite Microwave Corporation:
20 Alpha Road, Chelmsford, MA 01824 Phone: 978-250-3343 Fax: 978-250-3373
Order On-line at www.hittite.com

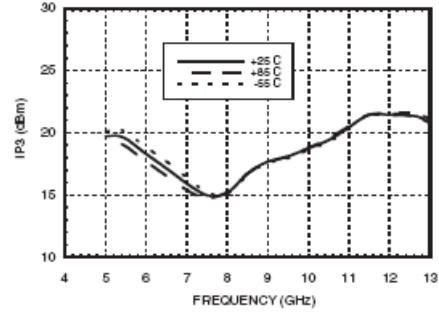
Figure C.1, continued: Datasheet for HMC130 Mixer IC

**GaAs MMIC DOUBLE-BALANCED
MIXER, 6 - 11 GHz**

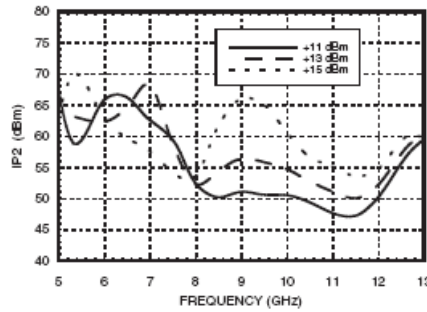
Input IP3 vs. LO Drive



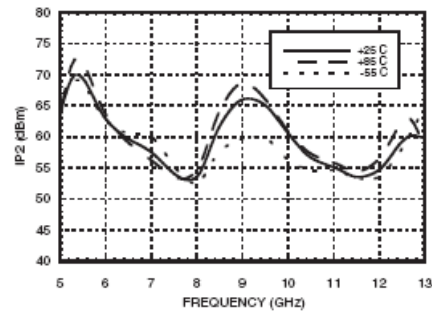
**Input IP3 vs.
Temperature @ LO = +15 dBm**



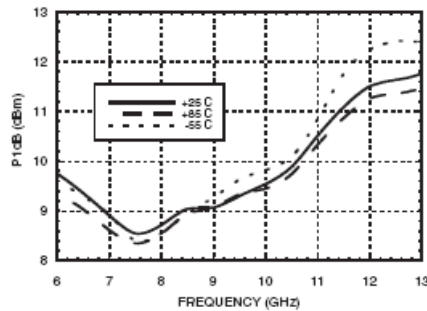
Input IP2 vs. LO Drive



**Input IP2 vs.
Temperature @ LO = +15 dBm**



**Input P1dB vs.
Temperature @ LO = +15 dBm**



Harmonics of LO

LO Freq. (GHz)	nLO Spur @ RF Port			
	1	2	3	4
9.0	45	56	46	79
10.5	42	56	56	62
12.0	36	54	43	60
13.5	35	69	38	57
15.0	35	58	44	?
16.5	32	49	40	?

LO = +13 dBm
All values in dBc below input LO level measured at RF port

For price, delivery, and to place orders, please contact Hittite Microwave Corporation:
20 Alpha Road, Chelmsford, MA 01824 Phone: 978-250-3343 Fax: 978-250-3373
Order On-line at www.hittite.com

Figure C.1, continued: Datasheet for HMC130 Mixer IC

**GaAs MMIC DOUBLE-BALANCED
MIXER, 6 - 11 GHz**

MxN Spurious @ IF Port

mRF	nLO				
	0	1	2	3	4
0	xx	17.16	26.0	9.0	37.33
1	12.83	0	39.83	53.0	33.66
2	69.0	76.5	57.83	76.83	71.0
3	75.33	76.16	78	61.66	78.16
4	66.83	74.83	77.33	78.16	79.66

RF Freq. = 9.1 GHz @ -10 dBm
LO Freq. = 9.0 GHz @ +13 dBm
Measured as downconverter

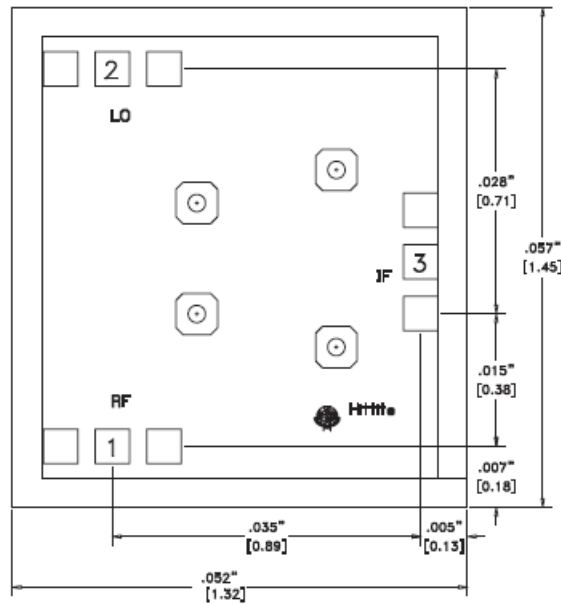
Absolute Maximum Ratings

LO Drive	+27 dBm
Storage Temperature	-65 to +150 °C
Operating Temperature	-55 to +85 °C



**ELECTROSTATIC SENSITIVE DEVICE
OBSERVE HANDLING PRECAUTIONS**

Outline Drawing



Die Packaging Information [1]

Standard	Alternate
WP-3	[2]

[1] Refer to the "Packaging Information" section for die packaging dimensions.

[2] For alternate packaging information contact Hittite Microwave Corporation.

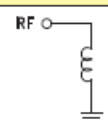
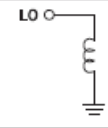
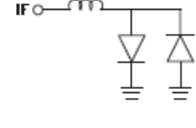
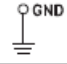
NOTES:

1. ALL DIMENSIONS ARE IN INCHES [MM]
2. BOND PADS ARE .004" SQUARE
3. TYPICAL BOND PAD SPACING CENTER TO CENTER
.1 IS .008" EXCEPT AS SHOWN
4. DIE THICKNESS = .004" [100MM]
5. BACKSIDE METALIZATION: GOLD
6. BACKSIDE METAL IS GROUND
7. BOND PAD METALIZATION: GOLD

For price, delivery, and to place orders, please contact Hittite Microwave Corporation:
20 Alpha Road, Chelmsford, MA 01824 Phone: 978-250-3343 Fax: 978-250-3373
Order On-line at www.hittite.com

Figure C.1, continued: Datasheet for HMC130 Mixer IC

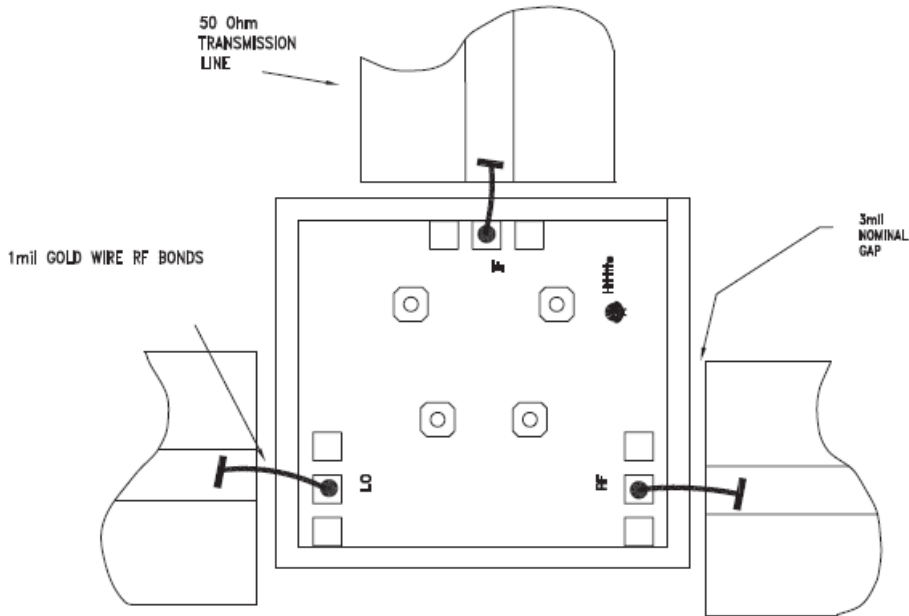
Pad Descriptions

Pad Number	Function	Description	Interface Schematic
1	RF	This pin is DC coupled and matched to 50 Ohms.	
2	LO	This pin is DC coupled and matched to 50 Ohms.	
3	IF	This pin is DC coupled. For applications not requiring operation to DC, this port should be DC blocked externally using a series capacitor whose value has been chosen to pass the necessary IF frequency range. For operation to DC this pin must not source or sink more than 2mA of current or die non-function and possible die failure will result.	
	GND	The backside of the die must connect to RF ground.	

For price, delivery, and to place orders, please contact Hittite Microwave Corporation:
20 Alpha Road, Chelmsford, MA 01824 Phone: 978-250-3343 Fax: 978-250-3373
Order On-line at www.hittite.com

Figure C.1, continued: Datasheet for HMC130 Mixer IC

Assembly Diagram



Handling Precautions

Follow these precautions to avoid permanent damage.

Storage: All bare die are placed in either Waffle or Gel based ESD protective containers, and then sealed in an ESD protective bag for shipment. Once the sealed ESD protective bag has been opened, all die should be stored in a dry nitrogen environment.

Cleanliness: Handle the chips in a clean environment. DO NOT attempt to clean the chip using liquid cleaning systems.

Static Sensitivity: Follow ESD precautions to protect against ESD strikes.

Transients: Suppress instrument and bias supply transients while bias is applied. Use shielded signal and bias cables to minimize inductive pick-up.

General Handling: Handle the chip along the edges with a vacuum collet or with a sharp pair of bent tweezers. The surface of the chip has fragile air bridges and should not be touched with vacuum collet, tweezers, or fingers.

Mounting

The chip is back-metallized and can be die mounted with AuSn eutectic preforms or with electrically conductive epoxy. The mounting surface should be clean and flat.

Eutectic Die Attach: A 80/20 gold tin preform is recommended with a work surface temperature of 255 °C and a tool temperature of 265 °C. When hot 90/10 nitrogen/hydrogen gas is applied, tool tip temperature should be 290 °C. DO NOT expose the chip to a temperature greater than 320 °C for more than 20 seconds. No more than 3 seconds of scrubbing should be required for attachment.

Epoxy Die Attach: Apply a minimum amount of epoxy to the mounting surface so that a thin epoxy fillet is observed around the perimeter of the chip once it is placed into position. Cure epoxy per the manufacturer's schedule.

Wire Bonding

Ball or wedge bond with 0.025 mm (1 mil) diameter pure gold wire. Thermosonic wirebonding with a nominal stage temperature of 150 °C and a ball bonding force of 40 to 50 grams or wedge bonding force of 18 to 22 grams is recommended. Use the minimum level of ultrasonic energy to achieve reliable wirebonds. Wirebonds should be started on the chip and terminated on the package or substrate. All bonds should be as short as possible <0.31 mm (12 mils).

For price, delivery, and to place orders, please contact Hittite Microwave Corporation:
20 Alpha Road, Chelmsford, MA 01824 Phone: 978-250-3343 Fax: 978-250-3373
Order On-line at www.hittite.com

Figure C.1, continued: Datasheet for HMC130 Mixer IC

Narrow Band Phase Shifter

JSPHS-1000+ JSPHS-1000

50Ω 180° Voltage Variable 700 to 1000 MHz



Maximum Ratings

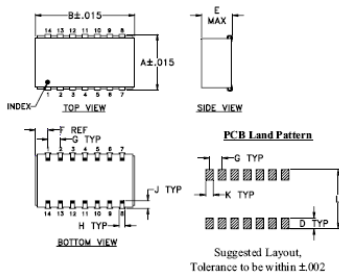
Operating Temperature	-40°C to 85°C
Storage Temperature	-55°C to 100°C
RF Input Power	20 dBm max.
Control Voltage	28V

Pin Connections

IN	1
OUT	7
BIAS	4,6*
GROUND	2,3,5,8,9,10,11,12,13,14

* pins must be connected together externally

Outline Drawing

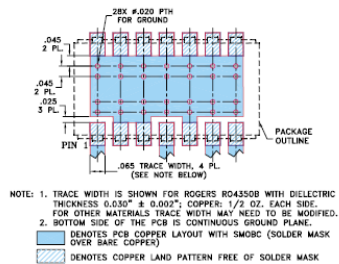


Outline Dimensions (inch)

A	B	C	D	E	F	G
.450	.803	--	.100	.250	.102	.100
11.43	20.40	--	2.54	6.35	2.59	2.54

H	J	K	L	wt
.047	.085	.085	.470	grams
1.19	1.66	1.65	11.94	3.0

Demo Board MCL P/N: TB-122 Suggested PCB Layout (PL-030)



Features

- low insertion loss, 1.4 dB typ.
- good VSWR, 1.3:1 typ.
- solder-plated J-leads for excellent solderability and strain relief
- aqueous washable

Applications

- cellular

CASE STYLE: BK276
PRICE: \$32.95 ea. QTY (1-9)

+ RoHS compliant in accordance with EU Directive (2002/95/EC)

The +Suffix identifies RoHS Compliance. See our web site for RoHS Compliance methodologies and qualifications.

Phase Shifter Electrical Specifications

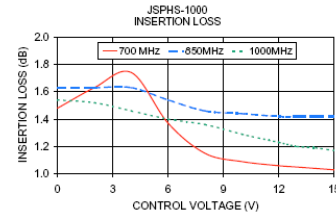
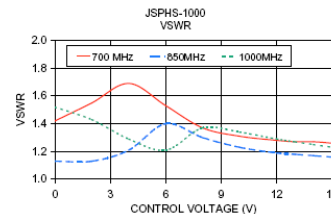
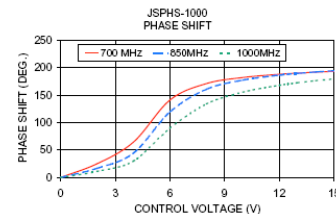
FREQUENCY (MHz)	PHASE RANGE (Degrees)	INSERTION LOSS (dB)		CONTROL VOLTAGE (V)	CONTROL BANDWIDTH (kHz)	VSWR (:1)	
		Typ.	Max.			Typ.	Max.
700-850	180	1.2	2.3	0-15	DC-50	1.2	2.6
850-1000	160	1.2	2.0	0-15	DC-50	1.2	2.0

Maximum operating power, 0 dBm

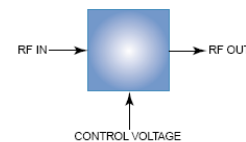
Typical Performance Data

Control Voltage (V)	Phase Shift* (Degrees)			VSWR (:1)			Insertion Loss (dB)		
	700 MHz	850 MHz	1000 MHz	700 MHz	850 MHz	1000 MHz	700 MHz	850 MHz	1000 MHz
0.00	0.00	0.00	0.00	1.42	1.13	1.52	1.48	1.63	1.54
2.00	25.08	16.78	11.21	1.55	1.13	1.43	1.63	1.63	1.52
4.00	64.96	44.54	30.16	1.69	1.21	1.29	1.74	1.63	1.46
6.00	141.20	119.49	89.61	1.53	1.40	1.21	1.37	1.54	1.40
8.00	171.07	160.75	134.12	1.37	1.30	1.17	1.15	1.46	1.36
10.00	182.16	177.41	155.54	1.31	1.23	1.34	1.09	1.44	1.29
12.00	188.09	186.53	168.05	1.28	1.19	1.29	1.06	1.42	1.23
13.00	190.16	189.72	172.58	1.27	1.18	1.27	1.05	1.42	1.20
14.00	191.91	192.37	176.43	1.27	1.17	1.25	1.04	1.42	1.19
15.00	193.41	194.57	179.67	1.26	1.16	1.23	1.03	1.42	1.17

* Normalized at control voltage = 0V



electrical schematic



Mini-Circuits®
ISO 9001 ISO 14001 CERTIFIED

ALL NEW
minicircuits.com

P.O. Box 350166, Brooklyn, New York 11235-0003 (718) 934-4500 Fax (718) 332-4661 For detailed performance specs & shopping online see Mini-Circuits web site
The Design Engineers Search Engine Provides ACTUAL Data Instantly From MINI-CIRCUITS At: www.minicircuits.com



RF/IF MICROWAVE COMPONENTS

REV. C
M102713
JSPHS-1000
ED-8002/1
HYTD:CF/AM
070405

Figure C.2: Datasheet for JSPHS-1000 Phase Shifter

BIBLIOGRAPHY

- [1] K.C. Gupta and P.S. Hill (eds.), *Analysis and Design of Integrated Circuit Antenna Modules*, Wiley-Interscience, 2000.
- [2] K. Chang, R.A. York, P.S. Hall, T. Itoh, "Active integrated antennas," *IEEE Trans. Microwave Theory Tech.*, vol. MTT-50, pp. 937-944, March 2002.
- [3] J. A. Navarro and K. Chang, *Integrated Active Antennas and Spatial Power Combining*, Wiley-Interscience, 1996.
- [4] S. Kasturi, "Design parameters in single polarized, infinite arrays of Vivaldi antennas," M.S. Thesis, Electrical and Computer Eng., Massachusetts, Amherst, MA, Sept 2004.
- [5] H. Holter, T.-H. Chio, and D. H Schaubert, "Experimental results of 144-element dual-polarized endfire tapered slot phased arrays," *IEEE Trans. Antennas Propagation*, vol. 48, pp. 1707-1718, Nov. 2000.
- [6] R. Q. Lee, and R. N. Simons, "Orthogonal feeding techniques for tapered slot antennas," *IEEE Antennas Propagation Symp.*, pp. 1172- 1175, June 1998.
- [7] O. Salmela, T. Nieminen, et. al, "Reliability analysis of lead-free solder castellations," *IEEE Trans. Components and Packaging Technology*, vol. PP, pp. 1-1, 2007.
- [8] U. Guttich, " Planar integrated 20 GHz receiver in slotline and coplanar waveguide technique," *Microwave and Optical Technology Letters*, vol. 2 pp. 404-406, Nov. 1989.
- [9] W. K. Leverich, X. D. Wu, and K. Chang, "New FET active notch antenna," *Electronic Letters*, vol. 28, pp. 2239-2240, Nov 1992.
- [10] M. Sims, D. E. Lawrence, and R. Halladay, "A fully-integrated Vivaldi phased array for seeker applications," *IEEE Antennas Propagation Symp.* vol. 2B, pp. 445-448, July 2005.
- [11] H.F. Lee and W. Chen, *Advances in Microstrip and Printed Antennas*, Wiley-Interscience, 1997.
- [12] L.R. Lewis, M. Fasset, and J. Hunt, "A broadband stripline array element," *IEEE Antennas & Propagation Symp.*, pp. 335-337, June 1974.

- [13] P. J. Gibson, "The Vivaldi aerial," *Dig. 9th European Microwave Conf.*, Brighton, UK, pp 120-124, 1979.
- [14] S. Sugawara, Y. Maita, K. Adachi, and K. Mizuno, "Characteristics of a mm-wave tapered slot antenna with corrugated edges," *IEEE MTT-S IMS Dig.*, vol. 2, pp. 533-536, June 1998.
- [15] J. Shin and D. H. Schaubert, "A parameter study of stripline-fed Vivaldi Notch Antenna Arrays," *IEEE Trans. Antennas Propagation.*, vol. 47, pp. 879-886, May 1999.
- [16] R. .C. Hansen, *Phased Array Antennas*, Wiley-Interscience, 1998
- [17] A. O. Boryszenko, D. H. Schaubert, and C. Craeye, "A wave-based model for mutual coupling and truncation in finite tapered-slot phased arrays," *IEEE Antennas Propagation Symp.*, vol. 4, pp. 11-14, June 2003.
- [18] R. J. Mailloux *Phased Array Antenna Handbook* 2nd Ed. Artech House, 2005.
- [19] D. H. Schaubert, "A gap-induced element resonance in single-polarized arrays of notch antennas," *IEEE Antennas Propagation Symp.*, vol. 2, pp. 1264-1267, June 1994.
- [20] S. Kasturi, "Wideband characteristics of Vivaldi antenna arrays," PhD Dissertation, Electrical and Computer Eng., Univ of Massachusetts, Amherst, MA, Feb 2008.
- [21] D. Slater, *Near-Field Antenna Measurements*, Artech House, 1991.